

3D-printing Form and Function

by

Subramanian Sundaram

B.E. Electrical & Electronics Engineering,
B.E. Mechanical Engineering,
Birla Institute of Technology and Science, Pilani, India (2011)
S.M., Massachusetts Institute of Technology (2014)

Submitted to the Department of Electrical Engineering and Computer
Science

in partial fulfillment of the requirements for the degree of

Doctor of Philosophy in Electrical Engineering and Computer Science

at the

MASSACHUSETTS INSTITUTE OF TECHNOLOGY

September 2018

© Massachusetts Institute of Technology 2018. All rights reserved.

Author
Department of Electrical Engineering and Computer Science
June 8, 2018

Certified by
Wojciech Matusik
Associate Professor of Electrical Engineering and Computer Science
Thesis Supervisor

Accepted by
Leslie Kolodziejski
Chair, Department Committee on Graduate Theses

3D-printing Form and Function

by

Subramanian Sundaram

Submitted to the Department of Electrical Engineering and Computer Science
on June 8, 2018, in partial fulfillment of the
requirements for the degree of
Doctor of Philosophy in Electrical Engineering and Computer Science

Abstract

Integrating diverse functions inside man-made parts with specific shapes, in a highly scalable manner, is the broad challenge in manufacturing. Functional integration is typically achieved by assembling specialized parts, each independently made using carefully designed production techniques - for example, in assembly lines in the automotive industry. This approach of external assembly of specialized parts is tedious at certain length scales (e.g. mesoscale manufacturing), imposes restrictions on achievable geometries, and limits functional integration.

In contrast, nature excels at packing disparate materials and functions into unconstrained geometries across different length scales (e.g. distributed sensors in cuttlefish, or sensorimotor pathways and resonant muscles in insects). These far exceed our current fabrication capabilities, and replicating all the functions of natural systems has remained a distant dream. 3D-printing has resolved many challenges in fabricating complex geometries, but despite its promise, assembling diverse materials (including solids, liquids and thin-films) and functions inside a single, printed composite is a current challenge.

This thesis presents a set of materials, processes and design strategies - a full experimental toolkit - to address the question: *how can we distribute diverse materials and functions in free-form geometries?* First, a fully-3D-printed autonomous composite that can sense an external stimulus, process it, and respond by varying its optical transparency is described. The composite consists of seamlessly integrated solids (UV-cured polymers), thin-films (conducting and semiconducting, solvent-evaporated films), and encapsulated liquids. Techniques to engineer material interfaces are also presented in this section.

A stimulus-free strategy to 3D-print self-folding composites at room temperature is presented in the second part of this thesis. Specifically, the focus is on printing flat electrical composites that fold into pre-programmed shapes after printing using residual stress defined in specific regions. This provides advantages in the fabrication speed, and also expands the range of achievable geometries when using solvent-based inks. The third portion of this thesis focuses on 3D-printing soft actuators. After highlighting a few example applications of printed actuator arrays, this is used as a

case study for topology optimization based design strategies. It is shown that the inclusion of a topology optimizer in the 3D-printing pipeline enables the automated design and fabrication of high-dimensional designs. The final section of this work focuses on creating tactile sensor arrays, with an emphasis on the acquisition of tactile datasets that can be used to understand the human grasp. The concluding section summarizes the role of the fabrication strategies presented here in creating composites of increasing levels of autonomy and self-sufficiency.

Thesis Supervisor: Wojciech Matusik

Title: Associate Professor of Electrical Engineering and Computer Science

Acknowledgments

Very little of my graduate school experience was predictable. My time at MIT was full of surprises and challenges, and more importantly, filled with enjoyable learning experiences. I am thankful to all the fantastic people I crossed paths with, over the past nearly seven years.

Through all these years, Professor Marc Baldo's guidance was one of the few constants. I met him during my first days at MIT, and I am lucky to have had the chance to interact with him all along. Even when we weren't directly collaborating, Marc was an amazing role model who inspired me with his focus on the scientific process. Marc's impact on this thesis and my career are significant, and I'm incredibly fortunate for this. I am thankful to my advisor, Professor Wojciech Matusik for his support through the last four years. He gave me the resources and the freedom to work on projects of my choice with no restrictions. He also encouraged me to develop my own ideas, take them to completion, and become independent. I find his persistence and passionate pursuit of his own projects quite inspiring. I thank him for his enthusiasm in supporting my career pursuits. I am deeply thankful to Professor Vladimir Bulovic for being part of my thesis committee and for offering his perspective on my projects. His comments on both the low-level details and the big picture guided my presentation of ideas in this thesis.

I am extremely thankful to Professor Ryan Hayward at the University of Massachusetts, Amherst - he was such a pleasant collaborator. He helped me understand many ideas in polymer science, and I specifically thank him for his help in the "self-folding composites" project. He kindly hosted me at his lab, and was generous with sharing his ideas on many topics.

My interest in tactile sensors and the human grasp grew out of early discussions with Professor Antonio Torralba, Professor Russ Tedrake and Professor Ted Adelson. I am thankful to them for their wisdom and for our regular meetings which were thoroughly enjoyable. It was also a constant reminder of how amazing CSAIL is. Thanks to Professor Dina Katabi for collaborating with us on printed antennas and

also for many pleasant conversations. Professor Ron Weiss taught some of my favorite courses on synthetic biology and was an excellent teacher.

I am fortunate to have worked with Professor Herbert Shea at the École Polytechnique Fédérale de Lausanne as an undergraduate - I continue to rely on his advice and friendship. Thanks to Professor Klaus Kern at the Max Planck Institute for Solid State Research and Professor Kannan Balasubramanian (now at Humboldt University, Berlin) for helping me get an early start on research at a rigorous environment. My interest in research originated in the offices of Professor N. N. Sharma and the late Professor R. Mehrotra at BITS, Pilani. My undergraduate mentors played an important role in my decision to join a graduate program - it was in these labs where I first experienced the joys of research.

I am thankful to David Kim, Louise van den Heuvel and Melina Skouras for being excellent collaborators and contributing ideas to the magnetic actuators project. The work on automated design and fabrication used many of Melina's simulation and optimization tools. Omid Abari and I had great fun working on printed antennas. Ziwen Jiang and Julia Rubin were ideal UROPs - it was exciting to mentor them and be around their boundless enthusiasm. I would like to thank Pitchaya Sittthiamorn (Yam) who taught me much about our 3D-printer during my first days in the lab. Thanks to all my labmates at the Computational Fabrication Group for their friendship and being great colleagues.

I also want to thank Professor Jeff Lang and Professor Tomas Palacios for helpful discussions during the course of my projects. Daniel Piedra was generous enough to let me use his measurement setup to characterize my printed transistors, sometimes even during the weekends. My experiments and characterization measurements also benefited from the advice of countless research staff at MIT. I want to thank Geetha Berera, David Bono and Timothy McClure in particular for their help with material characterization. Thanks to Paul Tierney, Dennis Ward, Donal Jamieson, and the MTL staff for their help with my fabrication processes during my first 3 years at MIT, a large part of which I spent at the MTL cleanroom.

I am extremely grateful to my dear friends for supporting me and inspiring me

throughout this journey. Finally, this thesis would not have been possible without my family's encouragement and belief in me. This thesis is dedicated to my mother and grandmother. They enabled much of what I have today through their continuous sacrifice, foresight and resilience. I am forever thankful to them.

Contents

1	Introduction	19
1.1	Autonomous Composites	21
1.2	3D-printing and additive manufacturing	23
1.3	Thesis overview	25
I	3D-Printed Multimaterial Composites	27
2	Drop-on-demand 3D-printing	29
2.1	Inkjet-based 3D-printing	30
2.2	Ink requirements and processing	31
2.3	Material interface engineering	35
2.3.1	Effect of surface energy	35
2.3.2	Voxel filling	37
2.3.3	Surface texture	38
2.3.4	Geometric control of interfaces	40
3	Autonomous sensory composites	41
3.1	Fabrication of sensory composites	41
3.2	Printed strain sensor	43
3.3	Organic electrochemical transistors (OECTs) and amplifiers	49
3.4	Electrochromic pixel	52
3.5	Integrating the parts	53
3.6	Experimental methods	55

II	Generating Shape by Programmed Self-Folding	58
4	Polymer swelling induced residual stress	59
4.1	Printing materials with residual stress	60
4.2	Role of crosslink density	62
5	Self-folding electronic composites	69
5.1	Shape transformation in electronics	69
5.2	4D-printing	70
5.3	Self-folding bilayer	72
5.4	Modeling the self-folding system	75
5.5	Self-folding composites	83
5.6	Experimental methods	89
III	3D-Printed Actuators - <i>a case for automated design</i>	91
6	Multimaterial magnetic actuators	93
6.1	3D-printed mesoscale magnetic actuators	93
6.2	Magnetic actuator characteristics	100
6.3	Experimental methods	105
7	Topology-optimization for automated design and fabrication of actuators	111
7.1	Multi-objective topology optimization	113
7.2	Printed topology-optimized actuators	118
7.3	Experimental methods	121
IV	Tactile Skins for Understanding Human Grasp	124
8	Tactile sensor arrays & gloves	125
8.1	Fabrication of a regular array	126
8.2	Sensor characterization	128

8.3	Sensor array and readout circuit	130
8.4	Extensions to the sensor array	133
8.5	Towards tactile gloves	136
8.6	Future work	138
9	Conclusions	141
9.1	Future work	142
A	Ink formulations	145

List of Figures

1-1	Autonomous Composites	22
2-1	Schematic of functional parts of our printer	31
2-2	Resolution and droplet size	32
2-3	Three ways to convert ink to final use materials	34
2-4	Surface energy measurements from droplet shapes	36
2-5	Voxel filling strategies	39
2-6	Surface texture of the electrical contacts	40
3-1	Golden Tortoise Beetle (<i>Charidotella secpunctata</i>)	42
3-2	Schematic of the autonomous sensory composite	44
3-3	Stress-strain measurements of the UV curable materials - RIG and ELA	45
3-4	Strain sensor design and performance	46
3-5	Strain sensor performance under high strain	47
3-6	Strain sensor performance under repeated cycling	48
3-7	Printed organic electrochemical transistor (OECT) - design and performance	50
3-8	Transistor performance characteristics - transfer, I-V curves	51
3-9	Single-stage common source amplifier properties	52
3-10	Electrochromic pixel design and performance	53
3-11	Device with fluidic coupling enables controlling transparency and shape	54
3-12	Integrated autonomous sensory composite tests	56
4-1	Swelling of UV cured polymer samples in different components	62

4-2	FTIR spectra of STR samples with varying levels of crosslinks	63
4-3	Double bond conversion and cure depth of STR samples	64
4-4	Linear strain due to swelling and mechanical properties (STR)	65
4-5	Mechanical strain tests of printed STR slabs	66
4-6	Differential scanning calorimetry (DSC) and dynamic mechanical analysis (DMA) data - RIG and STR	67
5-1	Overview of self-folding composites	73
5-2	Characteristics of the bilayer system used for creating folds.	74
5-3	Bilayer characteristics at elevated temperatures and design guidelines	76
5-4	Modeling the folding in the bilayer geometry - extracting prescribed strain	80
5-5	Folding angle measurements and comparison with simulation	81
5-6	Effect of heating and high UV dose on the folding process	82
5-7	Electronic self-folding composite design	84
5-8	Self-folding electronic composites	86
5-9	Measured folding angle with mechanical stops	87
5-10	Unfolding forces	88
6-1	Magnetic actuators - material property library	95
6-2	Magnetic actuators - supplementary material characteristics	95
6-3	Actuator general design	96
6-4	Printed actuator arrays	97
6-5	Magnetically actuated displays	98
6-6	Magnetic actuation at fluid interfaces	99
6-7	Experimental verification of tilting angles	102
6-8	Modeling of the external magnetic field	103
6-9	Force generated by our actuators	103
6-10	Switching transients and bandwidth measurements - small amplitude regime	104
6-11	Transient response - large amplitude actuation	106

6-12	Long term cycling test of the small actuator	107
7-1	Topology optimization for function driven actuator fabrication	113
7-2	Panel appearance computation	115
7-3	Dot gain images	116
7-4	Panel optimization for both optical and mechanical properties	119
7-5	Force and deflection measurements of the topology optimized actuator	120
7-6	Long term cycling test of $l_p = 19$ mm actuators	121
7-7	Topology optimized actuator array - grass and stones	122
8-1	Schematic of the tactile sensor array	127
8-2	Strain sensor characteristics and long term cycling	129
8-3	Sensor characteristics of 3 devices	130
8-4	Readout scheme for the tactile sensor array	131
8-5	Fabricated 32×32 sensor arrays	132
8-6	Captured 10 object dataset of visual and tactile images	134
8-7	Auxetic patterns for sensor arrays	135
8-8	Thermal characteristics of the pressure sensitive film	136
8-9	Tactile glove	137
8-10	Future work	139

List of Tables

2.1	Surface tension of probe liquids	37
2.2	Contact angles of probe fluids on RIG and ELA	37
2.3	Surface energy of cured RIG and ELA	37
A.1	Ink formulations for devices in Part I	147
A.2	Ink formulations for devices in Part II	148
A.3	Ink formulations for devices in Part III	149

Chapter 1

Introduction

Modern day manufacturing relies on the use of specialized manufacturing methods to produce parts ranging from automobiles and airplanes to robots and medical implants. These end products vary significantly in size, material composition and complexity, but importantly, also have great variance in the number and kind of custom-made machines and tooling required to produce them. Manufacturing industries are optimized to produce identical parts in large quantities using processes that are fast and efficient in their use of raw materials. Manufacturing of these modular parts has been a tremendous success story and is one of the foundations of industrialized economies. At the same time, this has also furthered an assembly-centric approach to manufacturing. Specifically, when multiple functional parts are required to build a larger system, they are typically produced individually and then assembled in a traditional assembly line.

It is possible to imagine new paradigms in manufacturing that can overturn this model, which is of extreme interest as any improvements in this broad framework would have large impacts on economically vital industries. Several broad alternatives and ideas are being explored today. Some important questions that are being asked are:

1. We can produce identical parts in a high-throughput manner. Can we produce customized parts - each tailored to a particular person - as efficiently?

2. Manufacturing equipment is often prohibitively expensive. Will home users be able to produce small quantities of parts using low cost machines?
3. Can we manufacture parts with complex shapes?
4. Can one low-cost machine produce more than one type of part?
5. How can a non-expert user design these parts quickly?
6. If these simpler hobbyist machines become pervasive, will we rely less on shipping and more on digital transfer of design files?

Three-dimensional printing (3D-printing, sometimes more broadly referred to as additive manufacturing [AM]), is emerging as a promising approach to explore these fabrication challenges. As these questions are being answered, the face of manufacturing is itself evolving. At a fundamental level modern products are increasingly optimized, and pack functions more densely together. These functions span multiple domains - electrical, mechanical, optical and so forth. The bigger challenge comes from our current reliance on modular parts as we enter the era of mass customization. When customizing small objects like hearing aids, the amount of “real estate” is small and we can no longer use modular parts - modularity costs space. Products of the future will be designed and fabricated in a completely integrated way resembling natural organisms.

This thesis is aimed towards the broad challenge of achieving the levels of functional integration seen in nature. Consider the sensorimotor pathways seen in natural organisms. These pathways are made up of individual elements that have a multitude of functions, and are arranged in close proximity in three dimensions. These functions are further defined at multiple length scales and hierarchies, and are created by assembling materials from a diverse palette. This density of functional and material integration enables much of the autonomy, efficiency and reliability of natural systems. Replicating this level of functional integration has been extremely challenging, even using additive manufacturing techniques. We largely rely on external assembly

for functional integration, and can't densely pack diverse materials in freeform geometries. Simply put, our fabrication capabilities are limited compared to strategies used by nature. The ability to replicate even a part of natural integration strategies would be useful for applications in fields like robotics. This thesis addresses the question:

“How can we integrate diverse functions in parts with unconstrained geometries?”

More specifically, the focus here is on functional elements that contribute to autonomy, such as sensors, processors and actuators. This is in part motivated by their pervasive presence in intelligent machines and robots. It is desirable to integrate these elements into seamless parts with complex 3D-geometries to form *autonomous composites*. Fabricating these composites requires the fundamental ability to arrange disparate materials - solids, liquids and thin films - freely in three dimensions and engineer their interfaces. More generally, fabricating form and function without external assembly demands precise control of material integration. This thesis describes in detail the materials, design approaches, device designs, fabrication processes and experimental methods to produce minimal versions of these autonomous composites.

1.1 Autonomous Composites

Mixing multiple materials to build composites with improved performance is an old, time tested strategy. For instance, wattle-and-daub is a composite structural material has been used for several millennia to make walls¹. The idea that the *right* materials can be brought together to create arbitrary functions inside *smart composites*² is widely accepted today. These composites can be considered primitive man-made analogues of biological systems. When a wide range of functions are simultaneously integrated in a composite, the boundary between materials and machines is blurred³. Specifically, we can envision such a composite where many sensors that sense external or internal stimuli are distributed freely in the structure. The received stimuli are processed using distributed signal processors and an appropriate collective response is effected by actuators. These composites would be able to communicate among

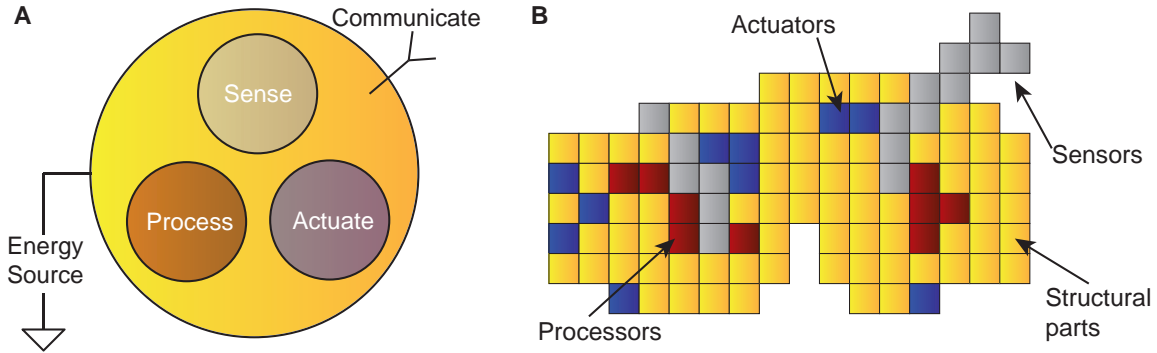


Figure 1-1: **Autonomous composites.** **A.** Autonomous composites integrate elements that enable basic autonomy into a single composite that is structurally stable and self-sufficient. Additionally, they allow individual composites to communicate with each other to perform coordinated tasks. **B.** One can abstractly segment these functions (and materials) into discrete compartments within a seamless composite.

themselves and with the outside world over extended periods of time with access to an energy source. When all these individual functions are brought together to enable autonomy, we define these composites as Autonomous composites, as shown in Fig. 1-1. Amorphous computing⁴ and robotic materials⁵ are analogous ideas that exist in robotics.

Aggregations of diverse functions that exist in nature have often served as inspiration in robotics and other related fields. (i) Cuttlefish are able to quickly sense the surrounding scene and camouflage themselves rapidly and effectively. This is possible due to their ability to locally sense light and respond by controlling the chromatophores on their skin⁶. (ii) The human tactile system has equally intrigued robotics - we cannot yet match the number or density of mechanoreceptors in the human palm⁷ in contemporary robots. This has limited our ability to both understand the primate grasp as well as use a similar system in robots. (iii) Insect flight is enabled by a sophisticated control system that consists of sensors and efficient resonant actuators. For example, the fruit fly uses inputs from both vision and antennae mechanoreceptors to stabilize itself in flight⁸. These examples highlight the long-standing roadblocks that exist in building hardware for robotics, and it is easy to see the role that artificial autonomous composites have in addressing this. Biomimetic and bio-hybrid functions feature prominently in the grand challenges of robotics⁹.

The recent surge in interest in biomimetic functions has happened in parallel with rapid improvements in fabrication technology in diverse fields - this has enabled fascinating new directions of inquiry. There have been many advances in using self-assembly techniques across vastly differing length scales¹⁰ and advances in MEMS and semiconductor fabrication technologies have led to proposals such as the smart dust project¹¹. Emerging advances in genetic engineering and synthetic biology have enabled the paradigm of biological fabrication¹². In addition, over the past three decades, 3D-printing techniques have come into the picture and have grown rapidly. This is the fabrication method explored here due to its advantages in creating free-form geometry and its ability to handle a diverse materials palette.

1.2 3D-printing and additive manufacturing

In 1981, Hideo Kodama described a way to fabricate 3D models using a photo polymer¹³. This, along with Chuck Hull's first patent¹⁴ is considered to be the beginning of 3D-printing as we know it today. It has since become a term for a collection of different techniques that enable the creation of parts made of diverse materials using additive processes. In general, most 3D-printers enable fabrication of complex structures by assembling powders, inks or filaments using a motion controlled stage (or gantry). The printhead is the active material deposition system which can be an inkjet printhead, a filament extruder, or even a controlled light source that dictates curing. A detailed description of all the different 3D-printing methods is beyond the scope of this work, but a short description of a few popular techniques is given below:

1. Stereolithography (SLA): In SLA techniques, a liquid resin is contained in a bath and can be selectively photo cured one volume element (voxel) at a time or one layer at a time. Subsequently, the stage on which the layer is polymerized is advanced to create the next layer on top. SLA is considered the first 3D-printing process.
2. Fused Deposition Modeling (FDM): A filament is extruded through a heated

nozzle which is mounted on a gantry. Typically, the extruder (or printhead) is mounted on a 2-axis gantry and the printer platform provides the 3rd axis of control. FDM is the most widely used consumer 3D-printing process.

3. Powder-based 3D-printing: In powder based additive manufacturing, powdered plastic or metal is bound together by using a binder (which is inkjet on top) or sintered using a laser source. In this process the resultant part is often *green* (i.e., requires further processing) and the material properties are typically enhanced by post-processing. Powder based 3D-printing techniques occupy a large part of the industrial 3D-printing space.
4. Drop-on-demand 3D-printing: This is an extension of the more common 2D inkjet printing process used in desktop inkjet printers. Drop-on-demand 3D-printing involves the use of UV-curable inks that can be deposited using a heated printhead that can be subsequently cured after deposition. These techniques have significant advantages in their multimaterial manufacturing capabilities.
5. Direct ink write (DIW): In a typical DIW process, material is extruded through a nozzle by using a high pressure air inlet. The printer setup is analogous to the FDM process and the printing process is controlled using a vector motion controller. This process is widely used in academic research today due to its simplicity and freedom in material compatibility.

3D-printing rivals traditional processing in its ability to work with complex materials. In parallel, examples of 3D-printed devices demonstrating different functions are emerging now. These developments are often accompanied by variations and improvements in the printing process itself. Recent demonstrations have produced a wide range of materials: polymer-derived ceramics¹⁵, a bone replacement¹⁶, transparent fused silica glass¹⁷ and stainless steels with high strength¹⁸. With the ability to achieve superior material properties, attention is now shifting to the functions that can be created using 3D-printing. So far a range of functional devices such as micro-batteries¹⁹, quantum dot light emitting diodes (LEDs)²⁰, strain sensors²¹, satellite

propulsion system²², hydraulically-driven robots²³ and dielectric elastomer actuators²⁴ have been 3D-printed. These few examples highlight the breadth of devices that can be printed. However, the typical challenge is in fully printing all parts of these devices completely (i.e. not relying on any external processing) and integrating diverse components inside the same part using the same printing process.

1.3 Thesis overview

The objective of this thesis is to enable the integration of diverse functions inside objects of complex shapes - this is in part inspired by the limitless freedom in the integration of functions seen in nature organisms, as mentioned earlier. The main hypothesis here is that this is only possible if we are able to integrate diverse materials in free-form geometries. Further, the ability to control the placement of these materials and engineer their interfaces is an essential requirement. With this in mind, we develop fundamental ideas for integrating solids, liquids and thin-films together. Material interfaces can be controlled by designing the materials themselves or by controlling physical properties such as surface texture and geometry. Part I explores material interfaces in detail in the context of autonomous sensory composites - an integration of sensing, processing and output devices. This is the first demonstration of fully 3D-printed transistors that are integrated together to form amplifiers inside a matrix that consists of rigid and elastic materials. The next part of the thesis, part II, presents a new folding technique based on programmed residual stress. This allows programmed spontaneous folding in a printed object once it is removed from the printer platform, i.e. without any controlled stimulus. In part III, we devise a strategy to design and fabricate magnetically-actuated panel arrays. Notably, the focus is on an automated design and fabrication scheme that utilizes a fabrication-aware optimization process. The first three parts of the thesis are based on a voxel-based 3D-printing approach. The subject of part IV is the fabrication of tactile arrays and gloves. The main goal of this part of the thesis is to demonstrate a rapid and scalable scheme for obtaining tactile data when humans grasp objects. Finally, the last

chapter of the thesis summarizes the results and present potential directions to build upon this thesis.

Part I

3D-Printed Multimaterial Composites

Chapter 2

Drop-on-demand 3D-printing

Inkjet printing, despite its conception over a century ago, reached wide adoption in the second half of the 20th century. It was during this time when microelectromechanical systems (MEMS)-based printhead technologies (piezoelectric or thermal droplet generation systems) were developed, and came into broad use. In traditional inkjet printing, droplets are generated (typically $\sim 50 \mu\text{m}$) and can each be independently controlled and positioned on a substrate. These droplets are then dried by evaporating the solvent, absorbing them onto a substrate, or solidified²⁵. These droplets can be triggered at a frequency up to 1 - 20 kHz per nozzle, and typically each printhead contains up to 100s of nozzles. While it is still widely used in graphics output and marking on paper, it has emerged as a promising manufacturing technology in different fields²⁶ ranging from printed electronics²⁷⁻²⁹, nucleic acid synthesis³⁰, and biological cell printing^{31,32}. The most compelling case for the use of inkjet printing, as far as this thesis is concerned, comes from its multimaterial capability and ability to actuate a large number of nozzles that can be independently triggered at any given time. We now describe our custom built drop-on-demand 3D-printer that contains multiple piezoelectric printheads, and can support multiple diverse materials.

Contents of this chapter are adapted with permission from - S. Sundaram, Z. Jiang, P. Sitthi-Amorn, D. S. Kim, M. A. Baldo, W. Matusik, "3D-printed autonomous sensory composites", *Adv. Mater. Technol.*, 2, 1600257 (2017). <https://doi.org/10.1002/admt.201600257> [Copyright John Wiley and Sons]

2.1 Inkjet-based 3D-printing

Drop-on-demand inkjet 3D-printing is an extension to the traditional 2D inkjet printing process. The transition to fabrication in three dimensions requires new hardware, design strategies and inks - all of which will be addressed in this thesis. The hardware consists of a 3D gantry - where the printhead is mounted on a carriage that can typically move in 2 axes and a printer platform which moves in the third dimension, often the z -axis. Our 3D-printer consists of two commercial printheads (from the Epson Workforce 30 printer), and can print up to a maximum of 10 different materials simultaneously³³. Each printhead has 540 individual nozzles. The inks to be printed are connected to the printhead and maintained at an optimized pressure using an air-input pressure control system. The pressure (positive or negative) is optimized based on the fluidic resistance of the path from the connector to the printhead nozzle. Each of the printheads can be connected to 5 unique inks. In our case, one print is heated to a temperature of 70 °C. So all the inks connected to this printhead have to be stable at this temperature, and also lie in the printable viscosity and surface tension range. The ink requirements are described in more detail later. The heated printed is typically used with UV curable inks in our printer. This is generally because most UV curable inks and resins tend to be higher in viscosity (~ 120 cP) than what the printhead is designed for (2 - 15 cP). Here temperature is used to reduce the ink viscosity to the printable range. The second printhead is maintained at room temperature and is used with all other inks. Apart from the two printheads, the carriage also contains energy sources - a heater and a UV LED array. The typical use of these energy sources is described in the next section.

The 3D-printing process begins with the voxelization of the 3D design to be printed. The voxel dimensions are chosen based on the typical droplet size. Our printheads are optimized for producing droplets that are ~ 30 μm in size. The typical voxel dimensions we use are $35 \mu\text{m} \times 35 \mu\text{m} \times 17 \mu\text{m}$. A typical droplet imaged midair is shown in Fig. 2-2A, and printed lines that are single voxel wide show the lateral resolution of the printing process ($\sim 35 \mu\text{m}$). This is used to divide the full

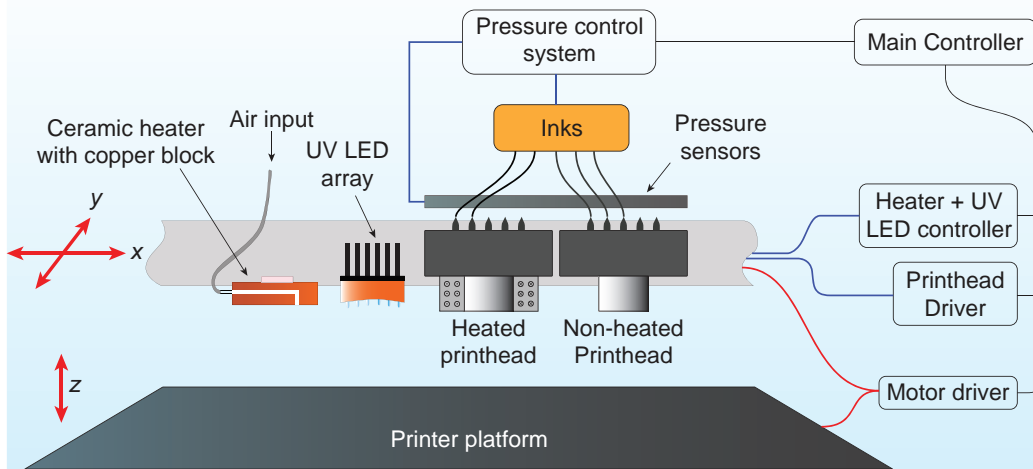


Figure 2-1: **Schematic showing the functional parts of our printer.** The printer consists of a carriage that moves in-plane (x and y -axis) and a platform that moves vertically (z -axis). The carriage consists of two printheads, one heated and one maintained at room temperature. Inks fed to the printhead are deposited on the printer platform. Subsequently, they are either UV-cured using the UV LED array, or heated using a ceramic heater, or left as ink inside a printed well to be encapsulated later. The process parameters and gantry are controlled by a central processor.

3D structure into individual voxels arranged in a lattice. Each voxel can then be assigned a material number that corresponds to a specific material. The end result is the deconstruction of the 3D design file in a stack of bitmaps where each pixel corresponds to the material assignments to corresponding voxel in the slice. Once this voxelized input file is generated, the motion control system and the printhead driver can be used to trigger droplets from individual nozzles at the right positions.

2.2 Ink requirements and processing

Drop-on-demand inkjet printheads impose strict restrictions on the ink rheology. At a basic level the ink cannot contain any particulate matter that can clog the nozzles. In practice, the particulate content has to be less than one-tenth the size of the nozzle to prevent clogging. There are several ink rheology conditions to be met for it to be printable. The Z -number has to lie in the range $1 < Z < 10$; Z is a non-dimensional parameter defined as the inverse of the Ohnesorge number $(Oh)^{25}$. The Ohnesorge number relates the viscous forces to the inertial forces and surface tension of the ink

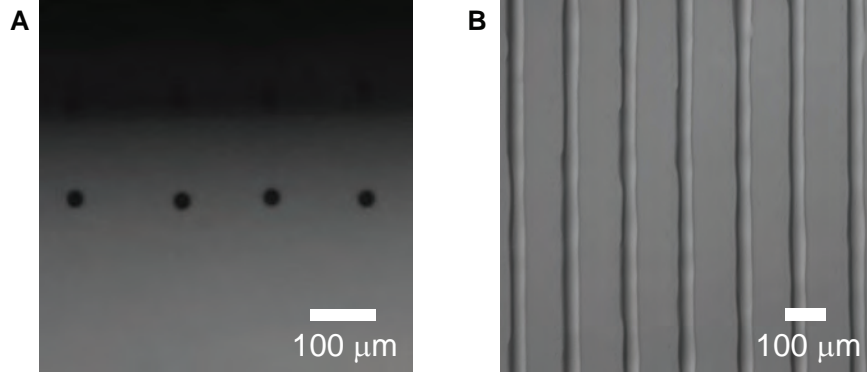


Figure 2-2: **Droplets and resolution** **A.** Images shows droplets after ejection from 4 adjacent nozzles. The droplets are $\sim 30 \mu\text{m}$ in size and the nozzle spacing is $\sim 140 \mu\text{m}$. **B.** Lines printed from adjacent nozzles show the lateral resolution of the printing process.

as follows

$$Oh = \frac{\nu}{\sqrt{\rho\gamma a}} \quad (2.1)$$

where ρ , ν , γ are the density, dynamic viscosity and surface tension respectively, and a is the nozzle size. In short, at low Z , the dynamic viscosity dominates the picture, and ink ejection is prevented. Where as at high Z , the inertial forces are too large and this results in many satellite droplets and unwanted spraying. The ideal condition for droplet ejection is the generation of one droplet per actuation cycle with clear separation of the droplet tail. In order to enforce this, we use a droplet-in-flight analysis system with stroboscopic illumination (jetXpert) to observe the droplets as they leave the nozzle (Fig. 2-2A). The droplet ejection force can be controlled by changing the actuation pulse and the waveform that is used to drive the piezoelectric stack corresponding to each nozzle. The actuation waveform contains 1-3 pulses to eject a single droplet, and is optimized manually for each ink. The number of pulses, their amplitude, and duration of these pulses control the droplet volume, ejection velocity and the shape of the droplet. The optimized droplet waveform for each ink is used as an input in the printing process. Prior to optimizing the droplet waveform, the ink viscosity and surface tension are tuned to printable range for our printhead (viscosity typically in the range 2 - 12 cP, and surface tension 40 - 50 mN/m). Ink rheology optimization and waveform optimization are performed outside the printing

platform. Once the inks are optimized they are loaded in the printer for printing as described earlier.

The inks described in this thesis are typically processed in one of three ways as highlighted in Fig. 2-3. One category of inks, i.e. UV curable inks, contain acrylate based monomers, oligomers, UV photoinitiators and crosslink inhibitors. The monomer and oligomers of the mixture can be varied to create final polymers with varying properties including a wide range of mechanical properties. The photoinitiator generates free radical when exposed to 365 nm UV light and the monomers and oligomers form chemical crosslinks as a result. The degree of crosslinks is also dependent on the concentration of the photoinitiators. The crosslink inhibitors are used to prolong the pot life of the ink by preventing the formation of crosslinks under low intensity exposure. In this thesis several variants of the acrylic ink are used in subsequent chapters: a rigid formulation (RIG), elastic formulation (ELA), a material with inbuilt residual stress (STR), and magnetic nanoparticle composite ink (MPC). The full formulations are listed in the appendix. All these inks are printed with the heated printed maintained at 70°C, and then UV cured.

The second category of inks, shown in the middle of Fig. 2-3, are liquids which are printed into wells defined in the printed part. These liquids are subsequently capped by the UV curable materials described earlier. Two main use case scenarios for these inks in this thesis are: (i) hydraulic transmission of force using water or other liquids like mineral oils, and (ii) using trapped liquids as active fluids, like liquid electrolytes in an electrical transistor. It is also possible to use a similar strategy in drug encapsulation³⁴ and to design batteries containing liquid electrolytes.

The third main processing strategy, for solvent-based inks, is to print liquid traces that are then heated from the upper side using a convection heater. A copper block was designed with air flow channels inside it, and attached to with a compact ceramic heater which is the heating element. The ceramic heater can be rapidly heated to a temperature of up to 400 °C. After printing the liquid traces, hot air is turned on locally over regions containing the liquid patterns. This techniques allows generating extremely thin films with sub-micron layer thickness. A similar approach is also

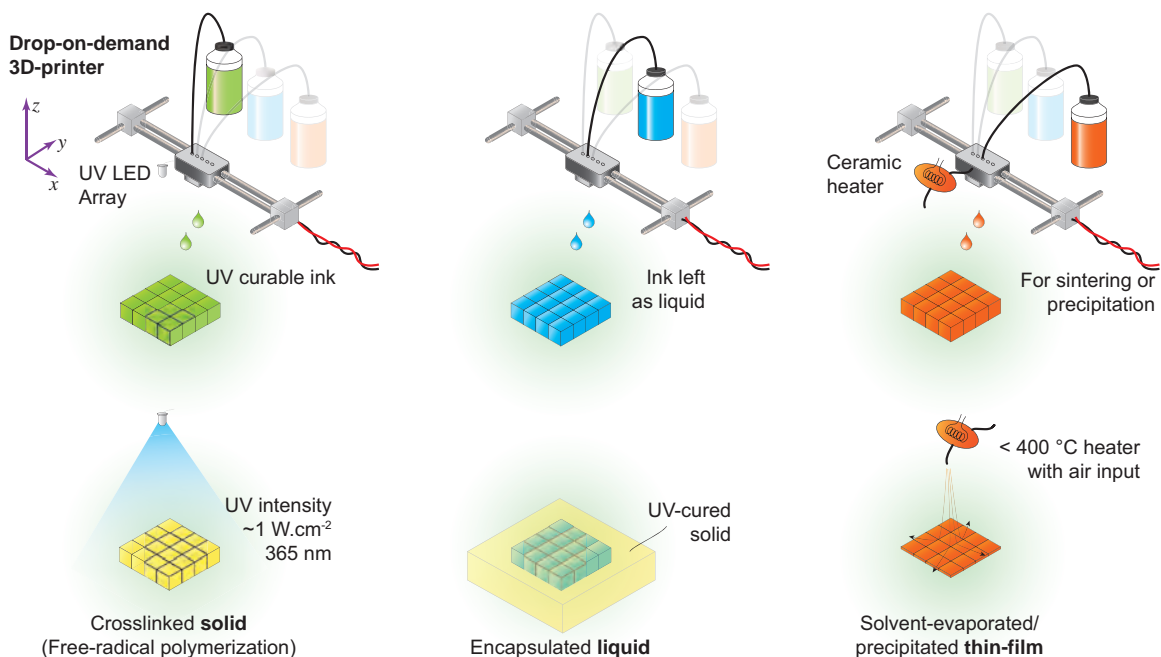


Figure 2-3: **Processing ink to material.** All inks used in this thesis are processed in one of three ways. The ink that results in the matrix materials contain acrylate monomers, oligomers and photoinitiators and photoinhibitors. The ink is UV cured using an LED array (365 nm) with a typical intensity of 1 W/cm^2 as shown in the left. Some inks are printed as liquids inside small wells and subsequently encapsulated in the liquid state inside UV curable matrices as shown in the center. The third category of inks are those which contain solvents. These inks are typically printed onto an underlying material and are sintered to remove the solvent or heated to induce precipitation.

used to precipitate nanoparticles from a silver amine complex ink in the next chapter. Overall, this approach is used to generate thin solid films from liquid ink, and specifically used to generate conductive and semiconducting traces here.

2.3 Material interface engineering

Controlling material interfaces is essential for obtaining high-fidelity patterns during the printing process as well as increasing the physical robustness of multimaterial interfaces. We use three main techniques to engineer the interfaces between solids, liquids and thin-films. They are described in detail below.

2.3.1 Effect of surface energy

When a ejected droplet lands on a surface, its impact velocity, surface tension and the surface energy of the underlying material play an important role in determining the drop shape post impact. Immediately after impact, droplet spreading is controlled by inertial forces. The ejection velocity is optimized to reduce splashing on impact. When splashing is avoided, the rest shape of the droplet is primarily determined by the capillary forces²⁵. This is where the surface tension of the ink, described in the previous section, plays a role. Here we carefully consider the surface energy of the cured materials. Rigid polymer (RIG) and the elastic polymer (ELA) are the two main matrix materials used in this thesis. To study the surface energy of RIG and ELA, droplets of deionized (DI) water, ethylene glycol and diiodomethane were used as probe fluids. Figure 2-4 shows 1 μ L droplets of DI water, ethylene glycol and diiodomethane resting on RIG and ELA surfaces. The surface tension of the probe fluids (apolar Lifshitz-van der Waals component γ_L^{LW} , Lewis acid γ_L^+ , Lewis base components γ_L^-) are known, and listed in Table 2.1. The measured contact angles are listed in Table 2.2. Contact angles were measured using the VCA-2000TM Video Contact Angle System Goniometer (AST Products Inc., Billerica, MA, USA) The values are averaged from 12 measurements of the contact angle in each condition. Using the contact angles and the known surface tension values of the probe fluids, the

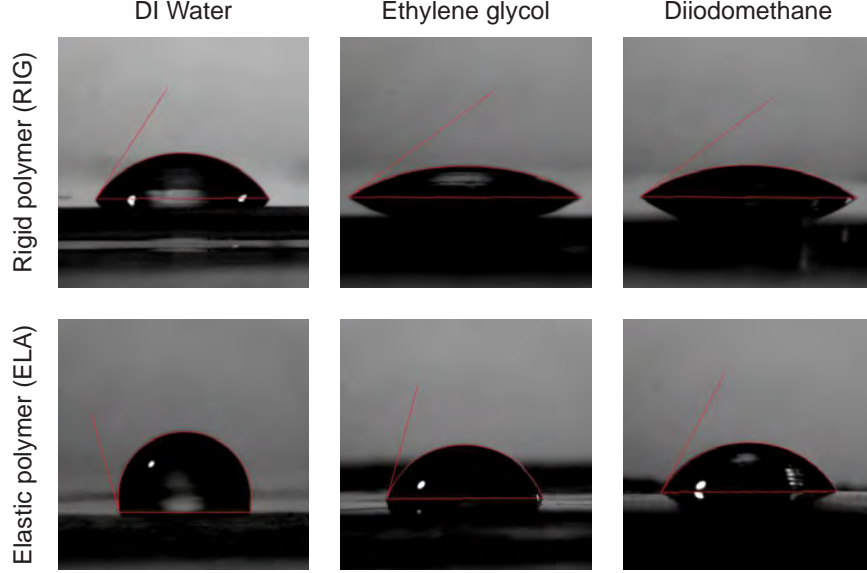


Figure 2-4: **Surface energy.** Images of 1 μ L droplets of DI water, ethylene glycol and diiodomethane on RIG and ELA substrates.

surface energy of RIG and ELA can be extracted using the van Oss-Good-Chaudhury approach³⁵, by solving the Young equation with each probe liquid:

$$(1 + \cos\theta) \gamma_L^{tot} = 2 \left(\sqrt{\gamma_s^{LW} \gamma_L^{LW}} + \sqrt{\gamma_s^+ \gamma_L^-} + \sqrt{\gamma_s^- \gamma_L^+} \right) \quad (2.2)$$

where θ is the contact angle, γ_L and γ_s are the surface tension of the probe fluid and surface respectively. The apolar Lifshitz-van der Waals, Lewis acid and Lewis base components, and the total value are denoted by the superscripts LW , $+$, $-$ and tot respectively. The three unknowns in the equation are γ_s^{LW} , γ_s^+ and γ_s^- and therefore three probe fluids are used to solve for the unknowns. The total surface energy of the substrate is a sum of the apolar and polar components, $\gamma_s^{tot} = \gamma_s^{LW} + \gamma_s^{AB}$. The polar component γ_s^{AB} is computed as $\gamma_s^{AB} = 2\sqrt{\gamma_s^+ \gamma_s^-}$.

Using this approach the surface energy terms of RIG and ELA are calculated and shown in Table 2.3. The total surface energy of RIG is obtained as 45.23 mJ/m² and the corresponding value for ELA is 28.65 mJ/m². It is evident that the polar component is negligible compared to the Lifshitz-van der Waals component as expected since our crosslinked polymers are not polar. Further, it is noteworthy that the ELA and RIG polymers differ significantly in their surface energies. This is useful later

Table 2.1: Surface tension of probe liquids

Probe Liquid	Surface energy and components [mJ/m ²]			
	γ_L^{LW}	γ_L^+	γ_L^-	γ_L^{tot}
Diiodomethane	50.8	0	0	50.8
Ethylene glycol	29	3	30.1	48
DI water	21.8	25.5	25.5	72.8

Table 2.2: Contact angles of probe fluids on RIG and ELA

Substrate	Measured contact angle, (θ) [°]		
	Deionized water	Ethylene glycol	Diiodomethane
Rigid polymer	60.10 ± 4.54	30.86 ± 3.37	35.29 ± 2.55
Elastic polymer	100.82 ± 1.93	72.71 ± 6.34	60.43 ± 3.96

in coating active surfaces to tailor the surface energy prior to printing liquid inks on top.

When a pattern is to be printed, the droplets are positioned such that they coalesce into the desired pattern. Droplet spacing can dictate whether a row of printed droplets remain separated or form a smooth line or bulge³⁶. The process parameters like velocity and droplet spacing together with surface energies require optimization for obtaining high pattern fidelity. The droplet deployment sequence also can be controlled.

2.3.2 Voxel filling

Multple printing passes are required to print any filled region, as shown in Fig. 2-5A - this is to an extent set by the printhead geometry. It takes 4 printing passes at

Table 2.3: Surface energy of cured RIG and ELA

Substrate	Surface energy, [mJ/m ²]		
	γ_s^{LW}	γ_s^{AB}	γ_s^{tot}
Rigid polymer	41.89	3.33	45.23
Elastic polymer	28.33	0.32	28.65

a minimum to cover a region smaller than the printhead width of 1" with a droplet (or voxel) size of $\sim 35 \mu\text{m}$, and nozzle separation of $140 \mu\text{m}$. In the case of a 10×9 voxel patch, 3 adjacent nozzles are fired continuously to fill the rows numbered 1. Prior to the second pass, the printhead is moved by $35 \mu\text{m}$ and all the '2' voxels are printed, and so on. This is the quickest way to fill a patch. However this is also the least tolerant of process imperfections. For instance, one clogged nozzle or misfiring nozzle will leave at least one (and up to three) row empty when nozzle rotation is not utilized. By default, nozzle 'a' in this schematic represents the same physical nozzle on the printhead across the 4 passes. However when nozzle rotation is used, a different physical nozzle is used for the nozzle 'a' across the 4 printing passes. This averages out the nozzle performance across the print.

The pattern can also be interleaved into many pseudo-layers to fill the area more uniformly as shown in Fig. 2-5B, C. In this case, it is interleaved as 3 pseudo-layers, and requires 12 printing passes in total. This interleaving approach also reduces asymmetric droplet spreading. In this case, the droplets also have more time to reach the spread state, and nozzle errors are more uniformly distributed across the print when nozzle rotation is used. This is one of many possible interleaving strategies used in the printing process.

2.3.3 Surface texture

When UV curable materials are printed and cured during the printing process, surface ripples with a spatial wavelength of $35 \mu\text{m}$ are common since the real printed voxel does not have a flat top as ideally represented. This can be both useful or a hindrance. However these ripples on the surface can be smoothed out significantly by introducing a delay between droplet deployment and curing. The tradeoff here is the blurring of edges of the printed pattern during this time. This can however be useful since by default surface ripples increase the area of a contact between two materials when printed on on top of the other.

It is also useful to intentionally define macroscale surface texture as shown in Fig. 2-6A. In this schematic, the contact of a printed electrical device is shown. Here the

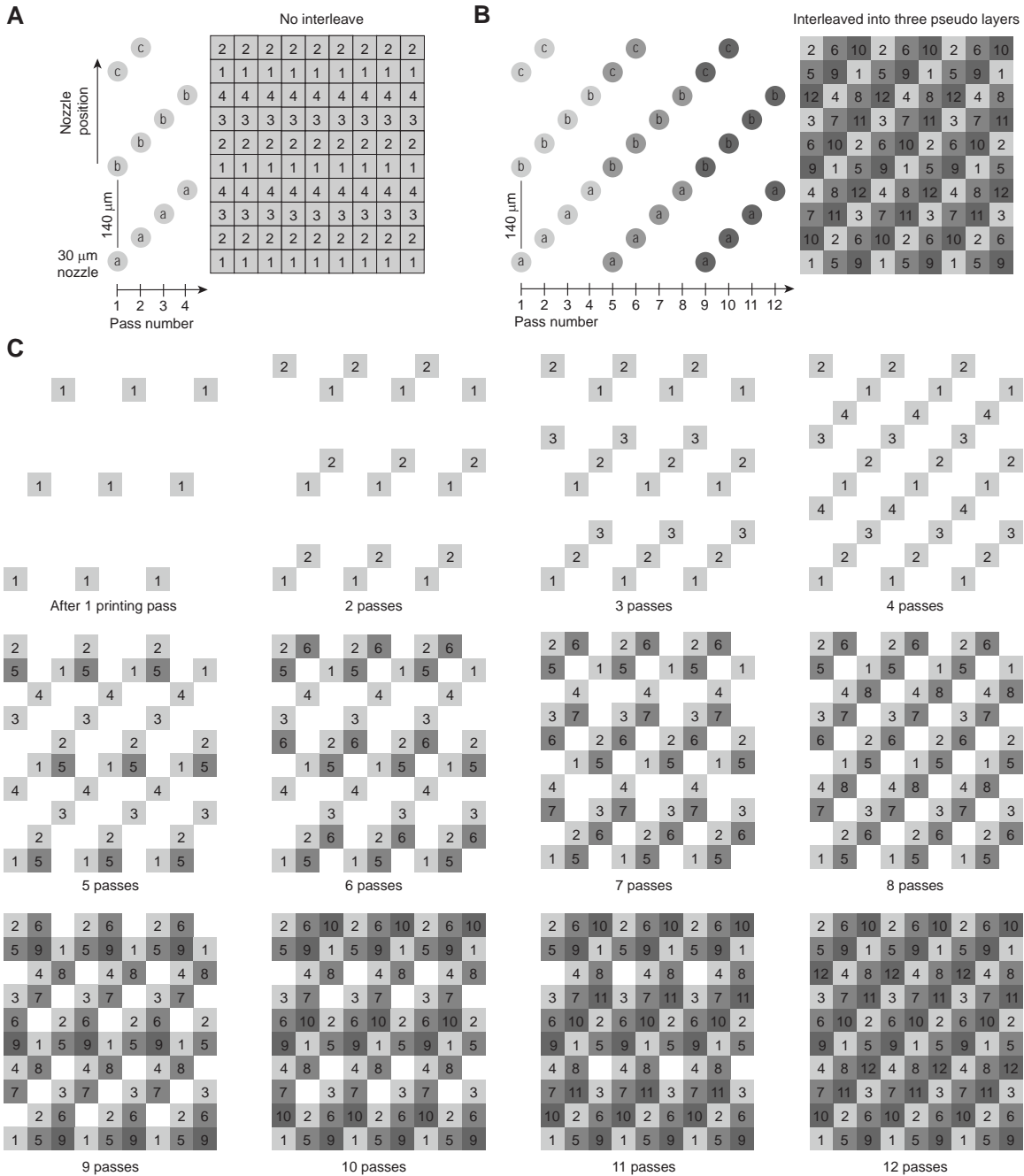


Figure 2-5: **Voxel filling.** **A.** Schematic shows the default way to fill a 10×9 voxel patch. ‘a’, ‘b’ and ‘c’ indicate three consecutive nozzle positions and the number inside each voxel shows the printing pass at which these voxels are printed. **B.** Instead, a patch can be separated into 3 layers, each requiring 4 passes to print. **C.** This approach requires 12 printer passes to print a patch. While slower, this process fills a pattern more uniformly through the area of the patch. When nozzle rotation is used, this strategy can distribute the effects of nozzle failures across the print.

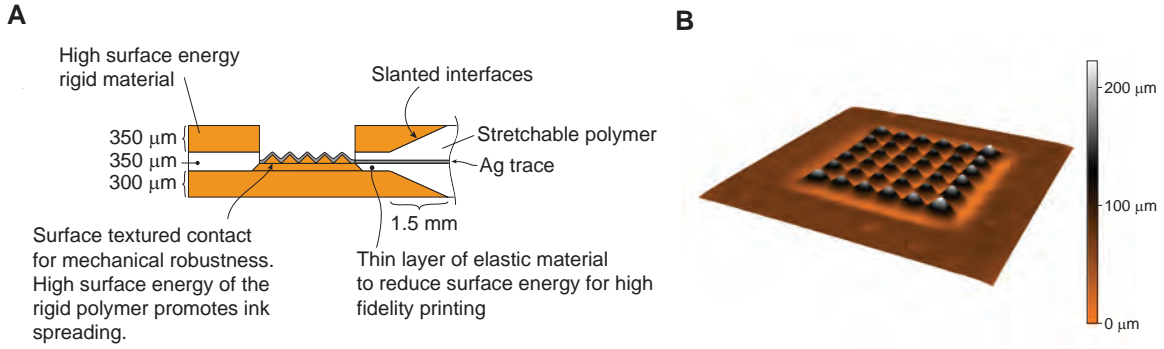


Figure 2-6: **Textured contact.** **A.** Schematic shows an electrical contact design in a printed device. The textured contact window and the slanted interfaces are of interest here. **B.** The height map of the textured contact measured using the Gelsight system.

encapsulated silver trace terminates in an open window for making external electrical connections. The silver trace, in this case is printed on to a pyramidal texture defined in a rigid matrix to prevent the silver trace from being scratched easily. The measured surface geometry of the textured contact region is shown in Fig. 2-6B.

2.3.4 Geometric control of interfaces

In many devices in the upcoming chapters, soft materials are printed together with rigid materials (with elastic modulus varying by over 3 orders of magnitude). These interfaces are inherently interesting since materials that experience high strains are brought together with nearly 0 strain materials. These interfaces can become prone to failure due to interfacial strain discontinuities. Controlling the geometry of the interface can be an effective strategy to engineer tough interfaces³⁷.

One such example is shown in the simplified schematic of the contact design in Fig. 2-6 where slanted non-planar interfaces increase the interface area between the stretchable polymer and the rigid substrate. In summary, material interfaces can be engineered at many levels of the printing process, but also in the material design and the device geometry.

Chapter 3

Autonomous sensory composites

Insects like the Golden tortoise beetle (*Charidotella sexpunctata*) shown in Fig. 3-1, can change the transparency of their exoskeleton quickly in response to mechanical stress. This reaction is enabled by a network of sensors and actuation mechanisms part of their broader sensorimotor network that are seamlessly connected inside this small insect. Integrating elements of sensing with processors and actuators within single composites opens up a route to autonomous sensory composites inspired by nature. Motivated by this, we describe a *monolithic* integration of strain sensitive elements with an organic electrochemical transistor (OECT) based amplifier and electrochromic pixels. A mechanical stimulus is picked up by our strain sensor, amplified electrically by a single-stage amplifier and the transparency is modulated in the optical actuator, all within a fully-printed composite powered by 1.5 V.

3.1 Fabrication of sensory composites

In emerging applications that demand sensorimotor analogues, such as in robotics and electronic skins^{38,39}, laminates of separately-made high performance sensors⁴⁰

Contents of this chapter are adapted with permission from - S. Sundaram, Z. Jiang, P. Sitthi-Amorn, D. S. Kim, M. A. Baldo, W. Matusik, “3D-printed autonomous sensory composites”, *Adv. Mater. Technol.*, 2, 1600257 (2017). <https://doi.org/10.1002/admt.201600257> [Copyright John Wiley and Sons].

Golden Tortoise Beetle

Charidotella sexpunctata, *Charidotella egregia* etc.



Reflective exoskeleton



Transparent exoskeleton

Figure 3-1: **Golden Tortoise Beetle.** Insect like the Golden tortoise beetle can modulate the transparency of their exoskeleton. In its default state, the beetle has a reflective golden shell. When disturbed, the beetle can drain fluid from its exoskeleton and appears red. *Image credit: Ken Sproule*

and external processors manufactured using several techniques have been used. This progress has been enabled by advances in stretchable materials⁴¹⁻⁴³ and ultralight organic electronics^{44,45}. Solution processed and printable designs have also emerged from the need for low-cost, large-area manufacturing,^{27,46-51} in parallel inspiring our work. Most current approaches to fabricate sensory composites rely on the external assembly of individual components produced from multiple processes, often limiting topology and density.

New additive manufacturing techniques enable the rapid creation of functional parts made of advanced materials in complex shapes^{15,52} with multidimensional control⁵³. However, 3D-printing is nascent and few functional electronics have been demonstrated so far. Strain sensors²¹, quantum dot light-emitting diodes²⁰ and passive components have been 3D-printed but demonstrations of active circuits and large integrations of elements are still missing.

We present a low-temperature additive manufacturing process to achieve an integration of strain sensitive elements, organic amplifiers and electrochromic elements using the integration scheme shown in Fig. 3-2. The solid supporting matrix consists of UV curable rigid (RIG) and elastic (ELA) layers. The strain sensor is defined in

the ELA regions and the amplifier and the electrochromic pixel are written on to the RIG matrix. RIG (elastic modulus ~ 637.76 MPa) and ELA (elastic modulus ~ 678.5 kPa) span three orders of magnitude in stiffness, as shown in Fig. 3-3.

The RIG and ELA UV curable polymer inks are printed simultaneously using the heated printhead to form the substrate layers, which are $700\ \mu\text{m}$ high including the pyramidal contact regions - using the interleaving technique. When the functional inks, PEDOT:PSS and silver ink, are being printed, the heater passes are activated to evaporate the solvent every two layers. At this stage, the ceramic heater moves over the regions containing solvents and traverses back and forth for 10 cycles with the air pump turned on/off automatically, taking ~ 1 min in total. This rapid heating cycle does not seem to have any detrimental effect on the material properties of the underlying substrate since only small regions of the uppermost print layers are exposed to hot air at any time. When silver ink is printed, the patterns made with the nearly transparent silver ink turn white-silver in appearance, signaling formation of silver nanoparticles and the completion of liquid evaporation. The sidewall layers, which are printed next, contain both the rigid and elastic polymers, which are printed using the same settings as the substrate regions. The electrolyte is printed into the wells defined in the elastic material. The print is then sealed with a $500\ \mu\text{m}$ thick rigid capping layer. At the completion of printing, the two strain sensor arms of the print are $1\ \text{mm}$ thick in total and the rigid electrical region is $1.5\ \text{mm}$ thick. The devices were made thick to demonstrate the ability to print thick composites, showing potential for printing complete functional parts. We will now look at the properties of the individual components in detail.

3.2 Printed strain sensor

The strain sensor consists of 3 different materials, each with a specific purpose. The RIG layers form the rigid electrical contacts, while the ELA is the stretchable region containing the active material (silver trace), as shown in Fig. 3-4A. The sensors are designed such that the contacts are rigid ensuring that the contacts are unaffected

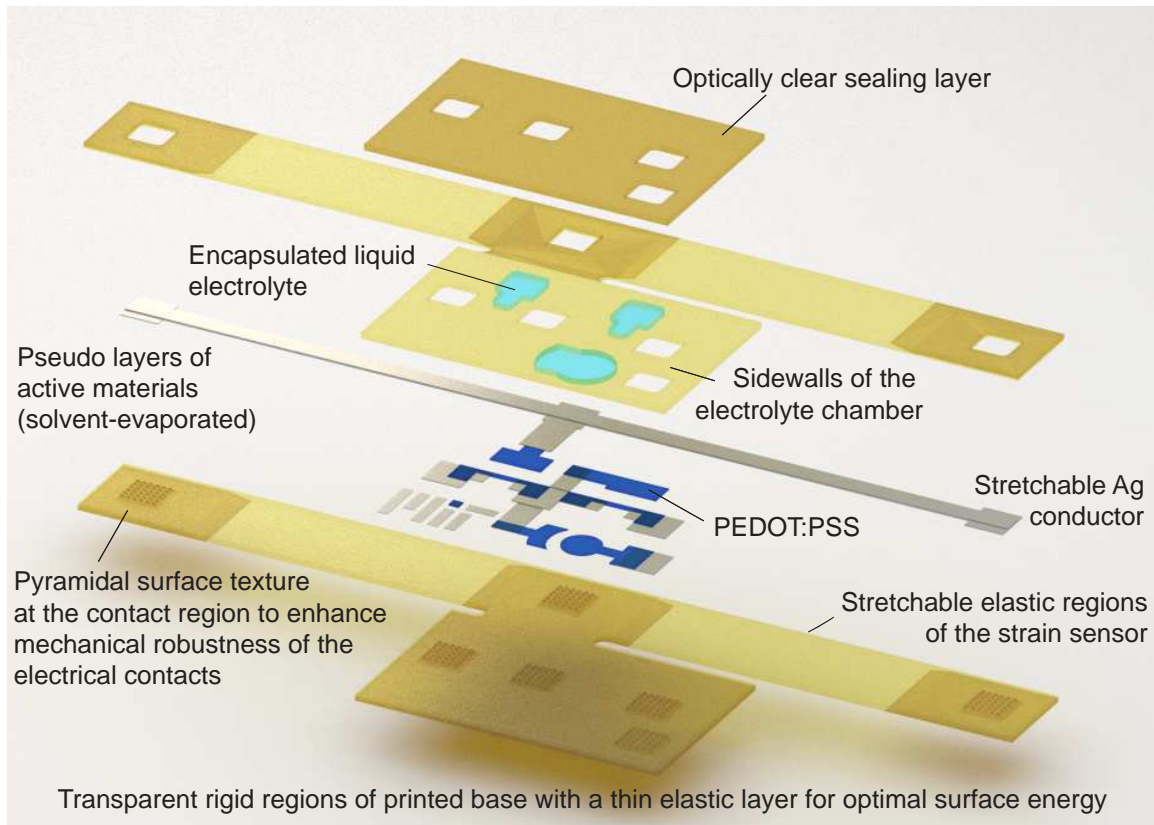


Figure 3-2: **Schematic of the autonomous sensory composite.** The composite is grouped into 4 sets of functional layers: a base with spatially varying mechanical stiffness and surface energy, electrical materials, electrolyte, and capping layers. All these materials are printed. The base is formed from droplets of UV curable acrylic polymer. Uppermost layers of the base consist of thin surface energy engineered elastic ELA layers to facilitate proper definition of solvent-based inks. Electrical contact regions of the base are textured with pyramids for mechanically robust contacts. Silver traces are obtained by precipitating silver from a liquid ink by local forced convection heating. The elastic matrix with silver nanoparticles forms a stretchable conductor. Thin poly(3,4-ethylenedioxythiophene) polystyrene sulfonate (PEDOT:PSS) layers are obtained by solvent evaporation and are used as the active semiconductor and electrochromic material. The printed conductive and semiconductor materials are capped by UV curable polymers and wells that hold the electrolyte, defining the active transistor geometry. The uppermost optically clear layer seals the electrolyte exposing only the electrical pads. This scheme shows the integration of elements with varying mechanical and dynamically-tunable electrical and optical properties in freeform architectures.

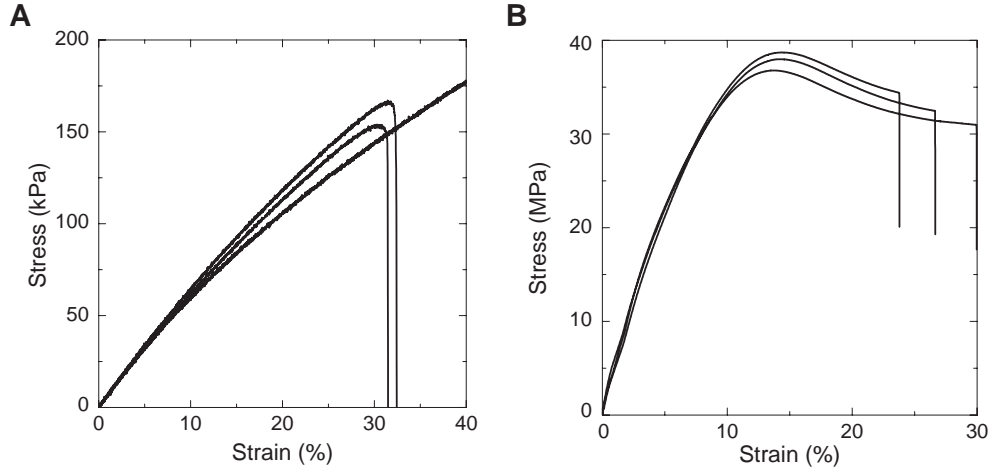


Figure 3-3: **Mechanical properties of the UV curable materials.** **A.** Measured stress plotted as a function of strain for three printed elastic (ELA) samples each 7 mm wide, measured at a strain rate of ~ 10 % per minute. The linear elastic modulus of the averaged stress-strain curve is 678.47 kPa at 0.5% strain. **B.** Stress-strain plot for three samples printed with the rigid material (RIG), with an elastic modulus of 637.76 MPa

when deformed. The transition from the rigid contacts to the active elastic matrix is gradual, preventing delamination at the interface, as shown in Fig. 3-4A.

The active material in the strain sensor is formed by rapid heating of the printed silver ink, facilitating the formation of silver nanoparticles by a reduction reaction. Typically 8 layers of the silver ink (with heater passes every 2 layers) results in a 10 μm thick strain sensitive resistor. The silver traces are sandwiched within the elastic polymer (scanning electron microscope image in Fig.3-4B). Elastic region at the middle of the sensor is 20 mm long transitioning to a predominantly rigid substrate at the contacts over 1.5 mm. All our sensors show a linear resistance change as a function of applied strain with no visible hysteresis for small deformations ($\sim 5\%$). Figure 3-4C shows the resistance as a function of strain when the sensor is cycled uniformly at 10 mm/min, for varying maximum strains of 5%, 10%, and 20%. The linear gauge factor (GF) of the sensor at small strains is 102.94. Our sensors show a small reduction in resistance around 5% elongation. We hypothesize that precipitated nanoparticles are brought closer in the vertical direction as the sensor is stretched horizontally leading to a competing enhanced conductance. On stretching the sensor

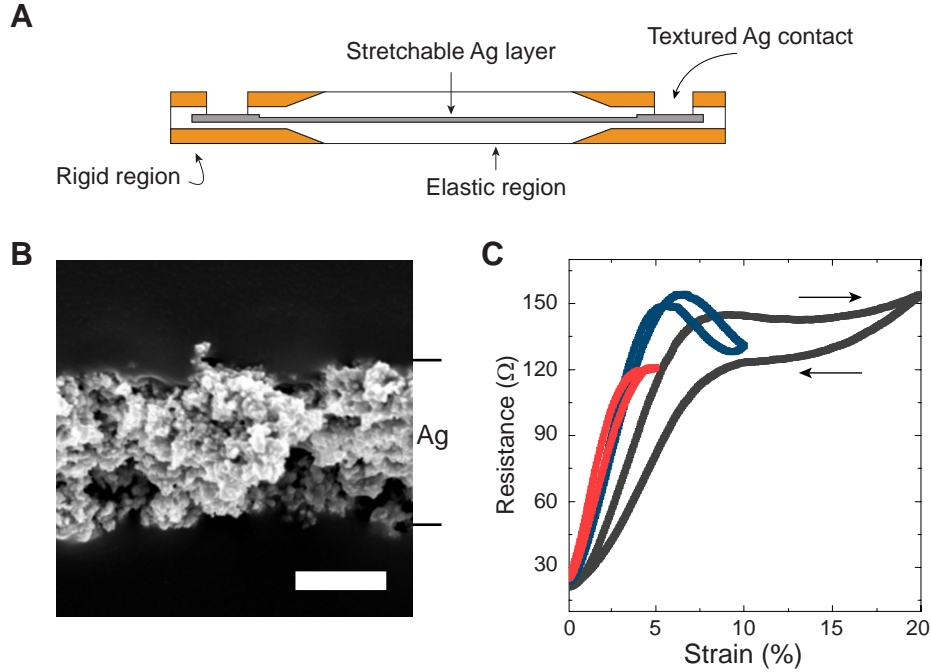


Figure 3-4: **Strain sensor design and performance.** **A.** Cross sectional schematic of the strain sensor. **B.** Scanning electron microscope image of the silver trace sandwiched between ELA regions on each side (Scale bar 5 μ m). **C.** Strain response of the strain sensor for various strain levels. The response is linear for \sim 5% strains with little hysteresis. When stretched to 20% strains, there is significant hysteresis and nonlinearity.

to 20% strain, the device exhibits hysteresis but shows no remnant offsets over cycles (see Fig. 3-5A, B). The strain sensors function until mechanical breakage of the polymer (Fig. 3-5C).

In order to evaluate the expected variation in their performance, sensors were fabricated in individual printing runs and the results are shown in Fig. 3-6A. A small variation exists between sensors printed across 5 runs. However, the variation between the two connected matched sensors in the final composite is expected to be even lower than shown above due to the devices being in the same composite in immediate proximity. Further, the steep slope in the resistance-strain curve close to 0% strain alleviates the effect of a minor mismatch when configured as a resistor ladder. The average gauge factor of these sensors at small strains (linearized at 2%) is 136.57 (best device has a gauge factor of 460.81, and the device with the highest base resistance has a gauge factor of 16.75). This gauge factor compares favorably

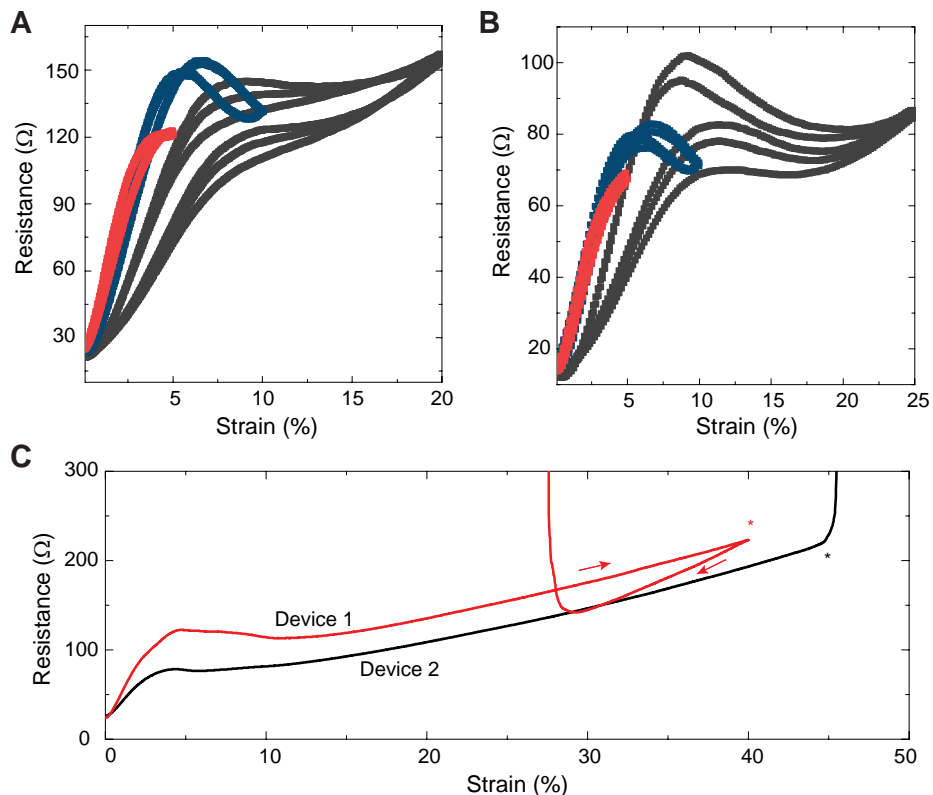


Figure 3-5: **Strain sensor under high strain.** **A.** Typical resistance-strain characteristics of a single sensor when stretched to 5% (red), 10% (blue) and 20% (gray). Multiple cycles of the device performance shown in Fig. 3-4C is shown here. **B.** Resistance-strain characteristics of another device with an identical configuration is shown here. **C.** Two devices were stretched until failure to observe the failure mode. Despite the mild nonlinearity at $\sim 5\%$, both devices remain functional until mechanical failure of the part caused by the breakage of the elastic matrix. Device 1 failed when a tear was initiated at 40%, and physically separated in the return to 0 strain. Point of tear initiation is shown by ‘*’. Device 2 failed at $\sim 45\%$ strain.

(same order of magnitude) with previous reports for colloidal nanoparticle based resistive strain sensors. Prior work has shown that large nanoparticle based resistive strain sensors show more enhanced hysteresis from increased disorder in the overall nanoparticle stacking and assembly⁵⁴.

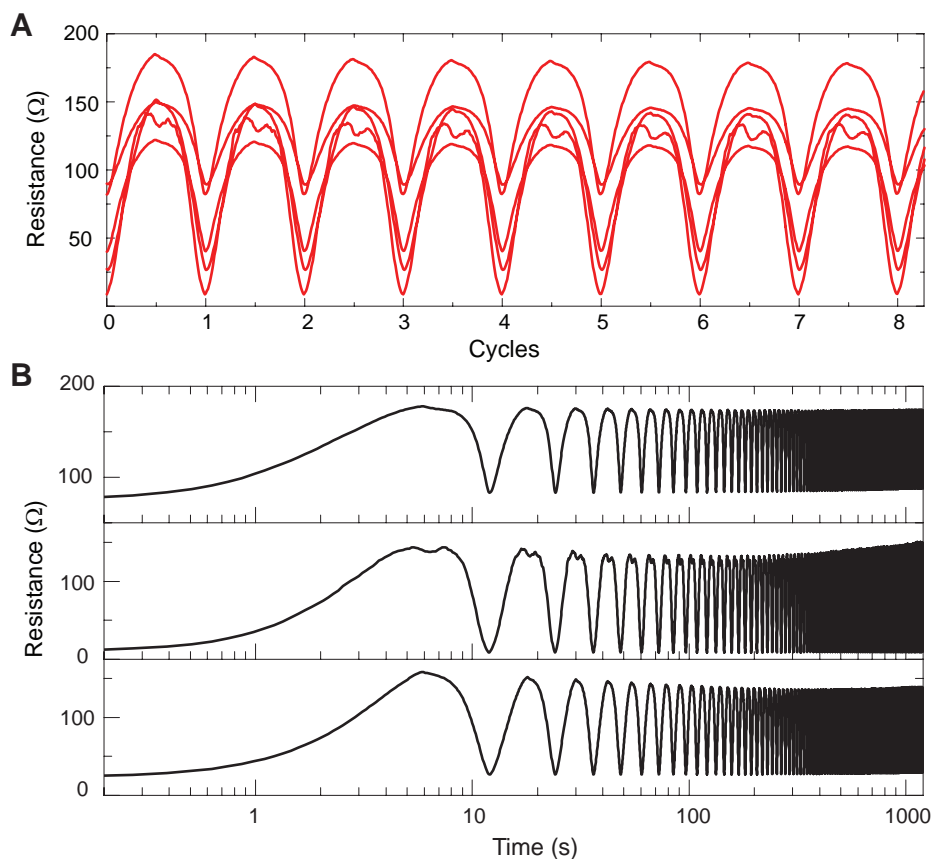
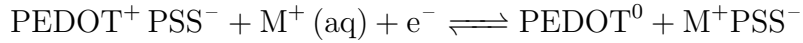


Figure 3-6: **Strain sensor - repeated cycling.** **A.** Sensors were printed in five individual runs to analyze repeatability of the process. The plot shows the resistance of these 5 sensors cycled to 5% strain at 10mm/min (50% strain/min). **B.** To test the long term performance, the sensors were cycled for 1200s for strains up to 5% (100 cycles at 10mm/min). The plot shows the resistance as a function of time for three sensors

3.3 Organic electrochemical transistors (OECTs) and amplifiers

Our printed OECTs are shown schematically in Fig. 3-7A. The substrate is made with a thin layer of ELA on top of RIG. The ELA layer is added to tune the surface energy of the substrate prior to printing the PEDOT:PSS layer. Both the channel and the gate are made with PEDOT:PSS and are bridged by a water-based electrolyte containing potassium ions. The electrolyte is encapsulated inside a well that defines the channel dimensions. Further, the sidewalls ensure that the silver contacts are not exposed to the halide rich environment, preventing large leakage currents⁵⁵. The channel of the depletion mode OECT is de-doped by the physical movement of metal ions from the electrolyte when a positive gate voltage is applied:



PEDOT:PSS is by default in the oxidized state. With the application of a positive voltage on the gate electrode, metal ions from the electrolyte diffuse into the PEDOT:PSS channel due to the presence of an electric field. The metal ions de-dope the material reducing PEDOT to the neutral state. PEDOT exhibits an optical contrast between its oxidized (transparent) and reduced states (opaque).

PEDOT:PSS based OECTs operating up to ~ 1 kHz have been demonstrated so far and are capable of amplifying cellular signals⁵⁶. Typically the speed is limited by the reduction front in the device, which can be improved by utilizing different topologies using carbon paste as the source and drain contact⁵⁷. Figure 3-7B shows a scanning electron microscope (SEM) image of the PEDOT:PSS layer (~ 1 μm thick sandwiched in ELA). Transfer characteristics of a transistor with channel width (W) 500 μm and length (L) 1500 μm are shown in Fig. 3-7C, where the gate-source voltage (V_{gs}) is varied from -0.5 V to 1.25 V, with the drain-source voltage (V_{ds}) set to -0.5 V. The on/off current ratio is 9.65×10^3 with a peak transconductance (g_{m}) of 5.61 mS (this corresponds to $g_{\text{m}}/W = 11.22 \text{ S m}^{-1}$) and an average subthreshold slope of 152.4 mV/dec (Fig. 3-8A). The current-voltage characteristics are shown in Fig. 3-7D. The

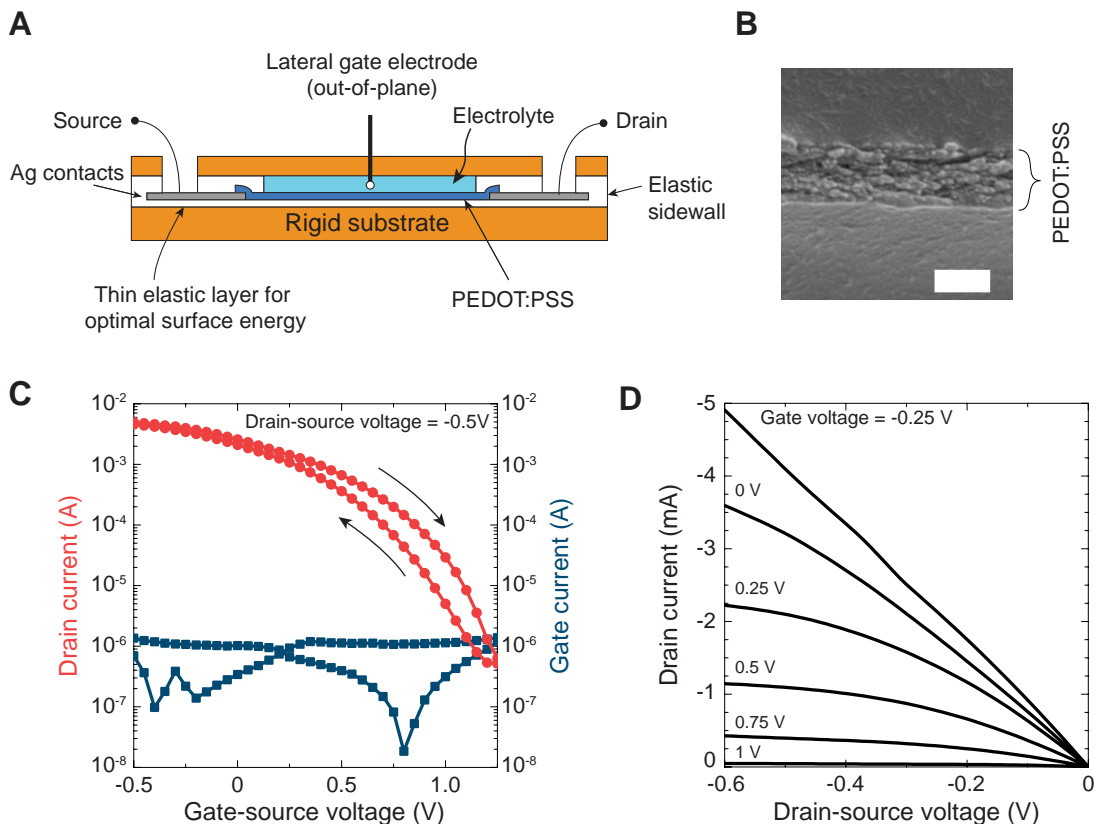


Figure 3-7: **Printed organic electrochemical transistor (OECT).** **A.** Schematic cross-section of the transistor. **B.** Scanning electron microscope image of the PEDOT:PSS layer (scale bar is 1 μm). **C.** Transfer characteristics of the printed transistor at $V_{\text{ds}} = -0.5 \text{ V}$. **D.** $I_{\text{ds}} - V_{\text{ds}}$ curves for different gate voltages.

switching times of the transistor are typically asymmetric due to the reduction front in the off state, where the off \rightarrow on transition is slower than the on \rightarrow off transient (Fig. 3-8B). This is due to the reduction front in the previous off state extending towards the electrodes (drain) which prolongs the subsequent switching to the on state in the next cycle. Figure 3-8C shows the transfer curves of 6 transistors printed in multiple runs. The current-voltage characteristics of a diode-connected transistor are shown in Fig. 3-8D.

The transistor can be connected to an active load to form the amplifier (as shown in Fig. 3-9A), where the gain is proportional to the load resistance (input-output characteristics shown in Fig. 3-8D). Here, the channel length of the diode connected transistor is $2L$ (3000 μm). As the mismatch between the channel lengths of the

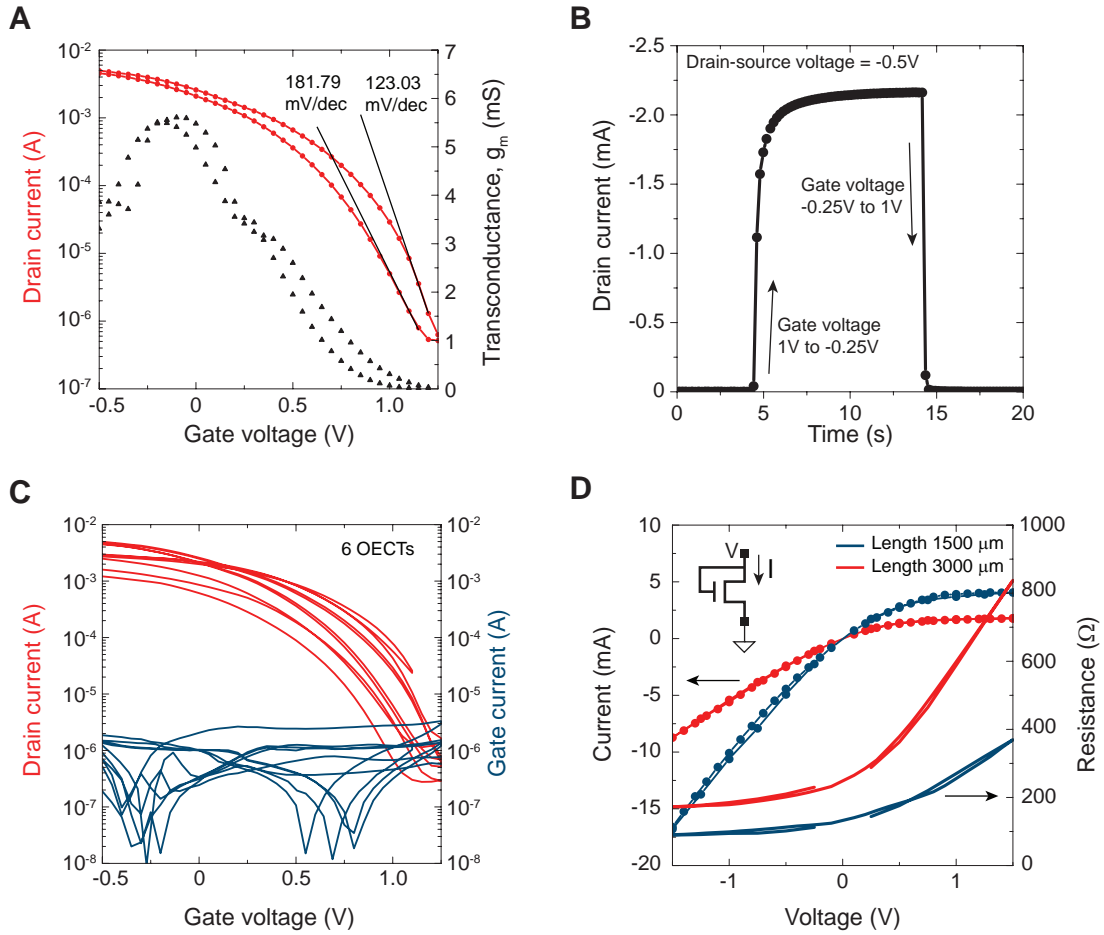


Figure 3-8: **Transistor specifications.** **A.** The transfer curves of the device shown in Fig. 3-7C, showing the subthreshold slopes during the forward cycle (123.03 mV/dec) and the reverse cycle. Transconductance, g_m , peaks to 5.61 mS, near 0 V gate voltage. **B.** Switching time of the transistor is limited by the off \rightarrow on transient switching time. Transistor has width, $W = 500 \mu\text{m}$ and length, $L = 1500 \mu\text{m}$. With the drain-source voltage set to -0.5 V, the exponential off \rightarrow on state switching rise time is 234.15 ms. **C.** Transfer curves showing the drain current and gate current measured as a function of gate voltage for 6 separate transistors printed in 3 different printing runs. Transistors show similar on/off ratios and transport properties. **D.** Current-voltage characteristics of two different diode connected transistors showing the voltage dependent effective resistance. The larger transistor is more effective as an active load for a common source amplifier showing a larger change in the resistance with voltage due to its proportionately larger channel (width, $W = 500 \mu\text{m}$)

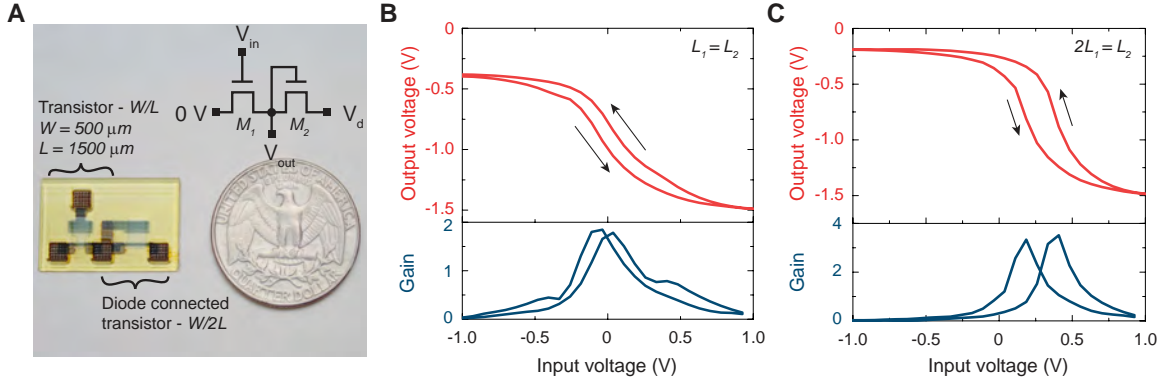


Figure 3-9: **Single-stage common source amplifier.** **A.** Photograph of a transistor amplifier with a diode connected load. Transistor width, $W = 500 \mu\text{m}$ and length, $L = 1500 \mu\text{m}$. The diode connected transistor has a length $2L = 3000 \mu\text{m}$. **B.** When instead the transistors are matched, i.e., $L_1 = L_2$, the maximum gain is centered around $V_{\text{in}} = 0 \text{ V}$. **C.** Input - output characteristics of the mismatched device shown in ‘A’ where $L_2 = 2 L_1$. Here the maximum gain is higher but the mismatch shifts the bias point for maximum gain away from 0 V .

load and the active transistor is increased, the output swing reaches closer to the ideal rail-to-rail switching characteristics while simultaneously shifting the maximum gain bias-voltage higher (see Fig. 3-9B & C). For the design of the amplifier a diode connected active load was chosen over a passive load to improve the gain. The current-voltage characteristics of the diode connected load (see Fig. 3-8D) shows that the longer device has a higher small-signal impedance. This results in the gain of the amplifier with the larger load being higher compared to the case where the channel dimensions are matched.

3.4 Electrochromic pixel

The design of the electrochromic pixel is largely similar to that of the transistor (Fig. 3-10A). The electrochromic pixel is a two terminal device that is used to control the oxidation state of the larger PEDOT:PSS patch. As the voltage on the smaller control electrode is increased, the PEDOT:PSS layers that make up the pixel are brought to the de-doped neutral state along with an increase in opacity as shown in the image in Fig. 3-10B. The transmission through the pixel is quantified using a spectrometer

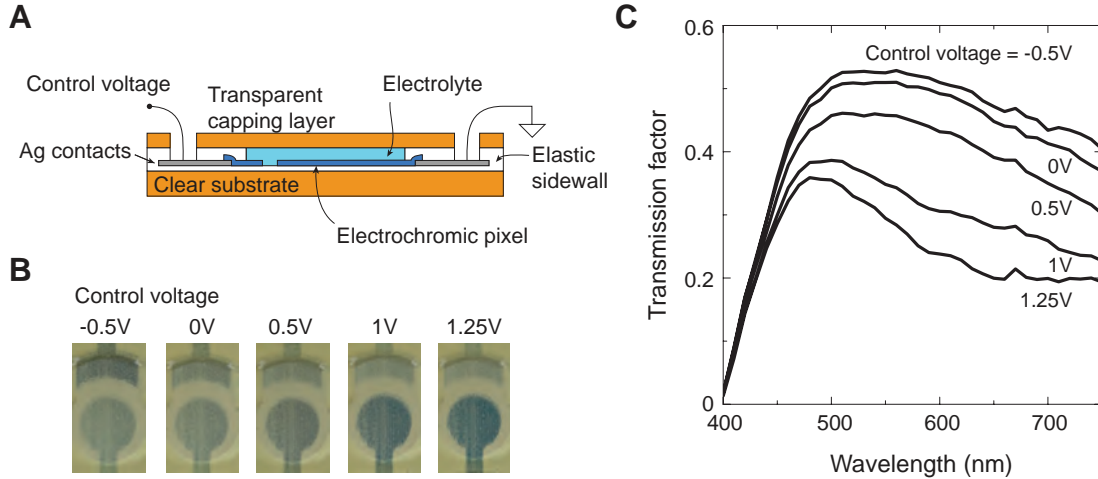


Figure 3-10: **Electrochromic pixel.** **A.** Cross sectional schematic of the electrochromic pixel. **B.** Optical images of the pixel as the voltage on the control electrode is cycled from -0.5 V to 1.25 V . The circular pixel is $\sim 3\text{ mm}$ in size. **C.** Optical transmission through the pixel as a function of wavelength for different control voltages, normalized with respect to direct transmission through a 2 mm aperture.

and shown in Fig. 3-10C as the function of the wavelength of light. Nearly half the light can be blocked by switching the control voltage from 0 V to 1.25 V .

Further, as shown in Fig. 3-11, the printed electrochromic pixel can be coupled with liquid filled microchannels within a single composite. This is traditionally a challenging task in conventional microfabrication. Force coupling through the channel is obtained here by encapsulating a transparent mineral oil. This device allows control of both the transparency and surface texture/shape as shown in Fig. 3-11C.

3.5 Integrating the parts

All the parts described in detail earlier are composed together in a single composite (design presented in Fig. 3-2). The strain sensor (R_2) based resistor ladder, common source amplifier, and the transparency modulator are connected together as shown in the circuit in Fig. 3-12A. The fully printed device is pictured in Fig. 3-12B. Transistors M_1 and M_2 are made identical in channel geometry to achieve maximum gain at $\sim 0\text{ V}$, which is the default voltage at the intermediate node in the resistor ladder. In this default state, the voltage across the pixel is $\sim 0.7\text{ V}$, leaving it in a

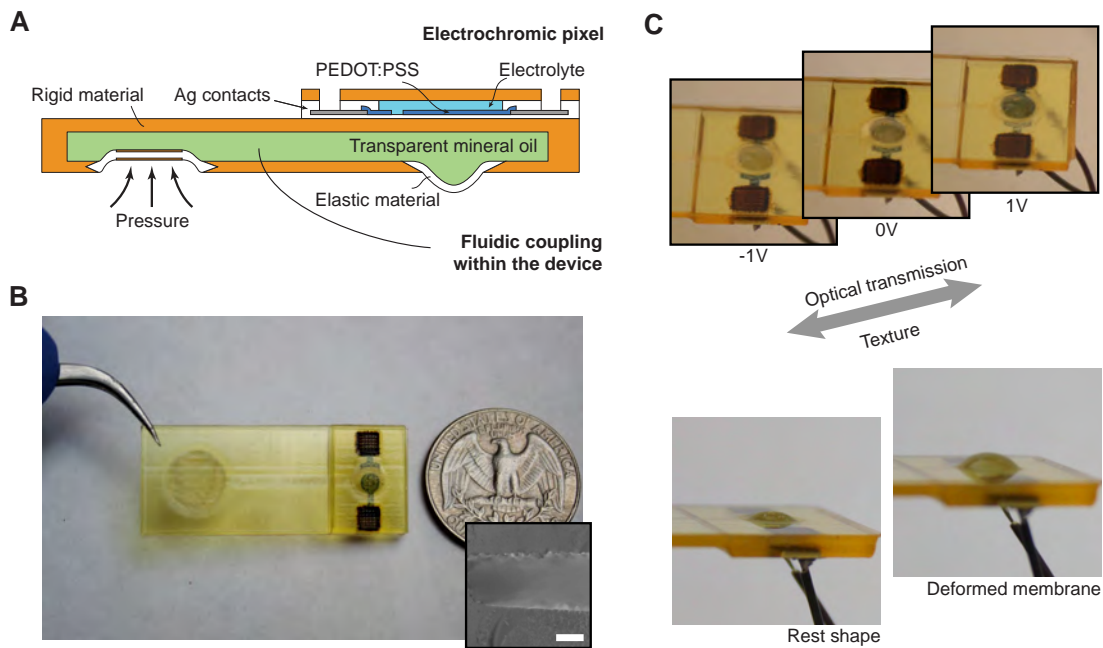


Figure 3-11: **Device with fluidic coupling to control transparency and shape.** **A.** Cross sectional schematic of the electrochromic element integrated monolithically with a microfluidic device. The fluidic channel is designed to be 500 μm thick. When a force is applied on the large enclosed reservoir, it is transmitted through the fluid and causes the elastic membrane below the electrochromic pixel to deform. **B.** Photograph of the fully printed device with 6 materials. Inset shows the cross section of the internal microchannel (scale bar - 200 μm). **C.** This allows control of both the optical transmission and shape. The control voltage is used to change the transmission. The encapsulation of fluids seamlessly with electronics demonstrates potential in microfluidics and in actuation.

dark state. As R_2 is stretched, the voltage input to the amplifier is positive, leading to a drop in the voltage across the electrochromic pixel. Figure 3-12C shows two still images from a video of the fully integrated system, highlighting the color change as the regulator (R_1) and the sensor (R_2) are deformed. The close-ups show the red channel image of the electrochromic pixel.

The monolithic integration of sensing, processing and response mechanisms shown here allows transducing signals across mechanical, electrical, and optical domains using organic processors and sensors that can be powered by 1.5 V. Merging hydraulics and electronics within a single composite containing soft materials allows control of both the shape and color as shown earlier. Overall, the biggest challenge is in integrating power sources within the composite. Reducing the need for external power sources (and wires) would be an important direction toward self-sufficiency in these autonomous sensory composites. Controlling multi-domain properties with uniform resolution and without any external processing should enable advances in biologically inspired autonomous multi-functional systems with increased levels of self-sufficiency. With room for miniaturization and a prospect for using biocompatible structural matrices, this approach could lead to compact autonomous systems that interface with or support natural biological systems.

3.6 Experimental methods

The experimental methods relevant to this chapter are summarized here. The full details of the printing process are in the previous chapter. Specific notes on the inks and characterization are included below.

Note on inks: The full list of inks and their complete formulations is in the appendix. Inks used here were prepared in our wet lab from constituent materials bought from different commercial vendors. Each ink was optimized for desired functional properties and subsequently had its rheological properties tuned as described previously to make it suitable for inkjet printing. Silver ink was prepared based on an ethanol based formulation using an approach described in a patent⁵⁸. A neutral PEDOT:PSS

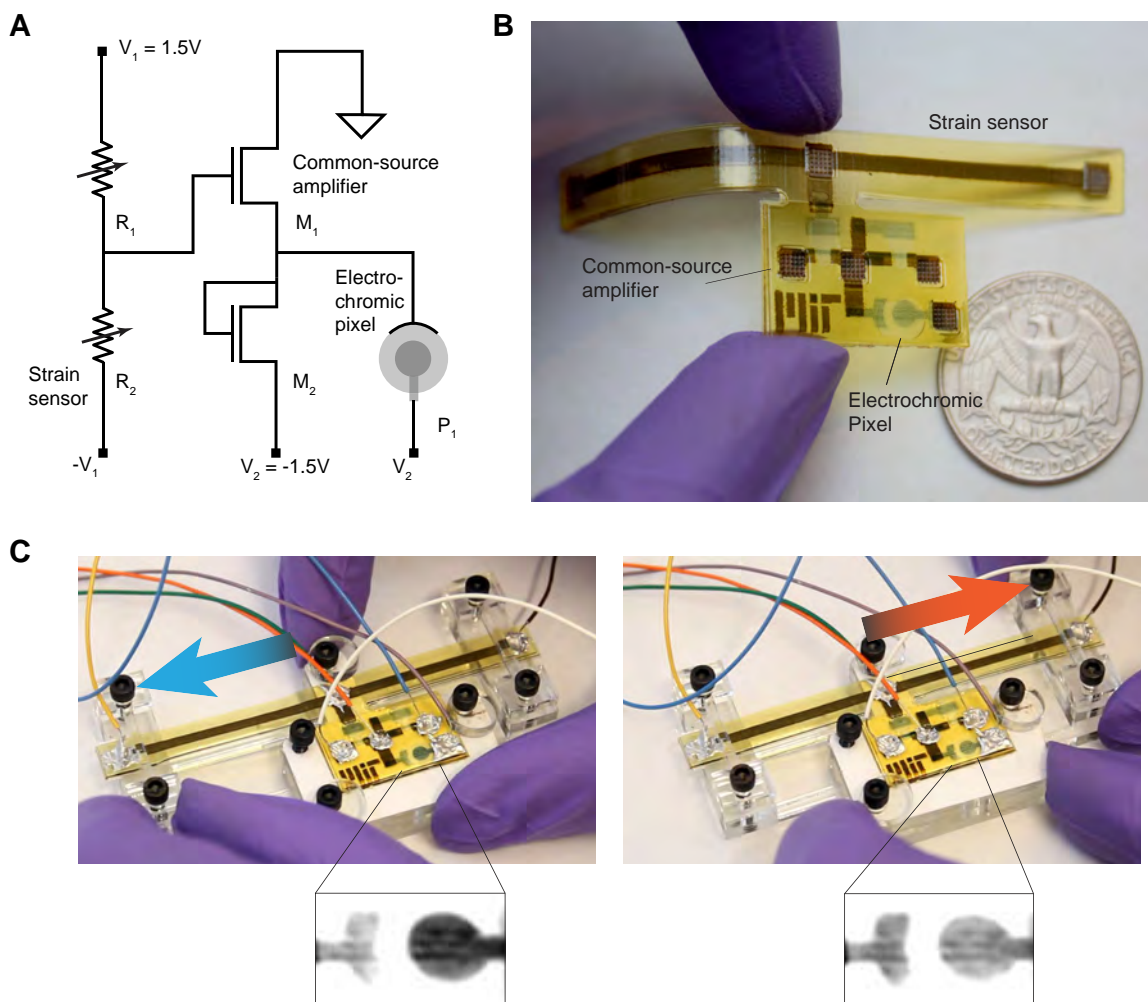


Figure 3-12: **Integrated autonomous sensory composite.** **A.** Equivalent circuit diagram of the strain sensor ladder, the common source amplifier with a diode-connected transistor load, and the electrochromic pixel. ($V_1 = 1.5\text{ V}$, $V_2 = -1.5\text{ V}$) **B.** Photograph of the fully 3D-printed autonomous sensory composite shows a strain sensor linked to an electrical amplifier that modulates the transparency of the electrochromic pixel. This composite transduces signals across multiple domains. **C.** Output at the electrochromic pixel when the left (R_1) and right (R_2) strain sensors are extended. At rest, the pixel is in the dark reduced state due to the default voltage ($\sim 0.7\text{ V}$) across the pixel. Transparency is increased when R_2 is extended, and the voltage across the pixel drops closer to 0 V . Contrast enhanced red channel information from the frames are shown in the monochrome close-up.

based formulation (CleviosTM P Jet 700N, Heraeus, Leverkusen, Germany) was mixed with 5% dimethyl sulfoxide (A13280 dimethyl sulfoxide, 99+%, Alfa Aesar, USA) to prepare the PEDOT:PSS ink used here. The liquid electrolyte used for the gate is a 0.1M solution of potassium chloride in deionized (DI) water, mixed with glycerol.

Characterization and electrical testing: Wires were attached to the open textured contacts with low temperature curing conductive silver epoxy (MG Chemicals 8331 Two-part silver conductive epoxy adhesive, Amazon, USA). The attached wires were left undisturbed overnight for the epoxy to cure at room temperature. Typically devices were tested two days after printing for uniformity. All devices were printed and stored in ambient conditions exposed to open air. It was observed that the encapsulated solution does not evaporate at least until 1-2 weeks after print. Mechanical stress-strain tests for supporting UV curable polymer materials were performed with Instron 5944 (Instron, Norwood, MA, USA), a single column table top mechanical testing system. Surface profile measurements of the textured contact were obtained using a GelSight Benchtop Scanner (GelSight Inc., Waltham, MA, USA). Printed strain sensor characterization was performed by using the Instron 5944 to strain cycle the sample, while the resistance was measured using a Keithley 2911B sourcemeter with 100 mV applied across the sample. Steady state transistor characterization and amplifier measurements were performed using an Agilent 4155C Semiconductor Parameter Analyzer. To measure the transient characteristics of the transistors, an Agilent 33250A signal generator was used to generate the gate voltage control pulse (-0.25 V low voltage, 1V high voltage, 50% duty cycle, 0.1 Hz frequency, for measurement in Fig. 3-8B), while the drain current was measured using the Keithley 2611B sourcemeter. Transmission spectra were measured using a spectrophotometer (X-Rite Color i5 Benchtop Spectrophotometer, X-Rite Inc., Grand Rapids, MI, USA) using a Keithley 2611B as the control voltage power source.

Part II

Generating Shape by Programmed Self-Folding

Chapter 4

Polymer swelling induced residual stress

Material processing steps affect the final mechanical properties significantly, and frequently, the resultant residual stress is an important consideration. The role of residual stress in thin-film fabrication has been well studied and modeled, for instance in microfabrication processes^{59,60}. Residual stress is broadly a result of gradients in the processing environment, often in the temperature and precursors, and standard techniques have been developed to measure this⁶¹. Effects of residual stress are rife in 3D-printing processes - gradients are easy to occur in techniques that utilize a repeated layering approach. Non-uniform residual stresses result in warping in most 3D-printing techniques including Fused Deposition Modeling (FDM)⁶², Selective Laser Sintering (SLS) & Selective Laser Melting (SLM)⁶³ and temperature/environment control systems are an important part of industrial printers.

Residual stress in parts printed from UV-curable resins and inks have a fundamentally different source. In processes like drop-on-demand 3D-printing, all layers receive different UV doses at the end of the print - the first deposited layers are exposed to

Contents of this chapter are adapted with permission from - S. Sundaram, D. S. Kim, M. A. Baldo, R. C. Hayward, W. Matusik, "3D-printed self-folding electronics", *ACS Appl. Mater. Interfaces*, 9 (37), 32290-32298 (2017). <https://pubs.acs.org/doi/abs/10.1021/acsami.7b10443> [Copyright American Chemical Society]

many passes of the UV source, while the last layers are exposed to much less UV doses. An optimized process should aim to produce parts with an uniform degree of crosslink through the entire part - and preferably full-crosslinked layers uniformly through the depth. However, this is complicated by two factors: (i) crosslinking results in shrinkage, and (ii) there is a delay between the formation of crosslinks and reaching the shrunk state⁶⁴. Therefore, avoiding residual stress completely in drop-on-demand 3D-printing is challenging. Residual stress results in the typical degradation of mechanical properties of polymers⁶⁵. Furthermore, the shrinkage of UV cured parts causes a departure from the expected dimensions of a printed part. In this chapter, we show that shrinkage can be avoided by controlling the degree of crosslinks during the printing process. Additionally, we demonstrate that residual stress can be tuned by the amount of polymer swelling.

4.1 Printing materials with residual stress

We observed that one of our elastic material formulations seemed to expand significantly on peeling after printing, in contrast to parts that tend to shrink when UV cured. Much of the following experiments and characterization were motivated by this initial observation. We henceforth refer to this material as the residual stress material (STR). STR is prepared by mixing 53.1 wt% CN3105 (Sartomer USA, Low viscosity acrylic oligomer), 18.8 wt% SR440 (Sartomer USA, isooctyl acrylate), 17.7 wt% SR504 (Sartomer USA, ethoxylated nonyl-phenol acrylate), 8.85 wt% Genomer 4215 (Rahn USA Corp., aliphatic urethane acrylate), 1 wt% Irgacure 819 (BASF Germany, bis(2,4,6-trimethylbenzoyl)- phenylphosphineoxide), 0.5 wt% ITX (Rahn USA Corp., 2-isopropylthioxanthone), 0.05 wt% MEHQ(Sigma-Aldrich USA, methoxyphenol). The different components are homogenized and left to mix overnight using a magnetic stirrer. Finally the ink is filtered using a 1 μ m filter and degassed using a vacuum pump to remove small bubbles. When a few layers (~ 50) of this material are printed and removed from the printer platform, its expansion is easy to observe.

To check if the ability to expand on crosslinking is an inherent property of the

material, it was also cured in a single step using a high intensity (14 W cm^{-2} at 365 nm, UV Fusion) broadband UV source outside the printer. Upon release from the mold, the cured piece does not expand, but instead shrinks slightly as a result of the formation of crosslinks, in contrast with the printed samples. We conclude that the residual stress enabled expansion is not merely a property of the ink alone but also the layer-by-layer deposition scheme as a part of the 3D-printing process. To better understand this, we performed an array of characterization measurements which are now described.

We started by testing whether the printed samples swell in the starting ink. To quantify the swelling tendency of the crosslinked polymer in the ink components, samples (cured fully in a single step) are allowed to swell by immersion in each of the individual ink components. The plot in Fig. 4-1 shows the swelling behavior of an externally cured sample of the polymer used to create residual stress. To characterize the inherent swelling of the material, and to remove any effect of the printing process, a 1 mm thick slab of the polymer was obtained by a single step curing process using a broadband UV source (with intensity $\sim 14 \text{ W/cm}^2$ at 365 nm). $0.8'' \times 0.15''$ samples were immersed in each component, where the plots show the swelling along the length of the samples after 1 hour, 3 hours and 1 day. The swelling results show that SR440 (isooctyl acrylate) plays a dominant role (causing $\sim 10\%$ expansion in each dimension of a 1 mm thick slab, after 1 hour), while all other individual components lead to negligible swelling over the same time.

This can be attributed in part due to the nature of the side chains of the acrylate components. SR440, SR504 and SR313B include an isooctyl group (C_8H_{17} chain), ethoxylated nonyl phenol group ($\text{C}_{23}\text{H}_{39}\text{O}_4$ group which includes a phenol group) and a dodecyl group ($\text{C}_{12}\text{H}_{25}$ chain; methacrylate) respectively. It is expected that SR440 diffuses the most due to its low molecular weight and shortest side chain, though multiple other factors may be relevant. SR 313B does not enhance the swelling and was observed to further limit expansion when used as a part of the crosslinked polymer. SR313B is therefore not used in the formulation of the stress layer (STR) ink.

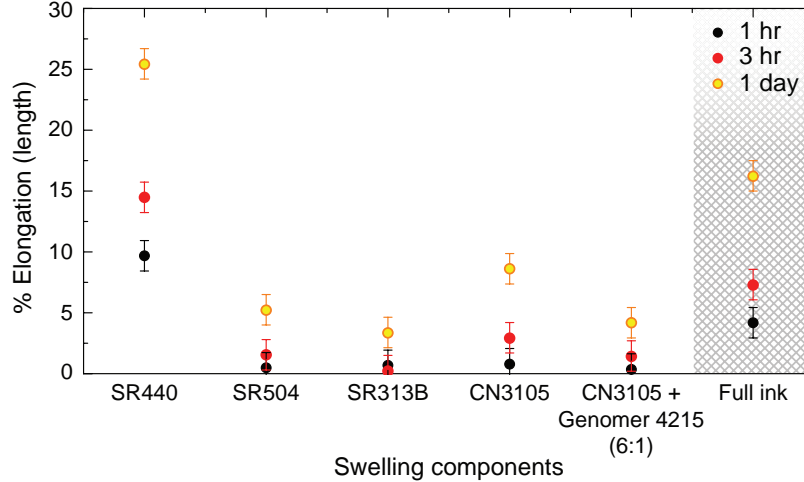


Figure 4-1: **Swelling of UV cured polymer samples in different components** Genomer 4215, an aliphatic polyester urethane acrylate is mixed with CN3105 (1:6 by weight, as used in the final ink) due to its high viscosity. It is evident that SR440, the isooctyl acrylate plays a dominant role in the swelling even after 1 hour. Each layer in the 3D-printing process is $\sim 17 \mu\text{m}$. Assuming a purely diffusive process, (diffusion time, $t \approx x^2/2D$), swelling of a 1 mm thick sample after 1 hour corresponds to the amount of swelling of each printed layer after $\sim 1.04 \text{ s}$.

It is important to note that during the actual printing process, the uppermost printed layers are exposed to one pass of the 0.9 W cm^{-2} UV source before exposure to fresh ink. Therefore diffusion is expected to be further enhanced in the printing process compared to the single-step fully-crosslinked samples. After small molecules diffuse into the underlying layers, they are crosslinked into the existing network with subsequent UV curing passes.

4.2 Role of crosslink density

To measure the actual degree of crosslinking in samples printed in our printer, we used Fourier Transform Infrared (FTIR) attenuated total reflection (ATR) spectra for a range of samples, cured with various intensities and number of curing passes in the printer. Figure 4-2 shows the FTIR ATR spectra measured on sample surfaces after 1 curing pass of the UV light (0.3 W cm^{-2} and 0.9 W cm^{-2}) along with the starting ink and fully crosslinked samples for comparison. FTIR spectra were obtained using

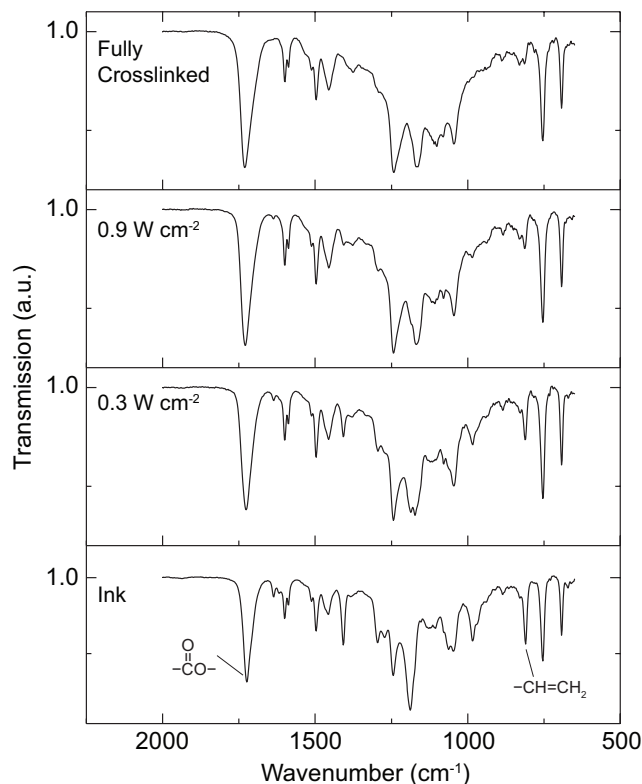


Figure 4-2: **Sample FTIR spectra of STR with varying crosslink density.** Panel of plots show representative FTIR ATR spectra measured on the surface of samples that are fully crosslinked, and samples cured by 1 pass of the UV light (0.3 W cm^{-2} and 0.9 W cm^{-2}) along with the starting ink. The vinyl and carbonyl group peaks are seen at $\sim 1705 \text{ cm}^{-1}$ and $\sim 809 \text{ cm}^{-1}$ respectively.

the Thermo Fischer FTIR 6700 Fourier Transform Infrared Spectrometer setup in the ATR mode with a Silicon crystal. Spectra were measured on three samples on the surface for each data point. The reactive double conversion is measured by normalizing the absorption peak of the “ $-\text{CH}=\text{CH}_2$ ” group with respect to the “ $-\text{COO}-$ ” group⁶⁶. The ratio between the absorbance of the vinyl group (809 cm^{-1}) with respect to the carbonyl group (1705 cm^{-1}) is used to measure the monomer conversion percentage. Reaction conversion is obtained by using the starting ink ($A_{\text{vinyl}}/A_{\text{carbonyl}})_{\text{ink}}$ as the 0 % conversion reference and the samples with 4 curing passes with the UV fusion ($A_{\text{vinyl}}/A_{\text{carbonyl}})_{\text{UVfusion}}$ as the fully-crosslinked reference.

The effect of the UV intensity and number of UV curing passes is seen more clearly in the plot in Fig. 4-3A. It is observed the double bond conversion of the lightly crosslinked layer (one pass with the default 0.9 W cm^{-2} intensity source) is \sim

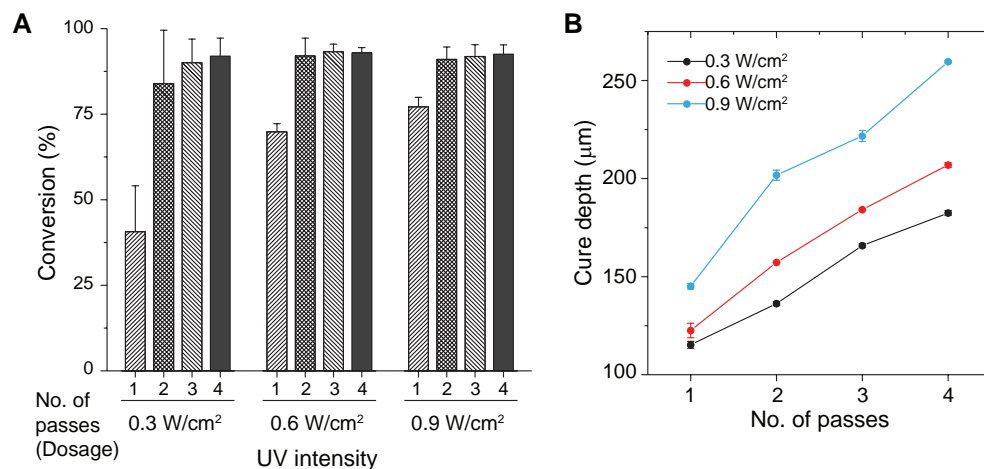


Figure 4-3: **Double bond conversion and cure depth.** **A.** The double-bond conversion percentage is calculated as a function of the UV light intensity and the number of curing passes from the Fourier transform infrared (FTIR) attenuated total reflection (ATR) measurements on the surface of the samples (three samples for each data point). **B.** Plot of the cure depth measured as a function UV light intensity and the number of passes.

77 %; samples reach near full double bond conversion after 3 passes (from 3 samples for each data point). In all these tests with multiple curing passes, new ink was not added to understand the effect of the UV curing passes alone, in contrast to the printing process where ink is added. Figure 4-3B shows the measured cure depth at these intensities and number of passes. This is the thickness of the crosslinked solid layer, or the effective penetration depth of UV light in terms of crosslinking the ink. Typical cure depth after 1 pass of the UV light at 0.9 W cm^{-2} intensity is $\sim 150 \mu\text{m}$.

As described earlier, during the printing process there is a gradient in received UV dosage going from the uppermost printed surface (latest) to the first printed layers. To perform a controlled study of the equivalent initial strain in the samples without dosage gradients along the thickness, we performed the subsequent measurements of gel fraction and linear strain using single step cured samples of a controlled thickness. For the thickness of layers to be meaningful, i.e., without significant gradients in the crosslink density along the depth, we try to constrain this value below the cure depth at each UV intensity. To understand the strain in the printed layers, we UV cured multiple samples with one pass of the UV light with different intensities (controlling

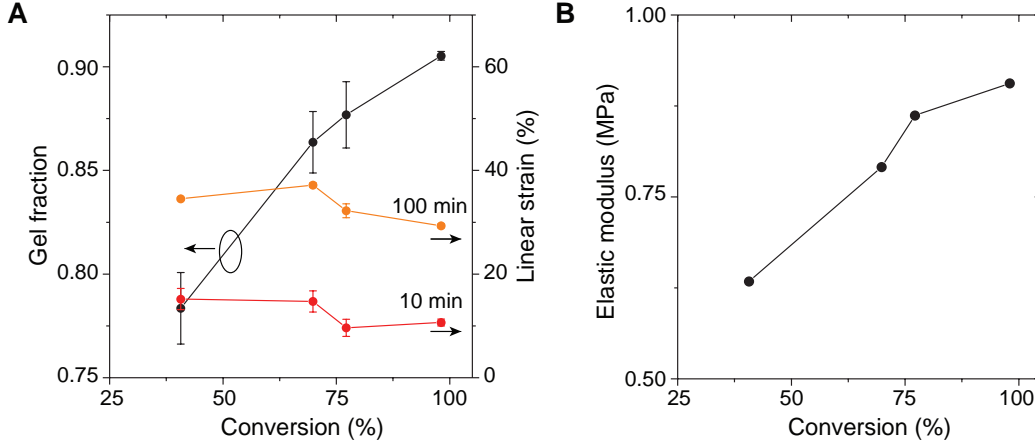


Figure 4-4: **Linear strain due to swelling and mechanical properties.** **A.** Measured linear expansion in one dimension as a function of double-bond conversion for different swelling times (samples are $\sim 125 \mu\text{m}$ thick). The samples are prepared using single curing passes with varying UV light-emitting diode (LED) intensities. As printed, the samples shrink by $< 1 \%$ typically. These samples with one-shot curing are expected to show isotropic swelling. The plot also shows the measured gel fraction of samples as printed. **B.** Elastic modulus values are measured for the samples after one UV curing pass at various light intensities (0.3 , 0.6 , and 0.9 W cm^{-2} using the printer and $\sim 14 \text{ W cm}^{-2}$ using a high-intensity broadband source, UV fusion).

the double bond conversion). The measured increase in one dimension (averaged from 4 individual samples) is plotted as a function of double bond conversion in Fig. 4-4A. In these experiments the cured samples were soaked in the starting ink of the residual stress material for different amounts of time to control the swelling. It is observed that the resulting strain increases with swelling time. It is to be noted that these experiments were performed with a spacer of thickness $\sim 125 \mu\text{m}$ for handling despite this being close to the cure depth at lower UV intensities; samples with 0.3 W cm^{-2} curing were very fragile and easy to tear. It is noteworthy that diffusion time is proportional to the thickness squared; 10 min swelling experiment conducted on a $125 \mu\text{m}$ sample corresponds to $\sim 10 \text{ s}$ of swelling a $17 \mu\text{m}$ layer. Additionally, the experiments are conducted at room temperature, however, in the actual printing process the droplets leaving the printhead leave at an elevated temperature and would experience increased diffusion. The measured increase in the length can be translated to an isotropic increase in all the three dimensions for single-pass cured samples swelling in the starting ink. During the printing process the scenario is different with

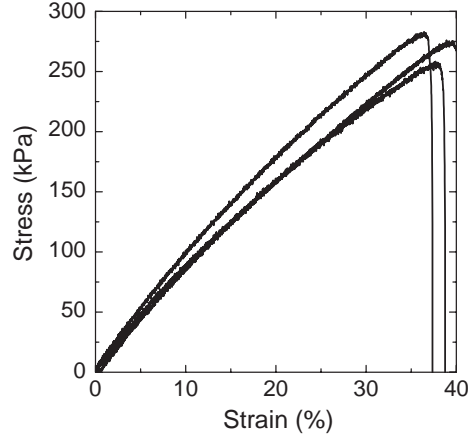


Figure 4-5: **Mechanical strain tests of printed STR.** Measured stress plotted as a function of strain for three printed stress layer samples each ~ 7.2 mm wide, measured at a strain rate of ~ 10 % per minute for each sample. The linear elastic modulus of the averaged stress-strain curve is 1.076 MPa at 0.5 % strain

isotropic stresses only in the in-plane directions but not out-of-plane. The figure also shows the gel fraction of as-printed samples for various double bond conversion levels. Figure 4-4B shows the elastic modulus of samples at different levels of double bond conversion. The modulus improves with the degree of double bond conversion as expected. The stress-strain relationship for multiple printed samples with multiple layers is shown in Fig. 4-5. The typical elastic modulus of printed multilayer STR samples linearized at 0.5 % strain is 1.08 MPa.

More broadly, the mechanical properties of STR depend on the glass transition temperature T_g and its relative position with respect to room temperature. Figure 4-6A and B, show the differential scanning calorimetry (DSC) measurements for RIG (for comparison) with STR. The material with the residual stress is well into the rubbery state at room temperature. This is also seen in the dynamic mechanical analysis (DMA) data shown in Fig. 4-6C & D. STR has a high loss modulus at room temperature, and the $\tan \delta$ peak is below room temperature in this case. In comparison, RIG at room temperature is below its glass transition temperature state and is therefore in its rigid glassy state. These measurements to an extent also indicate the expected polymer chain relaxation and compliance measurements which are discussed in more detail in the next chapter.

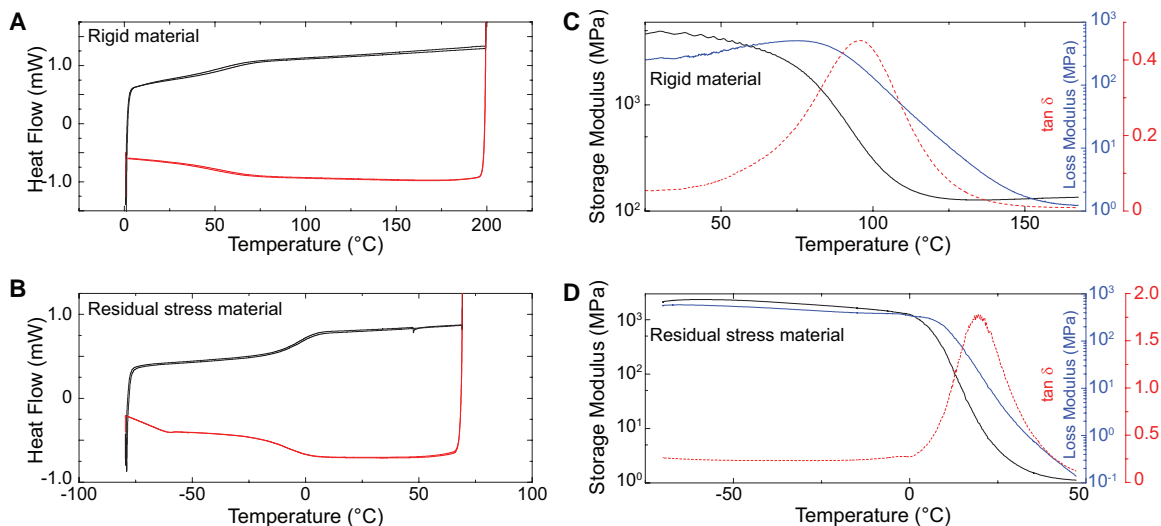


Figure 4-6: **Differential scanning calorimetry (DSC) and dynamic mechanical analysis (DMA) data.** **A** and **B** show the DSC data for the rigid material (RIG) and the stress material (STR) respectively. It is seen that RIG shows a broader glass transition centered at around 50 °C while STR shows a sharper glass transition below 0 °C and reaches a fully rubbery state at room temperature. **C** and **D** show the DMA measurements of the storage modulus, loss modulus and $\tan \delta$ measurements at 1 Hz cycling frequency for RIG and STR respectively

This chapter demonstrated that residual stress can be induced by polymer swelling. Small molecules part of the ink can diffuse into lightly-crosslinked layers to not only avoid shrinkage but even cause expansion in the 3D-printed samples. While residual stress is usually considered a problem, these ideas can be used to effectively counter the conventional shrinkage issue resulting from the formation of crosslinks. It is evident that the process parameters like UV intensity and number of passes help in tuning the degree of crosslinking which controls the amount of polymer swelling. In the next chapter, we describe how the generated residual stress can be use favorably to create self-folding composites that require no controlled stimulus, and how this enables 3D electronic composites.

Chapter 5

Self-folding electronic composites

5.1 Shape transformation in electronics

Programmable shape transformation strategies offer a wide range of advantages in the context of device fabrication. Not only do they help speed up the fabrication process, these techniques also provide access to complex geometries that are hard to fabricate directly. Recently, programmable matter and self-assembled structures have highlighted a range of applications that unify physical shape and overall function^{10,67}. For instance, advances in robotics⁶⁸, photovoltaics⁶⁹, antennas⁷⁰, biomimetic imagers⁷¹, and inertial measurement units⁷² present a compelling set of devices where electronics have now evolved to non-traditional complex architectures. Adapting contemporary planar electronics, which have high performance, to three-dimensional geometries, however, has been a challenging task. This is currently being tackled using a variety of techniques such as: droplet wetting to induce self-folding⁶⁹, manual folding of silicon pieces with interlocks⁷² and compressive buckling of thin silicon membranes bonded on pre-stretched materials⁷³. The general approach thus far is to create the

Contents of this chapter are adapted with permission from - S. Sundaram, D. S. Kim, M. A. Baldo, R. C. Hayward, W. Matusik, "3D-printed self-folding electronics", *ACS Appl. Mater. Interfaces*, 9 (37), 32290-32298 (2017). <https://pubs.acs.org/doi/abs/10.1021/acsami.7b10443> [Copyright American Chemical Society]

electrical device on planar silicon using microfabrication techniques, and subsequently shape it using different methods. These shaping techniques have the advantage of being directly applicable to planar-fabricated silicon-based electronics. However, they tend to be device specific, constrained in possible geometries, or not easily scalable. A process that creates electrical function within a complex 3D structure seamlessly is of significant practical importance, and is therefore an active area of research.

Outside the confines of traditional electronic device fabrication, a broad set of origami and kirigami-inspired techniques have been extensively explored as potential routes to fabricating complex 3D structures thus far^{67,68,74-80}. Demonstrations of material folding have spanned several orders of magnitude in length scales, utilizing a disparate set of mechanisms⁷⁴ including: controlled buckling⁷³, shape memory effect in composites^{75,76}, pneumatically driven transformations⁷⁷, thermally controlled swelling in hydrogels⁷⁸, photo-induced folding and manipulation⁷⁹⁻⁸³, residual stress induced curling⁸⁴, and controlled formation of creases⁸⁵. More recently, additive manufacturing has been used to create 3D structures using shape transformation techniques.

5.2 4D-printing

3D-printing techniques have been used to create 3D structures that evolve over time with controlled stimuli. These techniques - broadly referred to as 4D-printing⁸⁶⁻⁸⁸, with time being the 4th dimension - typically use temperature-controlled shape memory polymers, or hydrogels that swell in a solvent. Folding flat, printed composites into complex structures has additional benefits over directly printing the final 3D-structure, typically in the overall fabrication speed, cost, and ease of scaling. Furthermore, when solvent based inks are used (as is typical for a majority of electrically important materials) folded geometries may not be directly 3D-printed due to challenges from droplet spreading and non-uniform film thicknesses. This has generated considerable recent interest in 4D-printing - enabling structures that change dynamically thus allowing the shape to be controlled over time⁸⁹⁻⁹⁴. While there have been

attempts to embed packaged electronics inside 3D-printed structures^{95,96} to improve their overall functionality,⁹⁷ achieving fully 3D-printed electronics that self-fold is a current challenge. A first step in this direction is shown in a recent report where conductors are inkjet-printed on top of flattened 3D-printed shapes that can be restored to their original shapes using the shape memory effect⁹⁸. Similarly, electrically conductive shape memory materials have also been 3D-printed via direct ink writing⁹⁹. Despite the tremendous interest in shape transformation in 3D-printed structures, there are several practical challenges that exist in expanding these structures to include printed electronic devices. The two common classes of mechanisms used for self-folding in 3D-printed structures are based on the temperature controlled shape-memory effect in polymers and the controllable swelling of hydrogels in water and other liquids⁶⁶. The main focus of these approaches is the ability to achieve reversible self-folding, which is a significant advantage. The required stimuli, i.e., temperature cycling and immersion in liquids, however, may not be desirable for use with electronic devices. This is particularly relevant if the electrically active materials of the self-shaping composite may degrade with temperature cycling or exposure to humidity. Controllable folding with the ability to engineer stress at multiple positions is more favorable for electronics applications that do not require reversible shape change. Recently, a temperature input (in a system of polymers with different coefficients of thermal expansion) was used to accelerate folding based on an inbuilt strain¹⁰⁰. This is an elegant method that can create rapid folds. However, the use of a commercial printer with proprietary inks (that by default uses a flattening roller) makes it challenging to identify the stress creation mechanism. Furthermore, electrically relevant materials cannot be printed with this system, which is a key consideration.

In this chapter, we present a new approach to fabricate composites that can self fold. Importantly, these composites can contain electrical materials and devices, and do not have to be subjected to heat, or dipped in a solvent to initiate folding. This is achieved by merging regions with residual stress (described in the previous chapter) with a rigid but flexible substrate to generate folds. The whole composites are 3D-printed together, and both concave and convex folds can be obtained by controlling

the location of the regions with residual stress. The overall scheme is shown in Fig. 5-1. The crosslinked material with the residual stress STR, swells significantly in the starting ink containing small molecules (with pronounced swelling in isooctyl acrylate). During the layer-by-layer printing process here, each underlying cured layer ($\sim 17 \mu\text{m}$ in thickness) is automatically exposed to new ink which diffuses into the partly crosslinked layer below before the UV light passes over it. This causes the material to have an inherent residual stress that forces it to expand when unconstrained (removed from the print platform) as described in the previous chapter. This is illustrated in the bottom right of the scheme in Fig. 5-1, where the ink before curing is shown in yellow and the lightly crosslinked upper layers are shown in green (the colors correspond to the same residual stress material before and after curing).

5.3 Self-folding bilayer

To study the effectiveness of using residual stress to create folds, we used a bilayer geometry - STR (with residual stress) on top a rigid but flexible layer of RIG. For these experiments we printed the geometry shown in the inset of Fig. 5-2A. The expansion in the stress layer exerts a surface load on the rigid polymer causing the structure to bend, with a uniform radius of curvature, r_d . To characterize the folding, multiple bilayer structures are 3D-printed and the folding angle is measured as a function of the thickness of the stress layer over time. The thickness of the rigid layer, t_r , is $99.9 \mu\text{m} \pm 4.3 \mu\text{m}$, the width, W , is 4 mm, and the stress layer thickness varies from $71.95 \mu\text{m}$ to $270.9 \mu\text{m}$. The printed samples are peeled from their flat state and kept at a controlled temperature ($25 \text{ }^\circ\text{C}$). The folding angle, θ_d , is measured as a function of time for multiple designs and shown in Fig. 5-2A with each point showing measurements from 3 samples. It is observed that the folding angle increases with the stress layer thickness (in this range) until 1000 min, and the angle continues to increase over time showing no saturation up to 3000 min. When no stress layer is added (as negative control samples), the rigid layers themselves do not show any noticeable folding over time. In order to design new structures, understanding this temporal behavior in the

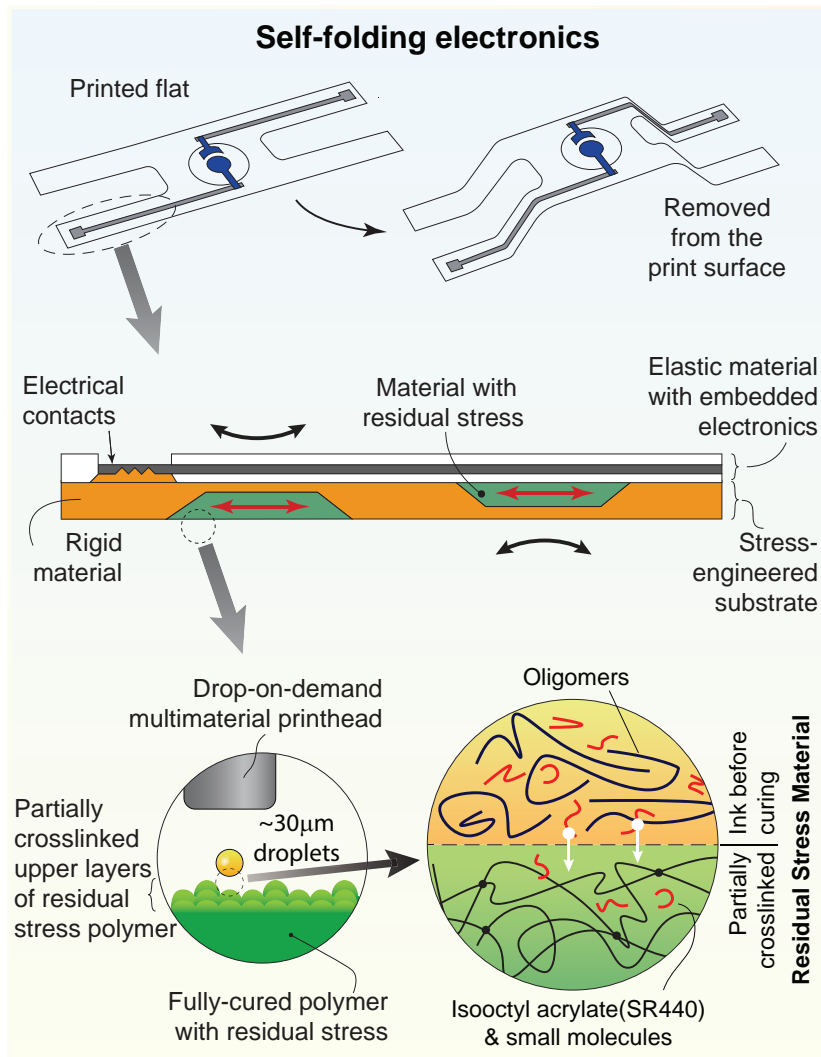


Figure 5-1: **Electronic composites that self-fold.** At the heart of this scheme is a UV curable ink containing acrylate oligomers, and short-chain monomers (such as isooctyl acrylate). As a part of the layer-by-layer inkjet based 3D-printing process, each previously cured (lightly-crosslinked) layer, $\sim 17 \mu\text{m}$ thick, is exposed to uncured ink from the subsequent layers. The small molecules from the ink swell the underlying cured layers and create local residual stress, as described in the previous chapter. The full composite containing active electronics, metallic traces and the substrate is 3D-printed. On removing the 3D-printed structure from the print platform, the composite spontaneously folds in a shape based on the locally engineered residual stress, requiring no stimulus at room temperature. Both the circular close-ups shown in the bottom only show the residual stress material, before and after curing; the rigid material is not linked to the stress generation mechanism. Concave and convex folds of desired angles can be created by controlling the material placement and the design geometry. In this scheme, the active electronics are electrically connected by a stretchable conductor printed within the same system.

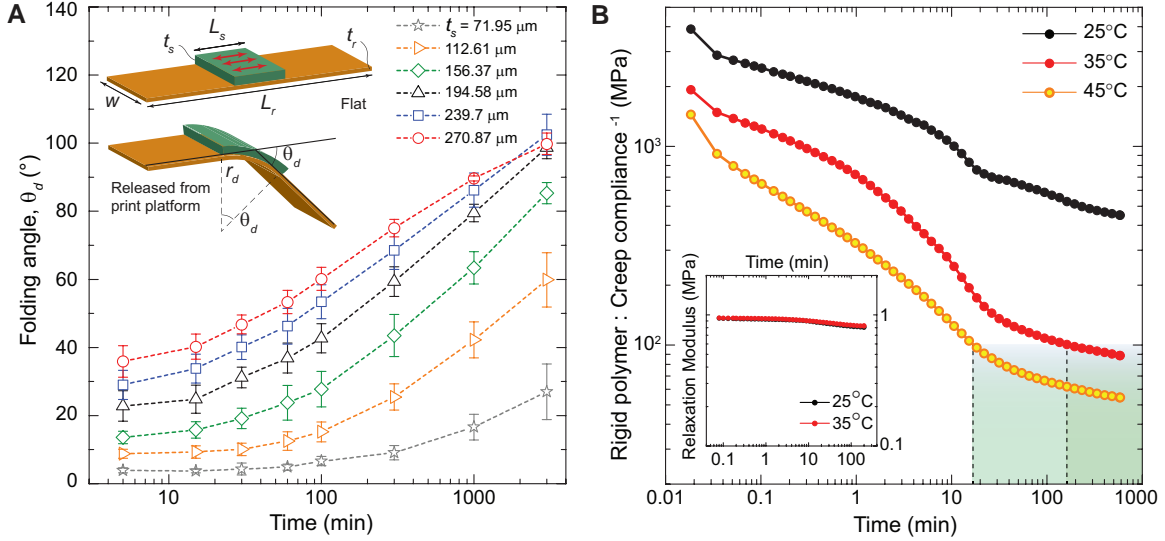


Figure 5-2: **Characteristics of the bilayer system used for creating folds.** **A.** Plot shows the measured folding angle with time after peeling the bilayer geometry from the printer platform. The inset show the bilayer device geometry and the corresponding variables. **B.** The plot shows the inverse of the creep compliance of the rigid material at 25 °C, 35 °C and 45 °C. The material shows a rapid increase in the compliance until ~ 30 min, after which the increase in creep compliance settles to a slower rate. The modulus drops by more than one order of magnitude between the start and 10 hours into the creep test. The inset shows the relaxation modulus of the stress layer material (STR). The relaxation modulus shows a negligible drop after 200 min (in the stress relaxation experiment). Further, there is no significant change in the base stiffness of the material as the temperature is increased to 35 °C since the material is well into the rubbery regime.

folding angle and its relationship with geometry is important.

From the DSC and DMA measurements of the two materials, RIG & STR described in the previous chapter, it is evident that the cured polymer RIG is below its glass transition temperature (~ 50 °C) while STR's glass transition temperature is -10 °C. Since the rigid layer is close to its broad glass transition regime, the dynamics are largely expected to be limited by the relaxation timescales of RIG. To understand the timescale of polymer chain relaxation in the rigid material, creep compliance measurements are performed using DMA, and the results are shown in Fig. 5-2B for 25 °C, 35 °C and 45 °C. The inverse creep compliance drops by approximately an order of magnitude by 600 min, and the rate of decrease rises as the temperature is brought closer to 50 °C. It is also observed that drop in the inverse creep compliance slows

down beyond $\sim 20 - 30$ mins after application of the load. Meanwhile, it is observed that the relaxation modulus of STR shown in the inset, is ~ 0.9 MPa and shows little change with time and temperature, confirming that the STR is in a completely rubbery state. To confirm that the change in the folding angle with time is a result of the increasing rigid material (substrate) compliance, we repeat the measurements of the folding angle for multiple designs at elevated temperatures (35°C and 45°C). At these slightly elevated temperatures, the sharper drop in the inverse creep compliance results in larger folds and saturation of the folding angle after 100 min and ~ 10 min at 35°C and 45°C , respectively, for the same set of designs (Fig. 5-3A). It can be seen that the effective modulus of the rigid material falls below ~ 100 MPa at these time intervals from Fig. 5-2B. This apparent threshold for saturation of folding can be understood from a first order bilayer model.

5.4 Modeling the self-folding system

A simple model of the bending system described here consists of a stack of two linear elastic materials. As described earlier, we can model this system, as a thin, rigid material of thickness, t_r , and a layer of material with residual stress (STR) of thickness, t_s . The corresponding elastic moduli (E , in general) are E_r and E_s . The planar moduli for the two materials can be written as $\tilde{E}_r = E_r/(1 - \nu_r^2)$ and $\tilde{E}_s = E_s/(1 - \nu_s^2)$. For the two materials in this work, $\tilde{E}_r \gg \tilde{E}_s$, typically by 2 - 3 orders of magnitude. In this case, the bottom rigid layer can be assumed to undergo negligible amount of stretching. In a general case, the initial energy stored in the upper residual stress layer can be used as the input energy to deform (bend) the bilayer stack. There are two limiting cases of interest here: (i) the thickness of the stress layer (top layer) is small ($t_s < t_r$), such that a majority of the residual energy stored in this film is used in bending the rigid layer underneath, (ii) thickness of the stress layer exceeds that of the rigid layer ($t_s > t_r$, $\tilde{E}_r \gg \tilde{E}_s$). In the latter case, the underlying rigid film can be treated as an inextensible layer that undergoes pure bending (constant length). The neutral axis of the bilayer stack is approximately at

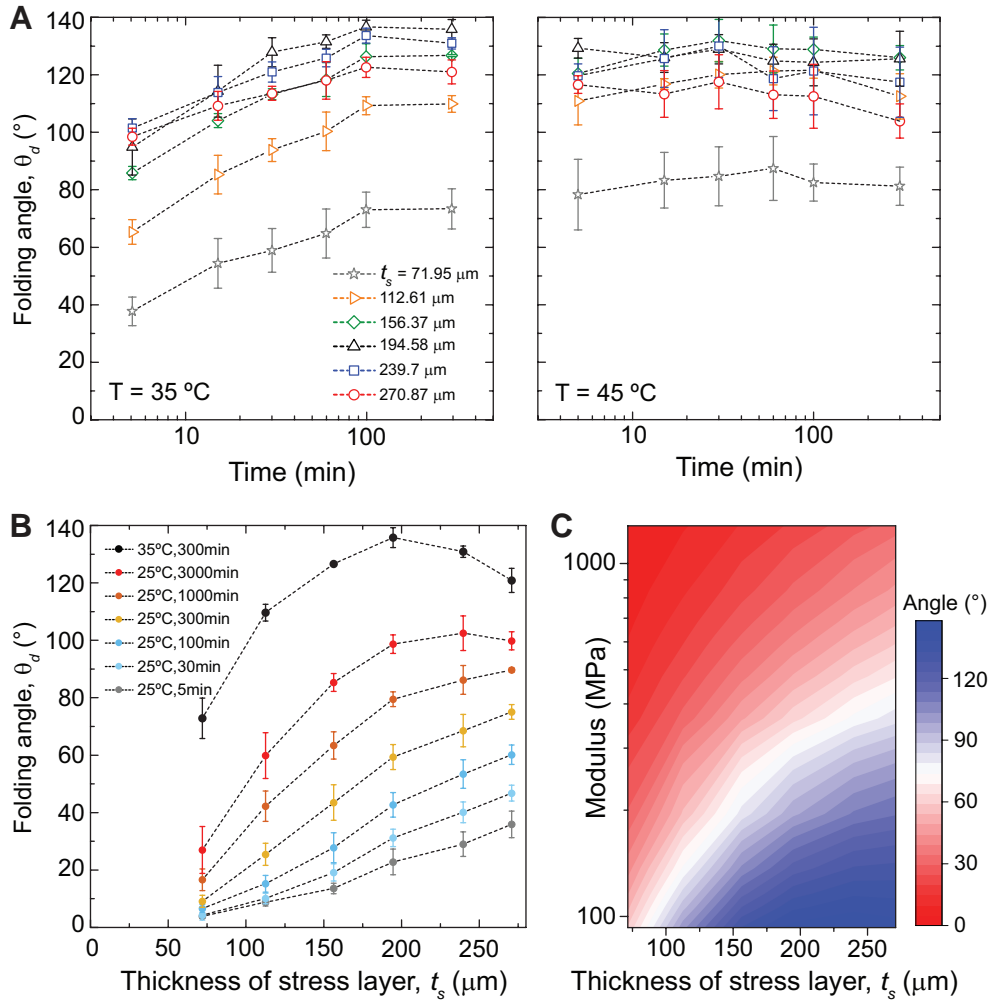


Figure 5-3: **Bilayer characteristics at elevated temperatures and design guidelines** **A.** Plots show the time dependence of the folding angle of the bilayer system used for creating folds at 35 $^{\circ}\text{C}$ and 45 $^{\circ}\text{C}$. The folding angle shows little variation past 100 min at 35 $^{\circ}\text{C}$. Samples approach a steady state folding angle after ~ 5 min at 45 $^{\circ}\text{C}$. **B.** The folding angle is shown as a function of the stress layer thickness at various time instants at 25 $^{\circ}\text{C}$. The black curve shows the saturated folding angle at 35 $^{\circ}\text{C}$ (after 300 min). Note that the optimum thickness of the stress layer for creating larger folds changes with time (due to a larger creep compliance). **C.** Finite element analysis (FEA) predictions of the folding angle based on geometry and time (or equivalently elastic modulus).

the center of the rigid material when $t_r \cdot \tilde{E}_r / \tilde{E}_s \gg t_s$. Under this condition, the energy required to bend the rigid material of unit width and length is obtained as

$$U_r = \frac{\tilde{E}_r t_r^3}{24r_d^2} \quad (5.1)$$

where r_d is the radius of curvature. In this configuration the energy component required to deform the residual stress layer (of unit width and length) to the same curvature is

$$U_s = \frac{\tilde{E}_s t_s^3}{24r_d^2} \left[3 \left(\frac{t_r}{t_s} \right)^2 + 6 \left(\frac{t_r}{t_s} \right) + 4 \right]. \quad (5.2)$$

In the folding angle experiments described in Fig. 5-2A & 5-3, the thickness of the stress layer is increased from 71.95 μm to 270.9 μm . In the upper limit of the stress layer thickness, the conditions $t_s > t_r$ and $t_r \cdot \tilde{E}_r / \tilde{E}_s \gg t_s$ are valid. To compute an estimate for threshold modulus of the rigid material, \tilde{E}_r , below which further softening of the rigid material does not affect folding angle drastically, the energy required to deform the residual stress layer should be the dominant part, i.e., $U_s > U_r$. This results in the condition

$$\frac{\tilde{E}_r}{\tilde{E}_s} < \left(\frac{t_s}{t_r} \right)^3 \left[3 \left(\frac{t_r}{t_s} \right)^2 + 6 \left(\frac{t_r}{t_s} \right) + 4 \right] \quad (5.3)$$

and can be approximated to

$$\frac{\tilde{E}_r}{\tilde{E}_s} < 4 \left(\frac{t_s}{t_r} \right)^3 \quad (5.4)$$

when $t_s > t_r$. For the case when $t_s = 270.9 \mu\text{m}$ and $t_r = 99.9 \mu\text{m}$ this threshold ratio is obtained as 79.7. Using the parameters $E_s = 0.9 \text{ MPa}$, $\nu_s = 0.44$, the threshold planar modulus for the rigid material, \tilde{E}_r , is obtained to be 88.7 MPa.

Intuitively, as the equivalent elastic modulus of the rigid material (substrate) starts to drop over time, an increasing portion of the residual energy stored in the stress layer (expanding material) is used in deforming (bending) itself. Beyond this threshold modulus of the rigid material, the energy spent in bending the rigid substrate is negligible, and further reduction in its elastic modulus does not result in an increase

in the folding angle. It is also evident that at elevated temperatures, increasing the thickness of the stress layer does not necessarily lead to increasing folding angles (experimental results in Fig. 5-3A and 5-3B).

Given the geometry of a bilayer stack and its material properties, bending resulting from a stress or swelling can be modelled analytically for simple planar geometries. So far the bending of bilayer stacks containing linear elastic materials, have been calculated using Timoshenko's bilayer model or the generalized Stoney's equations^{78,101} and the folding angle is obtained as

$$\theta_d = \frac{6\varepsilon\xi\eta(1+\eta)}{1+4\eta\xi+6\eta^2\xi+4\eta^3\xi+\eta^4\xi^2} \frac{L_s}{t_r} \quad (5.5)$$

where ε is the prescribed strain, $\eta = t_s/t_r$, the ratios of the thickness and $\xi = \tilde{E}_s/\tilde{E}_r$, the ratio of the planar moduli of the two materials. It is important to note that this model is not accurate for very tight curvatures when strains are not small, nonetheless it provides a good approximate estimate of the folding angle. More accurate results, if desired, can be obtained from finite element method (FEM) simulations. Figure 5-3C show FEM predictions of the folding angle as a function of elastic modulus of the rigid substrate and the thickness of STR. Note that in our system the time varying angular deflection results from the variation in the effective elastic modulus of the rigid substrate as a function of time. But this model requires an equivalent prescribed strain in the STR layer, resulting from the residual stress. The prescribed strain is estimated to be $\varepsilon = 0.22 \pm 0.027$; details are below.

To calculate the equivalent prescribed strain, finite element analysis is performed using COMSOL Multiphysics with the planar strain approximation. The input material properties are measured from experiments. The density of printed samples of the rigid material and the residual stress material are measured to be 1.1 g/cm^3 and 1.165 g/cm^3 respectively. A linear Poisson's ratio estimate was obtained from images of marked samples deformed under an applied load (using the Instron 5944, a single column mechanical testing system) and were found to be $\nu_s = 0.44 \pm 0.006$ and $\nu_r = 0.28 \pm 0.08$. The elastic modulus of the residual stress material was kept

constant in all simulations at $E_s = 0.9$ MPa. To obtain the curves in Fig. 5-4A, the above parameters were used along with values of the effective modulus, E_r , at each time instant. The values of the effective modulus (inverse creep compliance at 25 °C) of the rigid material (from Fig. 5-2B) after 5 min, 15 min, 30 min, 60 min, 100 min, 300 min are 1278.8 MPa, 838.8 MPa, 684.2 MPa, 625.9 MPa, 577.4 MPa and 478.8 MPa respectively. The geometric parameters used in the simulations are the following: thickness of the rigid layer, $t_r = 99.91$ μm , length of the stress layer, $L_s = 4$ mm, and length of the rigid layer, $L_r = 15$ mm and the width, $W = 3.25$ mm. The prescribed strain (initial strain, isotropic) used in the simulation for each curve is reported in the legend of Fig. 5-4A. The same procedure was repeated for the folding angle measurements at 35 °C in Fig. 5-4B (using the corresponding values from Fig. 5-2B). The average prescribed strains used in all simulations is obtained to be 0.22 ± 0.027 . This single parameter can be used to model the residual force in the system. It can be seen that at 35 °C, increasing the thickness of the stress layer does not always lead to increasing folding angles. The average strain in the residual stress material ($\sim t_s/2r_d$) in the folded state is directly proportional to the thickness of the residual stress material. Therefore, at the limit when negligible energy is spend on bending the rigid material, increasing t_s has to be accompanied by increasing r_d (or reducing angle) for maintaining a constant average strain in the material.

The folding angle is plotted as a function of thickness of the stress layer, t_s , and the elastic modulus of the rigid material E_r in the contour maps in Fig. 5-5A, 5-5B and 5-5C (the experimentally measured angles, results of finite element analysis and Timoshenko's equation respectively). It can be seen that Timoshenko's model (eq. 5.5) underestimates the angle compared to the finite element simulations. Overall, the finite element simulations model the folding process reasonably well using an initial prescribed strain of 0.22 in the material, and using the inverse of the time varying creep compliance as the effective modulus (of the rigid substrate material). However, it has to be noted that this derived value is expected to be a function of the crosslink density (controlled by the UV curing technique used in the printing process).

To investigate the effects of high UV dosage and heating on the residual stress

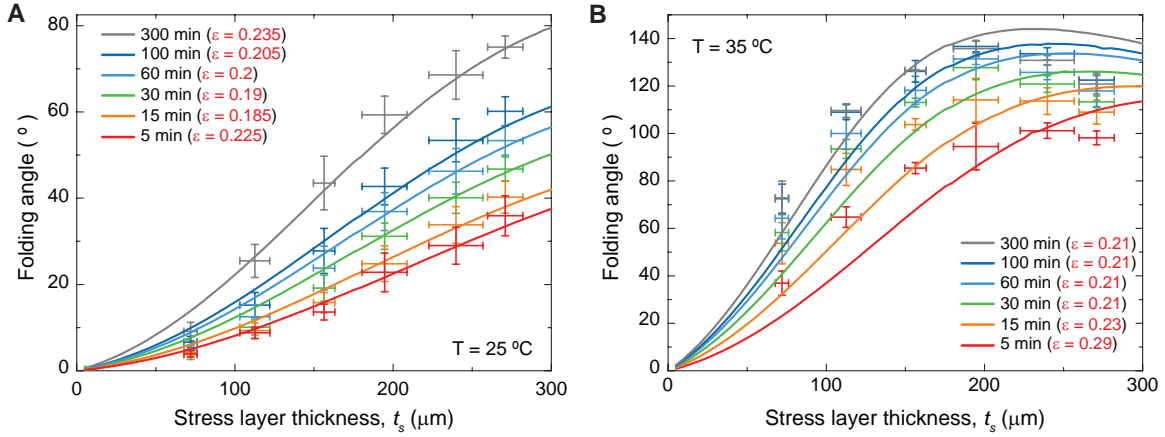


Figure 5-4: **Modeling the folding in the bilayer geometry - extracting prescribed strain A.** Plot shows the measured folding angle as a function of the stress layer thickness when the samples are placed in a temperature controlled oven at $25\text{ }^{\circ}\text{C}$ (data from Fig. 5-2A) for the initial 300 min. The inverse creep compliance plot from Fig. 5-2B is used as the effective instantaneous elastic modulus for the rigid substrate in a finite element simulation in COMSOL using the 2D planar strain approximation. The other material properties are assumed constant with respect to time. The values of the Poisson's ratio for the two materials are measured to be 0.28 (rigid material - RIG) and 0.44 (residual stress material - STR). The density of the printed samples are 1.1 g/cm^3 and 1.17 g/cm^3 respectively. Along with the above material properties, the elastic modulus of the stress material is assumed to be constant at 900 kPa. This assumption is reasonable given that the relaxation modulus for the stress layer (inset of Fig. 5-2B) does not change over time. The solid curves in the figure show the folding angles from the simulation. The corresponding initial strain used in the simulation (ϵ) is shown for each curve in the legend. **B.** The same is repeated for the measured values at $35\text{ }^{\circ}\text{C}$. It can be seen that in both 'A' and 'B', the assumption of a time varying elastic modulus of the rigid material proves to be a good approximation. The average strain used in all finite element simulations is 0.22 ± 0.027 .

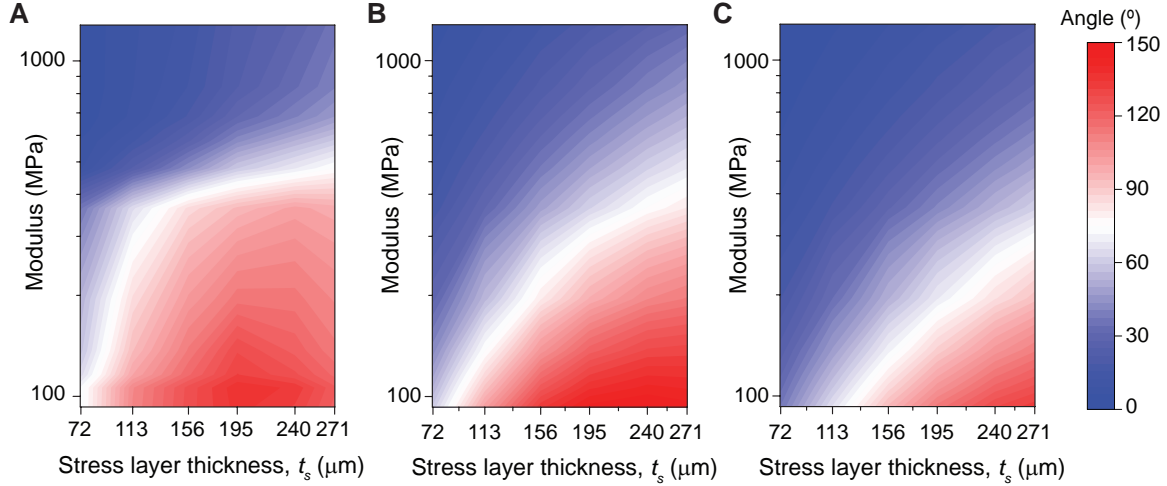


Figure 5-5: **Folding angle measurements and comparison with simulation A.** Contour map of the measured folding angle as a function of rigid substrate modulus and the stress layer thickness. **B.** The contour map shows the corresponding values from the finite element simulation using an initial strain of 0.22. **C.** The results of Timoshenko beam theory for the same value of the input strain (ε) using the planar modulus for the materials, $E/(1 - \nu^2)$, as input parameters (E is the elastic modulus, and ν is the Poisson's ratio).

(and the corresponding folding angles), an array of samples were 3D-printed on glass slides and processed differently. The thickness of the rigid material, t_r , is 80.1 μm , the width, W , is 3.25 mm and the length of the stress layer, L_s , is 4 mm. A set of samples were left as printed. An equal number of samples were exposed to UV light (5 mW/cm^2 at 365 nm) for an hour. Similarly, separate samples were also placed into the convection oven at 100 $^\circ\text{C}$. All the three sets of samples were removed from the glass slides and the folding angles were measured after same time interval (15 min). The corresponding measurements of the folding angle are shown in Fig. 5-6A. Figure 5-6B shows optical images of the set of prints that were peeled with neither excess UV dose nor excess heating. From Fig. 5-6A, it can be seen that the prescribed strain used to model the system reduced from the original value, 0.22, to ~ 0.1 . This preliminary result shows that both temperature variations and the UV curing process affect the folding angle. However, measurements of the folding angle of samples made in the final optimized process can be used to obtain the equivalent initial strain, ε .

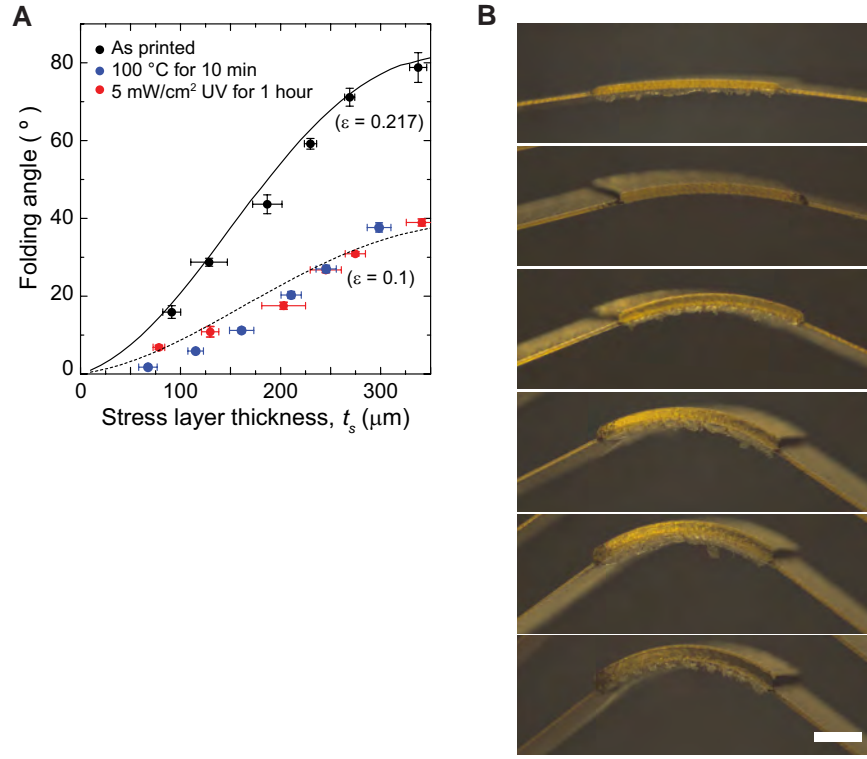


Figure 5-6: **Effect of heating and high UV dose on the folding behavior.** **A.** The overall geometry is as shown in Fig. 5-2A with the values $t_r = 80.1 \pm 5.8 \mu\text{m}$, $W = 3.25 \text{ mm}$ and $L_s = 4 \text{ mm}$. To measure the effect of high UV dose, samples were exposed to 5 mW/cm^2 UV source (measured at 365 nm) for 1 hour before they were removed from the printed substrate in the flat state. Similarly, identical samples were also placed in a convection oven at $100 \text{ }^\circ\text{C}$ for 10 min before being removed from the printed substrate. Some samples were kept as printed with no additional UV dose or high temperature exposure. The samples were peeled and the folding angles were measured after an interval of 15 min in all cases. The measured angles of the as-printed samples, and samples exposed to additional UV dose and heat are shown in black, red and blue, respectively. The folding angle for each point is obtained from three samples, and the error bars show the standard deviation. The solid curve shows the finite element computation using the actual device geometry, and the initial strain (0.22). The measurements show a good fit. The input strain is effectively reduced to $\varepsilon \approx 0.1$, for the cases with the high UV dose and heat exposure. We estimate that the reduction in the two cases is a result of additional crosslinks due to the hour long UV exposure (limiting the expansion of the stress layer), and polymer chain realignment due to the high temperatures respectively. **B.** Optical microscope images of the samples corresponding to black data points in ‘A’. Scale bar is 1 mm.

5.5 Self-folding composites

Entire composites that self-fold can be fabricated with our multimaterial printer. Here, 6 materials are printed together to demonstrate the potential for using this material system in self-folding electronic composites. While active printed electronics have been described in previous chapters, it is important to recognize that when solvent based inks are printed, the underlying substrate has to be locally flat to restrict movement of the ink during the printing process. It is therefore challenging to directly print fully-folded composites with embedded electronics, containing curved structures with overhangs. STR and RIG are used as the overall mechanical structural materials and act as a substrate for the other materials: an elastic layer (ELA) to control the surface energy, reactive silver ink⁵⁸ to make the contacts, PEDOT:PSS, and an electrolyte as previously described. STR, RIG, and ELA are UV cured. The convective heater is used with the reactive silver ink to initiate precipitation of the silver nanoparticles, and evaporate the solvent in the PEDOT:PSS layers. In the final device, the applied voltage controls the movement of metal ions from the electrolyte into the PEDOT:PSS channel. This de-dopes the PEDOT:PSS, leading to a change in the optical contrast and electrical conductivity as described previously. The design of the composite and the cross-sectional schematic are shown in Fig. 5-7A. Figure 5-7B shows the printed composite on a glass slide, with the red lines showing the cross section path. The rigid material and the stress layer form the mechanical substrate for the electrochromic pixel. The overall thickness of the rigid substrate is $\sim 425\ \mu\text{m}$; in the bilayer portions of the device the thickness is split as a $100\ \mu\text{m}$ thick rigid layer and $325\ \mu\text{m}$ thick residual stress layer. The elastic material used as a favorable surface energy coating is $\sim 50\ \mu\text{m}$ thick (3 layers) in a typical device. After solvent evaporation the thickness of the printed silver trace and the PEDOT:PSS layer are typically around $10\ \mu\text{m}$ and $1\ \mu\text{m}$ respectively, as described in previous chapters. After these layers are printed, the electrolyte and the cap regions are completed, along with the thin protection layer (typically 3 layers) on top of the silver traces. The silver traces are exposed at the textured contact region for electrical connections,

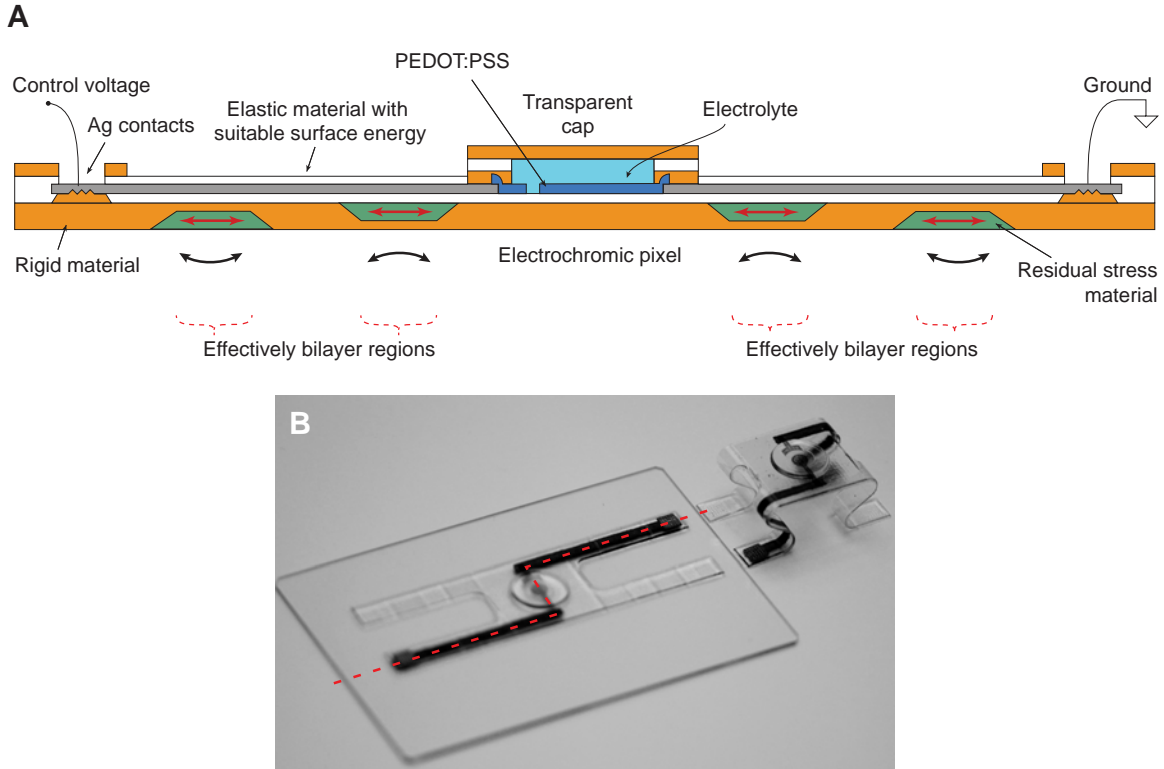


Figure 5-7: **Design of the electronic composite.** **A.** The cross-sectional schematic of the self-folding electronic composite showing the 6 different materials (not to scale). The rigid material and residual stress material form the basic substrate for the electrochromic pixel. The silver ink and the PEDOT:PSS layers are printed on top of ~ 3 layers of the elastic material with suitable surface energy (white). The electrolyte bridges the control terminal and the electrochromic pixel pattern (PEDOT:PSS). The rigid material forms a transparent cap for the enclosed electrolyte. The cross section is drawn along the line mapped in 'B' in red. **B.** Image of the composite as printed, and another sample a week after it was removed from the print platform. The glass slide is $2'' \times 3''$, for scale

and are surrounded by rigid material to provide additional stiffness. The composite is removed from the print substrate and used as is. Figure 5-7B shows a sample 1 week after being removed from the print substrate.

Figure 5-8A shows a printed self-folding structure with an embedded electrochromic pixel, 5 mins after removal from the print platform. The finite element simulation of the folded structure (without any fitting parameters) shows a good match, with most of the stress concentrated in the rigid material at the bilayer regions. The elastic modulus of the rigid material 5 min after application of the load (~ 1279 MPa,

from Fig. 5-2B) and $\varepsilon = 0.22$ are used for the results shown in Fig. 5-8B. The electrochromic structure utilizes the optical contrast between the oxidized and reduced states of the PEDOT:PSS film that can be electrically controlled. The stretchable conductor is subjected to compressive and tensile strains in adjacent folds in the two legs that provide electrical contacts. The precipitated silver nanoparticle layers that make up the stretchable conductor remain conductive until mechanical breakage of the underlying polymer (up to $\sim 40\%$ strain) as shown in an earlier chapter. When the polarity of the control voltage (1 V) is switched, the transmission through the pixel changes as shown in the inset at the bottom in Fig. 5-8A.

The shape of the composite changes over time, and Fig. 5-8C shows the shape change in an array of prints over the course of 1 week. While the shape change over time may be desirable in certain applications, it is equally desirable to achieve fixed folds at controllable angles irrespective of the external temperature fluctuations. Mechanical stops can be designed for this purpose, on either side of the bilayer stack as shown in Fig. 5-8D (top). On removing the structures from the substrate, and even when exposed to a hot air gun set to $100\text{ }^\circ\text{C}$ for 1 min, the folds stop at predesigned angles as shown in the bottom. The desired stop angles can be designed and controlled accurately based on the geometry (Fig. 5-8D bottom image and plot in Fig. 5-9)

At first it appears that only small folding angles are achievable at room temperature ($25\text{ }^\circ\text{C}$), and that the folding angle continues to change for at least over 2 days (Fig. 5-2A). It is important to note that only r_d , the radius of curvature is constrained, i.e., larger folding angles can be obtained by simply increasing L_s . Mechanical stops can be designed to limit folding at the desired radius of curvature (time). If the materials in the composite do not degrade with a small temperature increase, a small radius of curvature or accelerated folding can be achieved (at $35\text{ }^\circ\text{C}$). While generating folds from planar composites, it is expected that the achievable geometries are analogous to shapes from planar origami. The geometric limitations here come from the achievable radius of curvature and the temporal characteristics elaborated earlier.

Flattening a fold typically takes about $\sim 0.1\text{ N}$ of force for the structures described so far; Fig. 5-10 summarizes experiments on unfolding forces. Figure 5-10A shows

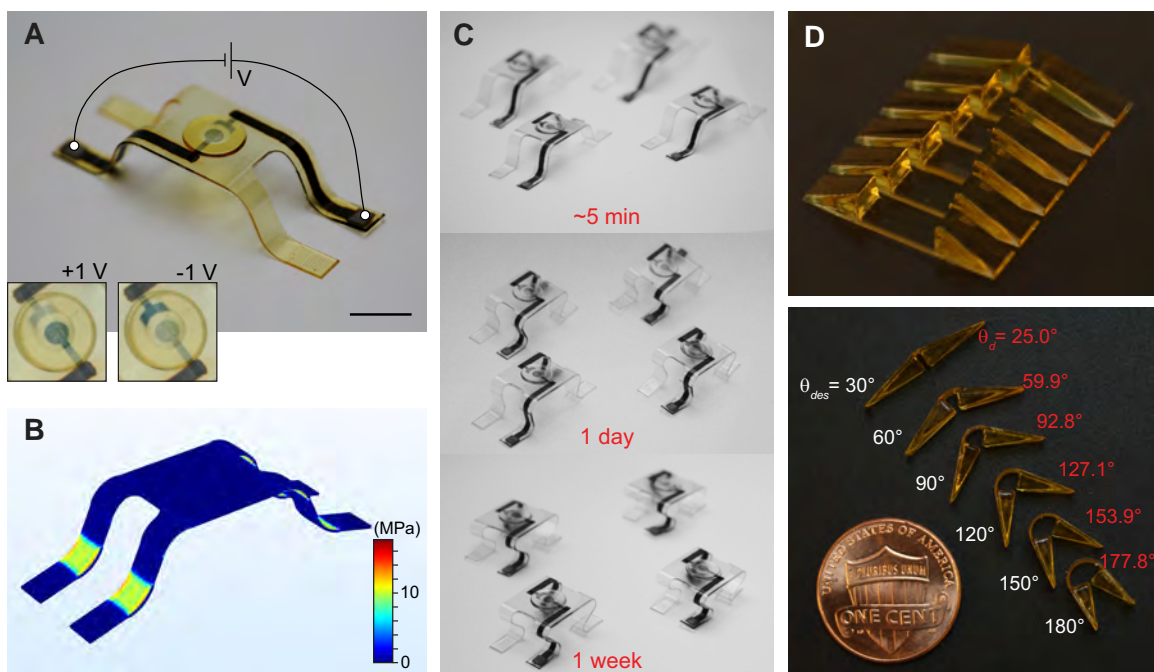


Figure 5-8: **Self-folding electronic composites.** **A.** Image shows an electrochromic element integrated in a spontaneously folding fully-printed composite. The composite consists of 6 materials that are printed simultaneously using no external processing. The transmission through the electrochromic ink (PEDOT:PSS) can be modulated by applying a voltage as shown in the bottom. The stretchable printed conductor provides electrical contacts through the folded legs. Scale bar is 10 mm. **B.** Finite element simulations using the equivalent input strain (0.22) obtained earlier shows a close match to the deformed structure ~ 5 min after removal from the print substrate as shown in ‘A’. The von Mises stress in structure is seen to be concentrated in the bilayer regions of the legs. **C.** Series of photographs shows the change in the folding angles over the course of a week. **D.** Printed bilayer structures with folding stops, before removal from the platform (top) and a set of structures after reaching steady state folding angles.

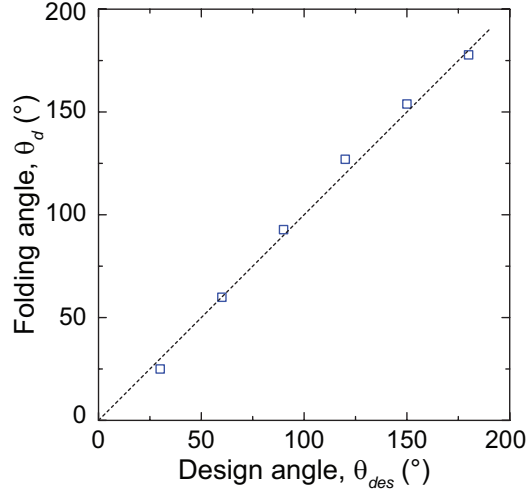


Figure 5-9: **Folding angle with stops.** For applications where a specific folding angle is preferred, the geometry can be modified to include folding stops. The length of the bilayer region, L_s , is obtained as a product of the desired folding angle, θ_d , and height of the stop. The height of the stop corresponds to the final radius of curvature. The thickness of the stress layer is designed such that a far smaller radius of the curvature is achievable. The plot shows the measured folding angle as a function of the designed angle (sample shown in Fig. 5-8D). The final folding angles match the designed values.

one of the folded legs of the composite weighed down by a binder clip (2.71 g). When the sample with a 180° mechanical stop is loaded with the same load (26.6 mN), it is also straightened. A quantitative measurement of the force required to open this sample is shown in Fig. 5-10C. Figure 5-10D shows the flattening load acquired from FEM simulations (0.12 N).

It is noteworthy that all samples rely on residual stress created in the in-plane printing directions for folding. During the printing process, the uppermost printed layers are unconstrained on the upper side and free to swell in the z -direction. To control the magnitude of the equivalent inbuilt strain, several approaches exist. The amount of swelling can be increased by increasing the layer printing time leading to a larger residual stress. Additionally, a multimaterial process like ours allows for using multiple inks with widely different swelling ratios allowing excellent spatial resolution in the prescription of residual stress.

Overall, this residual stress based folding method provides a new route to design

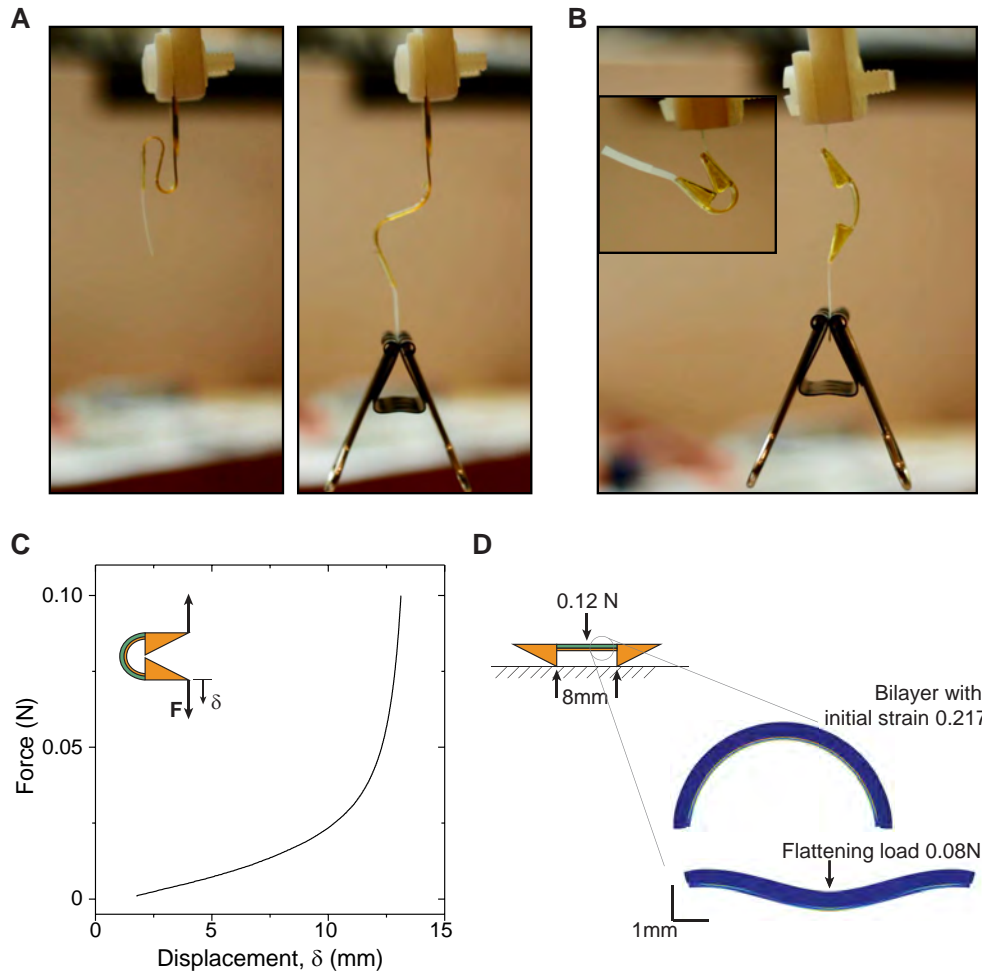


Figure 5-10: **Unfolding forces** **A.** Images show the effect of loading one of the folded legs from the composite with a binder clip (2.71 g) **B.** Loading the design with 180° mechanical stop with the same load (26.6 mN). **C.** The force-displacement measurement for the sample in ‘B’ was performed using the DMA. The plot shows that the typical force required to unfold our sample is of the order of ~ 100 mN. The displacement at full extension is ~ 14 mm. The thickness of the elastic and rigid layers are 0.3 mm and 0.1 mm respectively. **D.** To flatten the device, a point load of 0.12 N is required at the center. This corresponds to a maximum bending moment of 0.12×10^{-3} N-m at the center. The images on the right show the COMSOL simulations for the bilayer in the sample in ‘B’ and the sample with a point load of 80 mN applied in the middle.

3D shapes folded from planar polymer composites at room temperature. Furthermore, the ability to control the degree of folding based on the design geometry enables designs that are tolerant to small temperature changes. The formulated inks and the corresponding material characterization results provide all the tools to design, simulate and fabricate new geometries. The demonstrated self-folding electronic composite, fabricated without using any external processing, is expected to enable electronics in new form factors.

5.6 Experimental methods

Material characterization and folding measurements: Mechanical stress-strain tests for the material with residual stress (Fig. 4-5), and controlled deformation in samples for Poisson's ratio estimation were performed using with Instron 5944 (Instron, Norwood, MA, USA), a single column table top mechanical testing system. Stress relaxation measurements for the residual stress material (in the linear regime, at 2.5 % strain) and the creep compliance measurements for the rigid material (at 0.5 MPa stress), and storage and loss modulus measurements (1 Hz cycling) for all materials were performed using DMA Q800 (TA instruments, New Castle, DE, USA). Differential scanning calorimetry measurements were performed using DSC Q100 (TA instruments, New Castle, DE, USA). Thickness measurements for printed samples were performed using DektakXT stylus profilometer (Bruker Corp., Billerica, MA, USA) and optical microscope SZ61 (Olympus Corp., Tokyo, Japan) fitted with SC30 3.3 MP microscope digital camera (Olympus Corp., Tokyo, Japan). Folding angles were measured using the Stream Start software (Olympus Corp., Tokyo, Japan) from images taken using a Canon EOS 60D digital SLR camera and the SC30 microscope digital camera.

UV intensity and controlled temperature measurements: UV light intensities were measured using a Loctite UV A/B Radiometer Dosimeter (1390323, Loctite Henkel, Dusseldorf, Germany). The broadband high intensity UV source used was a F300 Heraeus system with the LC6B Benchtop conveyor (Fusion UV/Heraeus,

Maryland, USA). For measurements of folding angles at controlled temperatures, a universal oven UF 30 (Mettler, Schwabach, Germany) is used to setup a controlled temperature atmosphere. The hot air gun in X-tronic 5000 series rework station (Model #5040-XTS, X-tronic Int., Lincoln, NE, USA) was used to generate the hot air temperature variation for the samples with mechanical stops in Fig. 5-8D.

FTIR measurements and doublebond conversion: FTIR spectra in Fig. 4-2 were obtained using the Thermo Fischer FTIR 6700 Fourier Transform Infrared Spectrometer setup in the attenuated total reflection (ATR) mode with a Silicon crystal. Spectra were measured on three samples on the surface for each data point. The ratio between the absorbance of the vinyl group (809 cm^{-1}) with respect to the carbonyl group (1705 cm^{-1}) is used to measure the monomer conversion percentage similar to the technique used in a reference⁶⁶.

Part III

3D-Printed Actuators - *a case for automated design*

Chapter 6

Multimaterial magnetic actuators

Actuator fabrication at the mesoscale has received a boost from the rapid progress in additive manufacturing techniques that have enabled precision manufacturing of complex structures with diverse materials. Aided by the development of new materials in parallel, this has enabled the fabrication of structures with extremal properties and programmable biomimetic shapes. Interest in 3D-printed actuators is also growing due to their applicability for use in robotics - across all length scales. Demonstrations such as arrays of artificial cilia^{102,103} are particularly useful for micro/mesoscale robotics^{104–106}. Magnetic actuation in particular has been explored extensively^{107,108} for soft matter applications¹⁰⁹ due to its favorable scaling, high actuating force density and potential for untethered actuation¹¹⁰. Methods to develop 3D-printed mesoscale, magnetic actuators is the focus of this chapter.

6.1 3D-printed mesoscale magnetic actuators

The main materials used here are a rigid acrylic polymer (RIG), an elastic polymer (ELA) and a magnetic nanoparticle/polymer composite (MPC). The full formulations are in the appendix. The starting inks are formulated from acrylate monomers and

Contents of this chapter are adapted from a manuscript in preparation - S. Sundaram, M. Skouras, D. S. Kim, L. van den Heuvel, W. Matusik, “Topology-optimization and 3D-printing of multimaterial magnetic actuators and displays”, *in preparation*, May 2018.

oligomers along with photoinitiators that absorb at 365 nm (*i*-line), and are optimized for an inkjet printing process as done earlier. As a first step here, we print slabs of different materials and characterize the material properties (see Fig. 6-1). The figure shows a set of properties: transmission through the MPC material as function of thickness, optical transmission through RIG, magnetization curves for MPC and stress-strain curves for the 3 materials. The material is indicated as a cube in the bottom right (brown, yellow and gray correspond to MPC, RIG and ELA respectively). The crosslinked magnetic material (MPC) is nearly opaque beyond $\sim 100 \mu\text{m}$ thickness while the rigid polymer (RIG) is nearly transparent as shown in the transmission factor measurements in Fig. 6-1A and 6-1B. In this case, RIG was specifically optimized to be transparent by varying the photoinitiators in the formulation. The magnetic composite, MPC ($\sim 12 \text{ wt}\%$ Fe_3O_4 nanoparticles in the acrylic polymer ink; see thermogravimetric analysis in Fig. 6-2) with a saturation magnetization of $\sim 5 \text{ emu/g}$ (see Fig. 6-1C) is used to generate the forces and torques in our actuators. The three materials also have widely varying elastic moduli - ELA (528 kPa), MPC (507 MPa) and RIG (1290 MPa) - averaged from 3 individual samples. Representative stress - strain curves are shown in Fig. 6-1D, 6-1E and 6-1F. The contrast in the optical transmission, elastic moduli and magnetic properties is utilized in designing the appearance, displacement and forces in our actuators.

To first demonstrate the capabilities of our base material set, we fabricate a variety of multimaterial actuator arrays designed manually. The fundamental design unit used in our actuator arrays is illustrated in Fig. 6-3A. In this design, a square panel of size l_p and thickness t_p is partitioned into two halves of the RIG and MPC materials. The panel is suspended at the center by two identical elastic torsional hinges (ELA) of length l_h , width w_h and thickness t_h . On the application of a magnetic field, the paramagnetic material in the MPC region of the structure is attracted towards the magnetic field, generating a net torque that is balanced by the torsional springs. The general design is extended to generate 2-axis torsion in the panel by adding a rotating frame tilting in orthogonal directions. A printed 2×2 array of 2-axis rotating panels is shown in Fig. 6-3B under an applied magnetic field (using a permanent magnet).

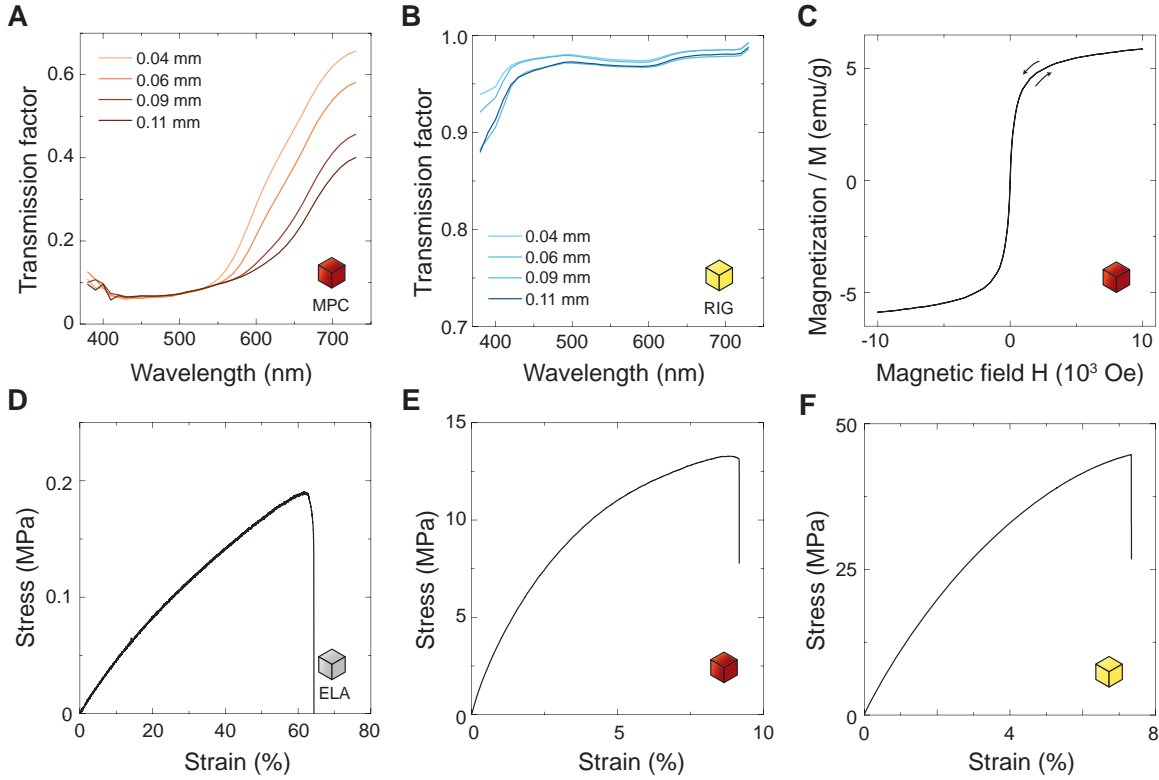


Figure 6-1: **Material property library.** **A.** The transmission through the MPC shown as a function of the wavelength for films of varying thickness, measured using a spectrophotometer. **B.** The transmission through the clear rigid material shown as a function of wavelength for multiple film thicknesses. **C.** Magnetization versus applied magnetic field for the MPC measured at room temperature. Magnetic nanoparticles make up $\sim 12\%$ of the overall weight of the MPC. Typical mechanical stress-strain curves for the elastic polymer (ELA), MPC and the rigid polymer (RIG) are shown in ‘D’, ‘E’ and ‘F’ respectively. Elastic moduli of the polymers at linear strains, averaged from three samples each, vary significantly - ELA (528 kPa), MPC (507 MPa) and RIG (1290 MPa).

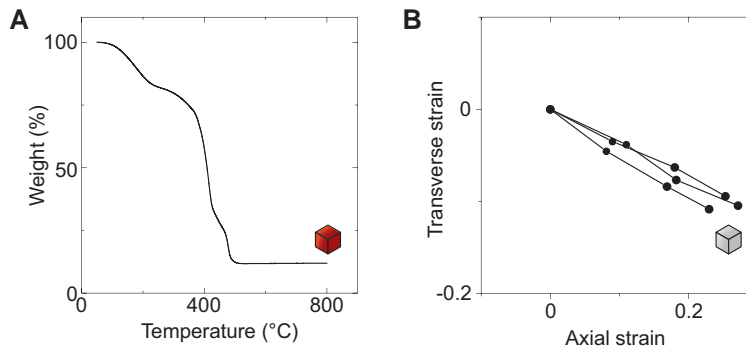


Figure 6-2: **Material characteristics.** **A.** Thermogravimetry measurements of an MPC slab shows $\sim 12\%$ nanoparticle loading. **B.** Poisson's ratio measurement for the elastic polymer (ELA).

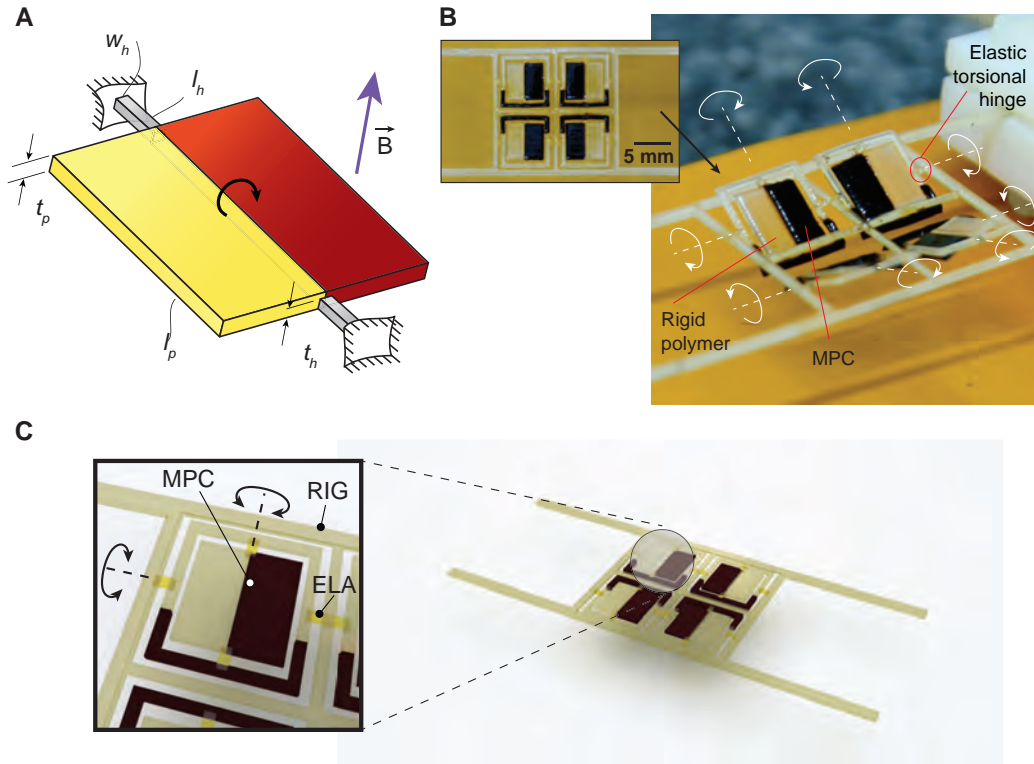


Figure 6-3: **Actuator design A.** The schematic shows the fundamental hinge-based design with panel length l_p , and thickness t_p . In this design, the panel is sectioned into two equal portions of RIG and MPC. The panel is attached to rigid boundaries on two sides with ELA torsional hinges of length l_h , width w_h , and thickness t_h . On the application of a magnetic field, the magnetic portion of the panel generates a torque. This is used as the fundamental block in actuators. **B.** Image of a 2×2 array of panels each with two axes of rotation. The dark brown regions of the image show the MPC material, and the translucent portions show the rigid materials. The elastic torsional hinges are nearly identical to the rigid polymer in appearance. On the application of a magnetic field, each panel exhibits a unique combination of two-axis angular rotations. The top view of the flat as-printed sample is shown on the left. **C.** Scaled rendering of the 2×2 array of panels shows the three materials used in the design. The hinges (0.5 mm long) are made out of the elastic polymer (ELA), while each 5 mm panel is split equally into regions with MPC and the clear rigid material (RIG). Each panel is held by another frame that can itself tilt in an orthogonal direction.

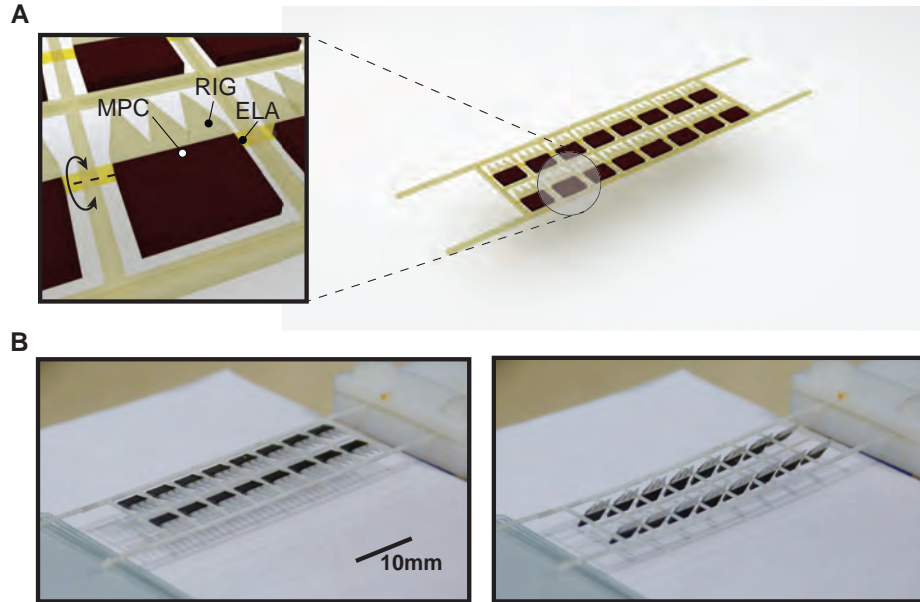


Figure 6-4: **Actuator arrays** **A.** Rendering of the actuator array showing the ELA, RIG and MPC regions. **B.** Panels tilt uniformly on the application of a magnetic field. Here the magnet is held ~ 5 mm from the printed part, closer than the typical distance of 1 cm used in the rest of this chapter.

The design of the 2-axis panel is shown as a rendering in Fig. 6-3C showing the RIG, ELA and MPC regions. It is quite straightforward to scale the number of elements in a printed actuator array. Figure 6-4 shows an array of 16 actuators that are printed together - the spikes on one side are modeled after the spiked scales seen on shark skins.

To highlight the potential of multimaterial actuator arrays in passive display applications, we enhance the fundamental actuator design (Fig. 6-3A) with two extra materials, as shown in Fig. 6-5A. Vertical slabs are printed on top of each panel with RIG mixed with a white pigment. The sides of the vertical slabs are textured with cyan-colored polymer such that different images can be displayed by controlling the panel's pitch. The panel array is designed to show the letters "MIT" when actuated by a magnetic field. To dynamically actuate our printed actuators, we utilize an electromagnet powered by a current source to generate a tunable magnetic field (see experimental methods section). We print an array of 6 elements on a special substrate to produce a mirror-like finish on one side of the print. This substrate is

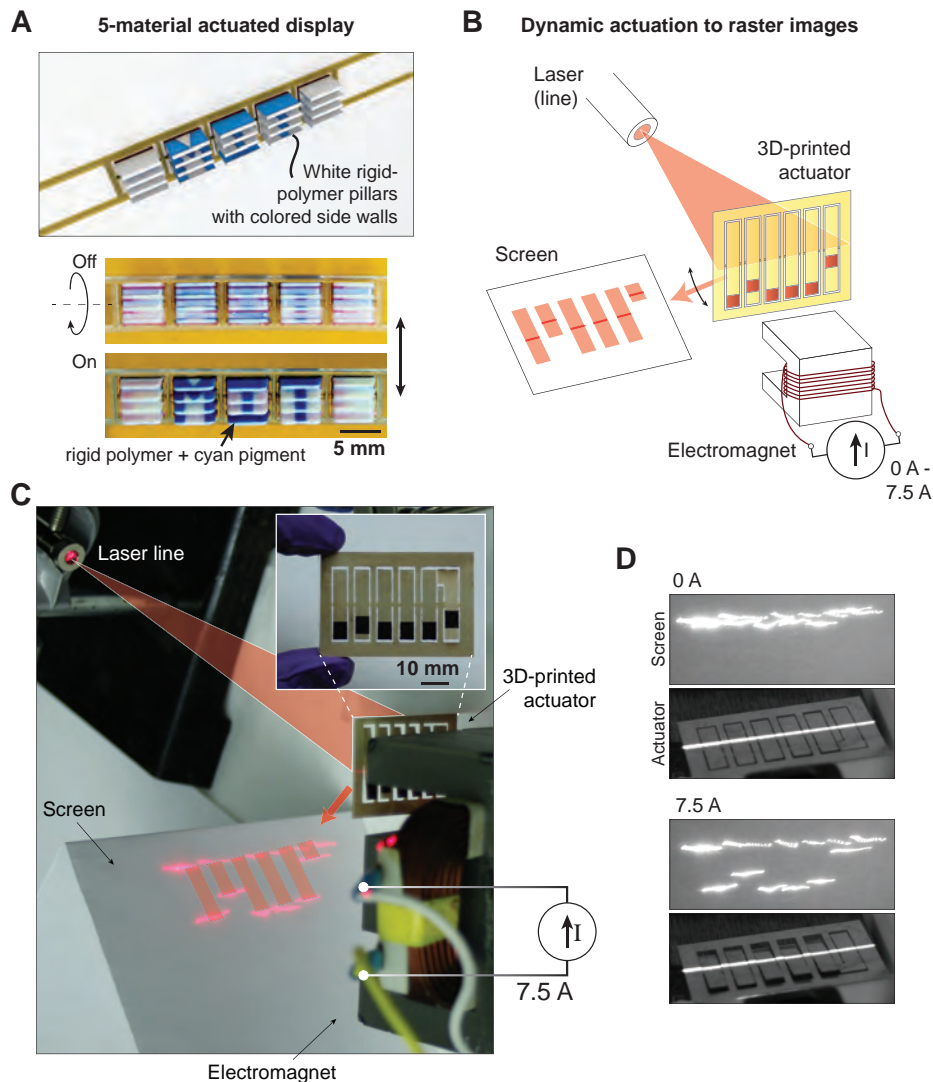


Figure 6-5: **Magnetically actuated displays.** **A.** 5-material actuated display. Each panel consists of the design shown in Fig. 6-3A on top of which 4 vertical walls of a white rigid polymer are printed. The side walls are patterned based on the image to be displayed. Here the letters “MIT” are patterned on the sidewall. An applied magnetic field generates a torque on the panel allowing different sides of the walls to be visible from a fixed viewing angle. **B.** A 6-element array of mirrors is mounted next to an electromagnet powered by a current source (0 A - 7.5 A). The torque experienced by each individual panel is controlled by the position of the MPC regions. Different images are rastered on a screen by shining a laser line across the mirror array. Here the panels are designed to raster the MIT logo. The physical setup is shown in ‘C’. **D.** The two sets of images show the still photographs of the screen, and a snapshot of the mirror array with the electromagnet turned off and on (7.5 A).

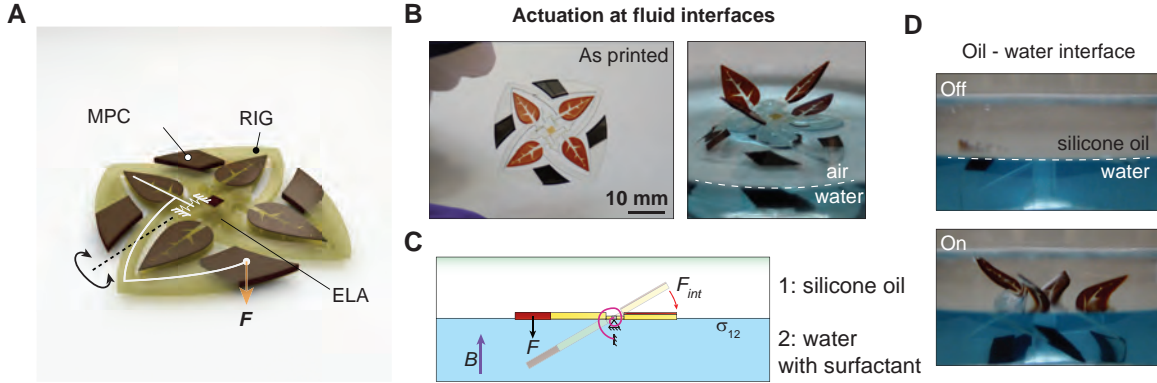


Figure 6-6: **Magnetic actuation at fluid interfaces.** To demonstrate the use of the magnetic actuator arrays at fluid interfaces, we designed water lilies that are positioned on air-water, and silicone oil-water interfaces. **A.** Rendering shows the design of the lily. The petal patterns are printed using 3 layers of the magnetic ink, and torsional hinges are made from the elastic polymer. **B.** The top view of the as-printed part is shown where the solid dark regions are the actuating regions made with MPC. (Right) When placed on the air-water (with 0.2 % FC4430, $\sigma = 20.9$ mN/m) interface, the leaves are held flat due to the interfacial tension of water. While it can be deformed by an applied field as shown, actuation is challenging when the water is disturbed. **C.** When tested in conditions with lower interfacial tension $\sigma_{12} = 3.7 \pm 0.78$ mN/m (interface of silicone oil and water with 0.2 % FC4430), the array can be actuated back and forth reliably. The schematic shows the restoring nature of the interfacial tension. **D.** Experimental results of actuation at the silicone oil-water interface.

prepared by drop casting and annealing the silver ink used in previous chapters, on a polyimide sheet (see appendix for formulation). The silver layer peels along with the print as the actuator array is removed from the polyimide film (after printing). The silver regions freely exposed on both sides are then etched. A laser line is projected on to the reflective side of these panels and the angular tilt of the panels is dynamically controlled using the electromagnet using the setup schematically shown in Fig. 6-5B (corresponding image in 6-5C). The laser line reflected from the mirror array is imaged on a screen; here, the panels are designed to tilt differently to raster the MIT logo shown in red. The two images shown in Fig. 6-5D are photographs of the laser line on the printed actuator array, and the screen when the electromagnet is turned off, and when powered by a 7.5 A current source (magnetic field settings are described in experimental methods section at the end of this chapter).

A critical advantage of magnetic actuation is in the potential for untethered actu-

ation, which is particularly useful in conductive or liquid environments, where electrically driven actuators need careful electrical isolation. In Fig. 6-6, we show untethered actuation in conductive fluid interfaces. Figure 6-6A shows a rendering of the actuator design, and Fig. 6-6B shows the as-printed sample containing four individual petals that can be actuated. When the printed device is placed on the air-water (with surfactant, and colored blue) interface, as shown on the right, the petals can be lifted up from the water surface by attracting the magnetic regions. However, the larger interfacial tension makes repeatable actuation challenging. Repeated actuation cycles can be performed when the printed sample is placed at the silicone oil - water interface (interfacial tension $\sigma_{12} = \sim 3.7$ mN/m), schematically shown in Fig. 6-6C. Experimental results are shown in Fig. 6-6D. It is noteworthy that the elastic hinge effectively acts as a rotating joint here. The torsional stiffness is dominated by the interfacial tension experienced by the petals when leaving the silicone oil-water interface.

6.2 Magnetic actuator characteristics

Previous results show a variety of actuators where untethered actuation is useful, in a qualitative fashion. We now focus on the quantitative characterization of these actuators. For this, we consider a variant of the general actuator unit (Fig. 6-7A). The thickness of the hinge, t_h , is varied from 0.3 mm to 0.5 mm across these samples and λ , the fraction of the magnetic region is varied between 0.1 and 0.2. The other dimensions are $l_p = 9$ mm, $l_h = 1$ mm, $t_p = 1$ mm, $w_h = 0.5$ mm. The results shown in Fig. 6-7B show the angular deflection of the panel as a function of the distance between the actuator and a permanent magnet. Here we used a 2" \times 2" \times 0.5" bar-shaped Neodymium grade N52 magnet magnetized along its vertical axis. In all our static deflection measurements, we placed the samples ~ 1 cm from the surface of the magnet, along the magnetic axis. In this case, the magnetic field can be derived analytically from Maxwell equations¹¹¹ and is a function of the dimensions a , b and c of the magnet (Fig. 6-8A) and its magnetization $\mathbf{M} = M\mathbf{e}_z$ that we assume to

be constant. With the origin of the coordinate system located at the center of the magnet, the field $\mathbf{H} = (H_x, H_y, H_z)$ can be written as

$$H_x(x, y, z) = \frac{M}{4\pi} \sum_{k,l,m=1}^2 (-1)^{k+l+m} \ln(y + (-1)^l b + r_{klm}(x, y, z)), \quad (6.1)$$

$$H_y(x, y, z) = \frac{M}{4\pi} \sum_{k,l,m=1}^2 (-1)^{k+l+m} \ln(x + (-1)^k a + r_{klm}(x, y, z)), \quad (6.2)$$

$$H_z(x, y, z) = \frac{M}{4\pi} \sum_{k,l,m=1}^2 (-1)^{k+l+m} \operatorname{atan}\left(\frac{(x + (-1)^k a)(y + (-1)^l b)}{(z + (-1)^m c)r_{klm}(x, y, z)}\right), \quad (6.3)$$

$$r_{klm}(x, y, z) = \sqrt{(x + (-1)^k a)^2 + (y + (-1)^l b)^2 + (z + (-1)^m c)^2}. \quad (6.4)$$

We used $M = 950$ kA/m as the value for the magnetization, obtained by fitting the analytical magnetic flux density $\mathbf{B} = \mu_0 \mathbf{H}$ to sample values (see Fig. 6-8B - D). We model the magnetization of the MPC cell using the hyperbolic tangent function as $M(\mathbf{H}) = \pm 5.67 \tanh(2.8 \times 10^{-2} \sqrt{\|\mathbf{H}\|_2})$, with \mathbf{H} expressed in [Oe], which is in good agreement with the measured data (Fig. 6-8D). All our magnetic field measurements were performed using a F. W. Bell 9500 gaussmeter with a probe (~ 4.5 mm \times 4.5 mm). Measurement were typically made in the 3 kG range, which has a reported accuracy of ± 30 G (or the 300 mT range, ± 3 mT).

We then characterized the force produced by our actuators by using designs shown in Fig. 6-7A. In particular, we used actuators with the following dimensions: $t_p = 1$ mm, $\lambda = 0.15$, $l_p = 9$ mm, $t_h = 0.25$ mm, $w_h = 0.5$ mm, and $l_h = 1$ mm. It is typically hard to measure small forces in the presence of a large magnetic field using commercial force probes. We therefore used polyimide cantilevers of calibrated stiffnesses $k_{cant} = 105.92 \pm 12.04$ mN/m cut from 0.002" thick Kapton-polyimide film (length 0.6", width 0.125") as force probes. In order to measure the blocking force, we measured the deflection of the calibration cantilever from the force exerted by the outermost edge of the panel (arm of 4.5 mm from the axis of rotation). Figure 6-9A shows the forces measured from 4 identical devices as a function of the distance from

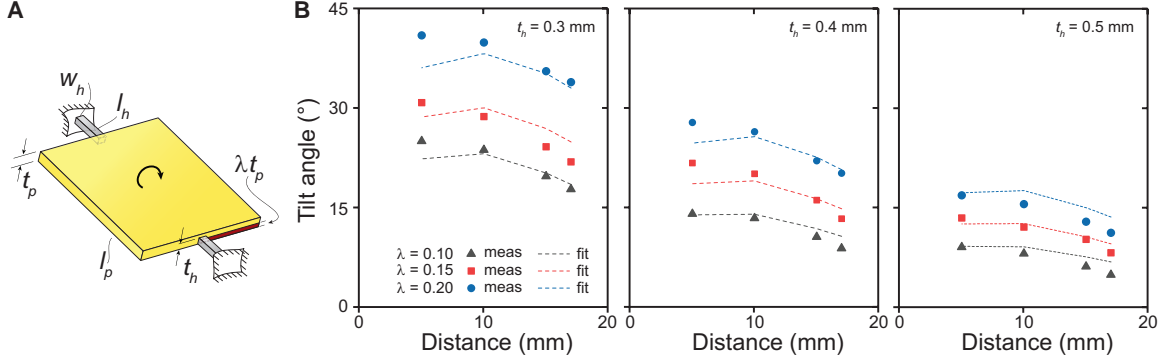


Figure 6-7: **Experimental verification of tilting angles.** **A.** A single panel actuator was designed with magnetic material on one half of the panel for a fraction of the thickness λ . To verify the tilting angle as a function of geometric design changes, the fraction λ and thickness of the hinge, t_h , were varied. **B.** Experimental measurements of tilting angles are shown as a function of the distance from the permanent magnet, along with the results of simulations using our soft-joint solver (see next chapter). It can be seen that as the ratio of the magnetic material thickness, λ , is increased, the tilting angle scales nearly linearly with it. Further, as expected the angle of tilting reduces with the thickness of the hinge (torsional stiffness of the ELA hinge).

the magnet. Our actuators with these general dimensions typically produce $\sim 100 \mu\text{N}$ of force. When the blocking cantilever is removed the angular deflection of these devices can be directly measured, and this is shown in Fig. 6-9B.

We next estimated the speed at which these actuators can be actuated using an electromagnet. First we optically tracked the edge of the panel as it was actuated in the small amplitude regime ($< 1^\circ$) as the frequency of the current pulse was varied (duty cycle is 50%, peak current is 1.5A) from 0.01 Hz to 10 Hz. The angular displacement is measured for three identical devices described earlier; one is shown in Fig. 6-10A. The key point here is that our actuators exhibit a damped response. This is consistent with the measured loss modulus for our elastic material, where the loss modulus exceeds the storage modulus at 1 Hz actuation, at room temperature. Note that the elastic hinge in our actuators belongs to the same class of materials as the residual stress material (STR); see DMA measurement described in chapters in Part II. The -3 dB bandwidth of these devices is $\sim 0.32 - 0.56$ Hz from the plot shown in Fig. 6-10B. The plot shows the amplitude as a function of frequency for the devices characterized in Fig. 6-9.

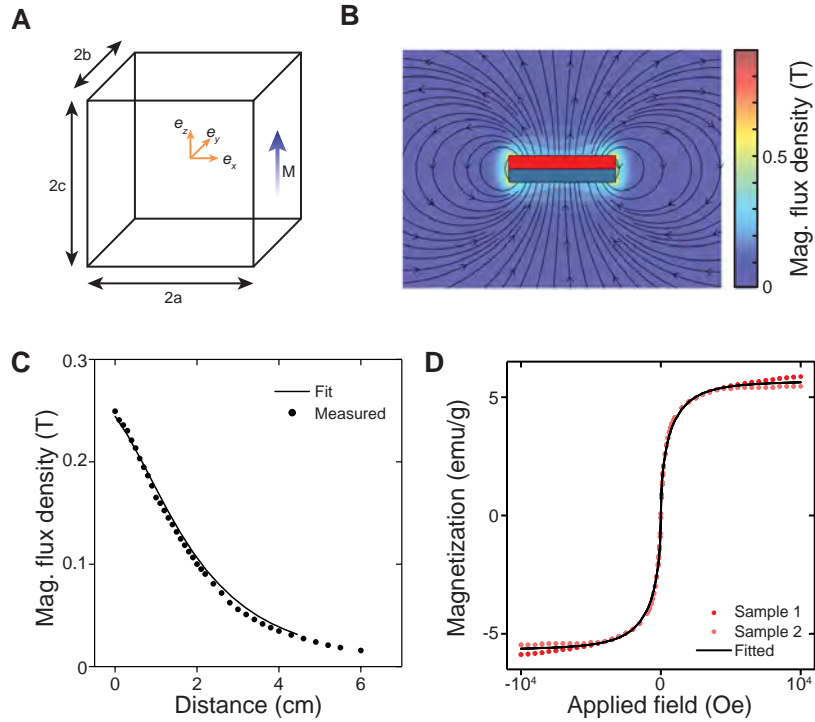


Figure 6-8: **Modeling of the external magnetic field.** **A.** Schematic representation of a permanent magnet vertically magnetized (see Methods for magnetic field computation using this coordinate system). **B.** Magnetic flux density analytically computed corresponding to a 2" \times 2" \times 0.5" magnet with a magnetic moment of 950 kA/m. **C.** Measured and fit magnetic flux densities corresponding to the magnet. **D.** Measured MPC magnetization curves.

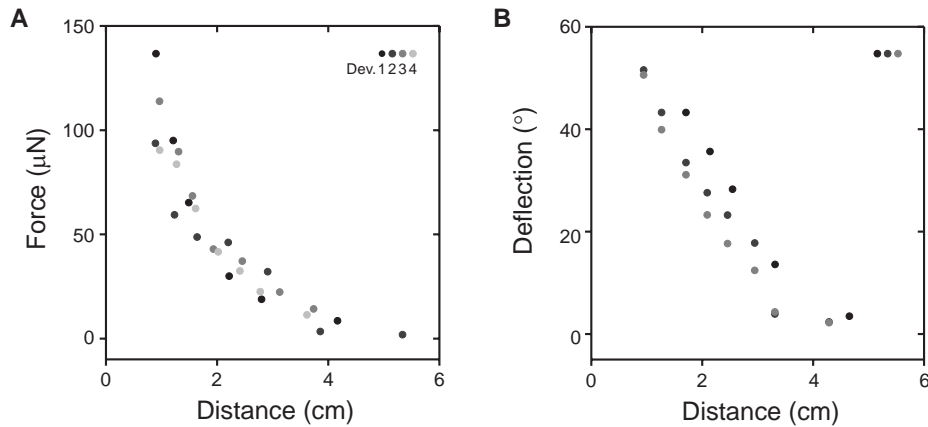


Figure 6-9: **Force generated by our actuators.** **A.** Blocking force generated by actuators with dimensions: $t_p = 1$ mm, $\lambda = 0.15$, $l_p = 9$ mm, $t_h = 0.25$ mm, $w_h = 0.5$ mm, and $l_h = 1$ mm. The plot shows measurements from 4 identical devices, as a function of the distance between the device and the permanent magnet (Fig. 6-8C). **B.** Measured angular deflections for 3 identical devices.

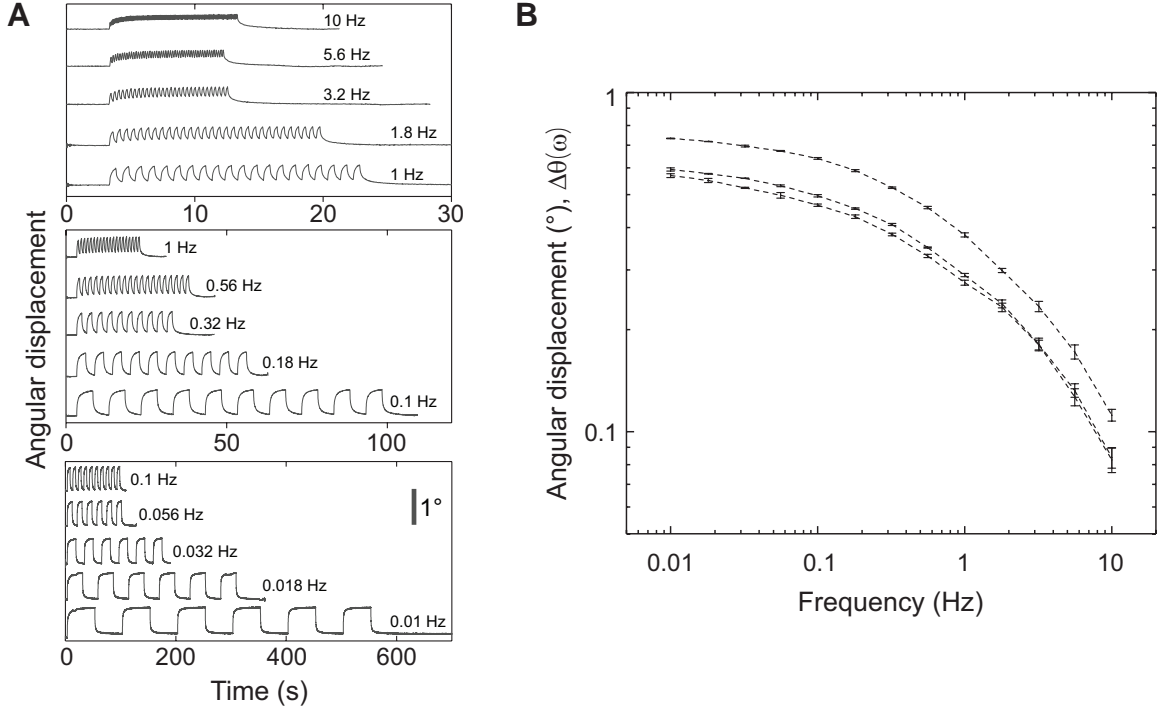


Figure 6-10: **Switching transients and bandwidth measurements.** **A.** Measured angular displacement as a function of time when the magnetic field is cycled (0.5 duty cycle) at varying frequencies. **B.** The plot shows the amplitude of angular deflection as a function of actuation frequency for 3 identical devices. The magnetic field was generated using the electromagnet powered by 1.5 A (measured peak magnetic field is ~ 10 mT).

The bandwidth estimation for large amplitude deflection is less straightforward. While the exact same measurement of cycling the magnetic field can be performed, the force experienced by the panel itself increases with increasing deflection. Therefore, the bandwidth for large amplitude deflections can be either much lower or higher depending on the actual force profile. To highlight this, we show two examples where the actuators are aligned differently - in one case, the force experienced by the actuator increases with increasing displacement (\star), in the other case, there is a stable angular position where the panel aligns with direction of maximum flux density and gradient ($\star\star$). The transient responses are highlighted in Fig. 6-11A & B (the corresponding images are shown in Fig. 6-11C). The apparent bandwidth can be vastly different. These actuators have the same small amplitude bandwidths as shown in Fig. 6-10B. Depending on the actuating field setup, the effective bandwidth at large amplitudes

can vary from 0.32 Hz to 1.8 Hz.

These devices were tested for reliability by actuating them for over 1000 cycles at 0.56 Hz. In this case - like the large amplitude bandwidth measurements - the electromagnet was powered by a 7.5 A current source which was turned on and off using a solid state relay (SSR-25 DD) controlled by a sourcemeter. Our actuators show no degradation over 1000 cycles (~ 30 mins). The optically measured deflection is shown in Fig. 6-12. The angular deflections remain steady over the cycles and the actuator shows no apparent offset or drift in the angular position, and the actuator returns to its starting position. The elastic hinges which are the likely point of failure are stable at least up to 1000 cycles of $\sim 30^\circ$ displacement.

In summary, we fabricated a variety of mesoscale multimaterial actuators that unite soft polymers, rigid polymers, and magnetic nanoparticle loaded materials. These untethered actuators can produce forces in the order of $\sim 100 \mu\text{N}$, and can be actuated at a -3 dB bandwidth of ~ 0.32 Hz. The devices described in this chapter were designed by hand. The process and materials here enable the automated computational design and fabrication of more complex actuators described in the next chapter.

6.3 Experimental methods

Printing process details: The UV LED array in our printer used in this chapter has an increased intensity $\sim 2.1 \text{ W/cm}^2$ at 365 nm. The thin elastic (ELA) hinges used in our actuator designs are fragile. To facilitate easy removal, our samples were printed on a 125 μm sheet of polyimide (PI) (McMaster-Carr, Elmhurst, IL, USA) coated with a thin layer of poly(acrylic acid) (PAA $\sim 50 \text{ kg/mol}$, $\sim 25 \%$ sol. in water, Polysciences Inc., USA), prepared by drop casting. On completion of the print, the samples on the PAA-coated polyimide substrates were left in water overnight by which time, the printed part is detached from the substrate. For our samples with a silver mirror finish (Fig. 6-5), the silver layer was prepared by drop casting a reactive silver ink on a PI substrate and then sintered at 80°C for 2 mins on a hotplate. Structures

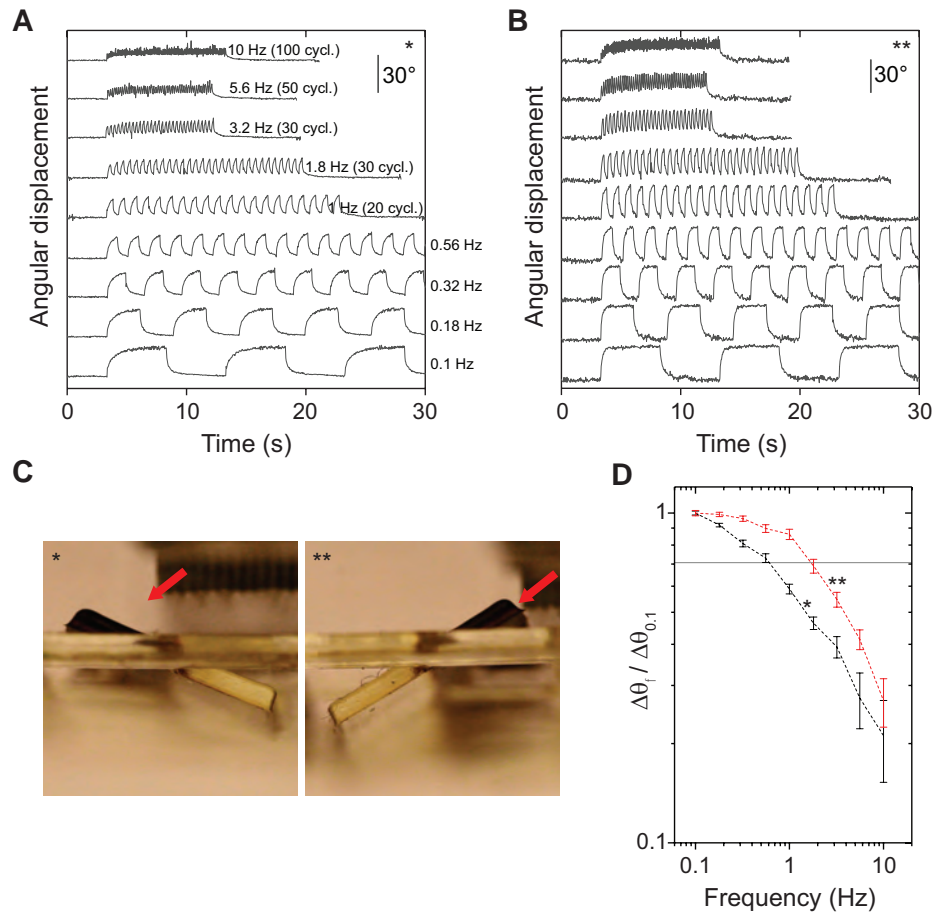


Figure 6-11: **Transient response - large amplitude actuation.** **A.** Measured amplitude as a function of actuation frequency for large amplitude oscillations. In this case, the field is oriented such that when the panel deflects, the force experienced by the magnetic portions keep increasing (*). **B.** When the panel is placed such that there is a stable angular displacement (**)- i.e., the panel is aligned along the direction of maximum flux density - the actuator can respond much faster. **C.** Images of the actuators for conditions explained in ‘A’ and ‘B’. **D.** The apparent bandwidth can vary a lot in the large amplitude regime based on the actuation magnetic flux density profile.

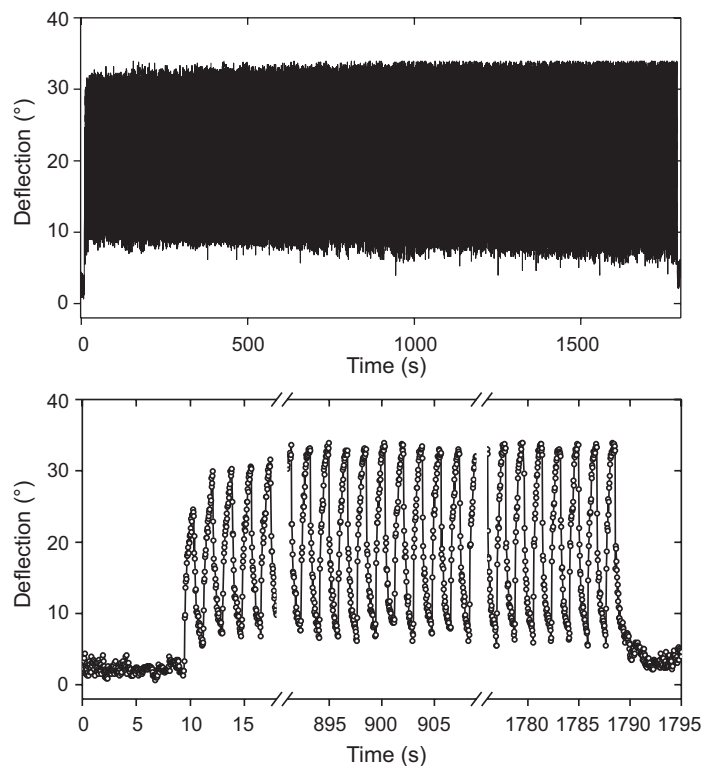


Figure 6-12: **Long term cycling test of the small actuator.** Top plot shows the measured deflection over 1000 actuation cycles. The maximum and minimum deflections remain quite stable. The plot below shows the deflection over few cycles at the beginning and the end. There is no visible offset after 1000 actuation cycles.

printed on top of the silver ink can be easily detached from the PI substrate since the precipitated silver nanoparticles adhere strongly to our UV cured polymers and weakly with the PI substrate. We used a 1:1 (vol) mixture of $\text{H}_2\text{O}_2:\text{NH}_4\text{OH}$ as the silver etchant to remove the freely exposed silver.

Polymer characterization measurements: Thermogravimetric analysis (TGA) measurements were performed using a Discovery-TGA (TA Instruments, USA). A 3D-printed slab of magnetic material (1 mm x 1 mm x 0.5 mm) was placed on top of a platinum pan and the sample temperature was ramped from 50 °C to 800 °C in air at a 10 °C/min ramp rate. The retained weight percent of the MPC was measured to be 11.93% verifying the nanoparticle loading (Fig. 6-2A). A larger weight percentage was measured when TGA was performed in nitrogen-rich atmospheres - potentially resulting from excess polymer retention after the tests.

Vibrating sample magnetometry (VSM): VSM measurements were performed

using an 800-VSM model (Microsense, USA). 8 mm disks of the MPC material were 3D-printed with varying thicknesses (0.1 mm to 1 mm), mounted on glass tips and characterized. Typically the applied magnetic field was cycled between -10^4 Oe to 10^4 Oe. The magnetization of the MPC samples saturated to ~ 5.7 emu/g.

Mechanical characterization: The stress-strain curve for each material was measured on a table top mechanical tester Instron 5944 (Instron, Norwood, MA, USA) with a 2 kN max load. The samples were 3D-printed and mechanically tested. The rigid polymer and MPC material were measured at 0.5 mm/min strain rate, and the elastic polymer was measured at 1.5 mm/min. Poisson’s ratio measurements were performed on 3D-printed samples of the elastic material using designs with 4 circular features along the x and y -axes of the sample. These axis aligned point pairs are positioned at equal distances. Samples were clamped on the Instron mechanical tester and a set of images were taken at various controlled strains. The distance along the x and y - axes for the 4 circular points were measured at varying strains with the optical microscope imaging software (Stream start software, Olympus Corp., Tokyo, Japan). Fig. 6-2B shows these measurements. The Poisson’s ratio was measured to be ~ 0.4 .

Spectrophotometer measurements: Transmission spectra were measured in the optical wavelength using a color i5 bench-top spectrophotometer (X-Rite, USA). Square slabs at varying thicknesses (ranging from 40 to 110 μm) were 3D-printed and the transmittance of the samples were measured.

Electromagnet setup: For our variable magnetic field experiments, we constructed an electromagnet using a consumer grade microwave oven transformer. The transformer was cut to enforce a flux path outside the core, and the secondary coil was removed. The primary coil (~ 114 turns) is retained in the core to generate the magnetic field. In laser rastering experiments, the primary coil was connected to a current source (up to 7.5 A). This allowed the field to be dynamically controlled up to ~ 45 mT at the sample location. The steepest gradient in the magnetic field is normal to the plane of the 6 mirror array causing the mirrors to tilt out of plane.

Silicone oil-water interface experiments: Interfacial tension measurements were performed with the DataPhysics FDS tensiometer (DataPhysics, Germany) using the

PT11Wilhelmy plate (10 mm × 19.9 mm × 0.2 mm) for air-liquid interface and with the RG11 Du Nouy Ring (18.7 mm diameter, 0.37 mm wire thickness) for the silicone oil-water interface.

Imaging and processing: All images and videos were acquired using DSLR cameras (Canon EOS 60D, or Canon EOS-1D X, Canon, USA). White balance and exposure were adjusted for visual clarity. Canon macro lens (EF 180mm f/3.5L Macro USM), Canon Zoom EFS 18-55 mm f/3.5 - 5.6, and Canon Zoom EF 28-80 mm f/3.5 - 5.6 were the lenses used.

Chapter 7

Topology-optimization for automated design and fabrication of actuators

Large mesoscale actuator arrays seen in contemporary electro-mechanical systems highlight the complex functionality that can be achieved by tiling identical actuators. For instance, the Digital Micromirror Device (DMD)¹¹² has evolved to include millions of individually addressable actuators¹¹³ and is at the heart of modern display technologies. Similarly the “Millipede”, a cantilever indentation based high density data storage system, first utilized a 1024-element array of identical microelectromechanical system (MEMS) cantilevers batch fabricated using silicon micromachining¹¹⁴. Arrays of actuated legs are also enabling the development of new centipede-inspired micro-robots¹¹⁵. While large integrations of actuators are highly desirable, it amplifies the requirements on the long term reliability of individual elements¹¹⁶. This has furthered an element-centric design strategy featuring tessellations of identical actuators.

On the other hand, designs pervasive in natural organisms demonstrate the in-

Contents of this chapter are adapted from a manuscript in preparation - S. Sundaram, M. Skouras, D. S. Kim, L. van den Heuvel, W. Matusik, “Topology-optimization and 3D-printing of multimaterial magnetic actuators and displays”, *in preparation*, May 2018. I thank M. Skouras for implementing the topology optimizer in this chapter.

creased versatility of non-uniform actuator collections. Further, these heterogeneous arrays are: (i) collectively shaped by a common functional purpose, (ii) can vary in length scales by orders of magnitude, and (iii) are individually controllable in coordination with other elements of the array. These features are prevalent in several natural systems. For example, denticle patterns attached to the epidermis and dermis of sharks together control the hydrodynamic drag^{117,118}. Wide variation in the length scales of actuators is particularly visible in comb jellies (*Ctenophora*) where cilia differing in length by two orders of magnitude (short cilia 10 - 15 μm ; long cilia >1000 μm) together play a role in synchronized beating for efficient propulsion¹¹⁹. Active control of individual actuators is, for instance, also seen in centipedes and other arthropods that generate coordinated leg movements across an array¹²⁰⁻¹²². Overall, replicating these high-dimensional actuators presents many challenges due to the design complexity, along with competing material properties and fabrication requirements. We present a strategy to realize high-dimensional actuators by combining an automated design-generation technique with a multimaterial additive manufacturing process, and this is the main contribution of this chapter.

Recently, shape optimization has been used for achieving temporal shape transformation using anisotropic swelling of a single composite material⁹⁰ and controllable magnetization profiles¹²³. Prior works deal with shape optimization for a single objective function. Despite this progress, automated design and fabrication of multimaterial structures with high dimensionality still remains a challenge. Topology optimization driven multimaterial additive manufacturing has a transformative potential in areas ranging from structural design¹²⁴ and actuator design¹²⁵ to tissue engineering¹²⁶. Custom material choices further enhance the potential of these techniques.

To build on the actuators described in the previous chapter, here we combine a custom multimaterial drop-on-demand 3D-printing process with multiobjective topology optimization to fabricate high-dimensional actuator designs generated from functional objectives (Fig. 7-1).

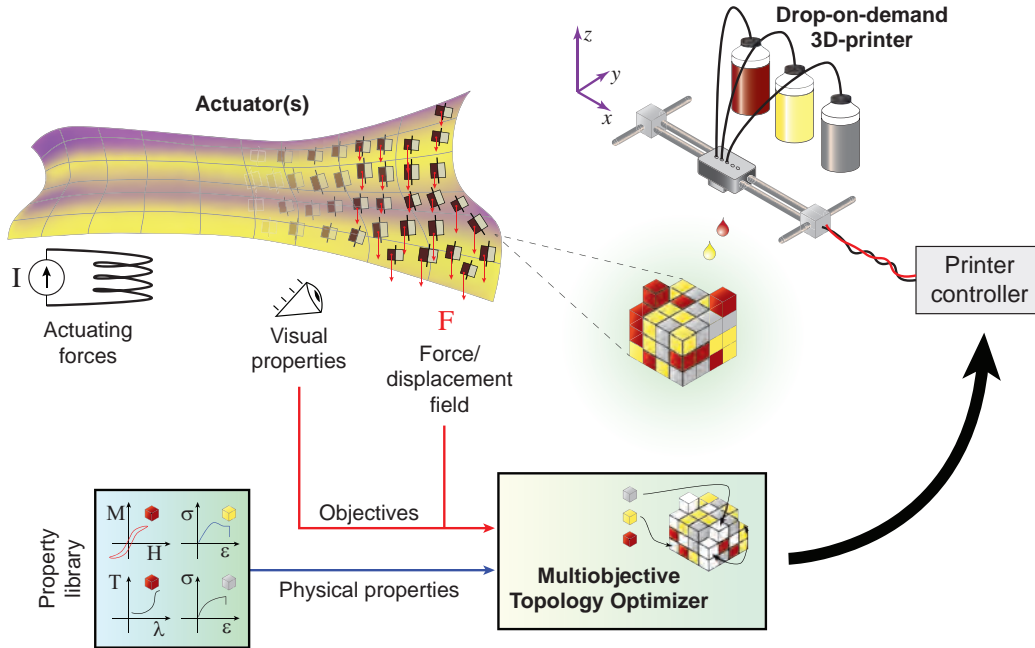


Figure 7-1: **Topology optimization for function driven actuator fabrication.** The structure of individual actuators (or the arrangement of multiple actuators) is optimized using a multi-objective topology optimization process. The optimization uses the bulk physical properties of the individual materials and the functional objectives as inputs. The generated optimized voxel-based representation of the structure is used by the printer in order to fabricate the structure using a drop-on-demand inkjet printing process. This allows high-dimensional designs to be automatically generated and fabricated with minimal human intervention. A rigid acrylate polymer (RIG), an elastic acrylate polymer (ELA) and a magnetic nanoparticle (Fe_3O_4)/polymer composite (MPC) are the main materials used, as in the previous chapter. The contrast in the optical, mechanical and magnetic properties is used to simultaneously optimize the visual appearance and the actuating forces while generating the voxel-level design

7.1 Multi-objective topology optimization

We choose an actuator design problem with more than 10^6 cells (here each cell is $3 \times 3 \times 1$ voxels in size) whose material assignments are computationally generated using topology optimization. Specifically, we fabricate an actuator that deflects and changes its appearance in the presence of a controlled magnetic field. The basic actuator unit is a single panel actuator (described in the previous chapter, Fig. 6-3A), supported by two ELA hinges, that is divided into a hexahedral lattice of cells whose individual material assignments are optimized by simulated annealing. The result is an actuator that can change its appearance to various unrelated images at

specific tilt angles (or torques). The multiple objectives here can be considered as a series of image and torque pairs. The general actuator architecture, inspired in part by multilayer tensor displays¹²⁷, is also indirectly motivated by the multilayer nature of metachrosis used by cuttlefish for camouflage⁶.

For each panel, our topology optimization component takes as input, n grayscale images \tilde{I}^i , $i = 1..n$, represented as arrays of pixel intensities, n target angles for the panels corresponding to the desired tilting angles and n distances d_i corresponding to the distances between the panel array and the permanent magnet at which the images should be revealed. The material distribution is generated at the individual cell level as the output, relying on the contrast in the optical and magnetic properties of RIG and MPC. Material assignments for each cell are made at a cell resolution of $3 \times 3 \times 1$ voxels here, i.e. $101.5 \mu m \times 101.2 \mu m \times 6.4 \mu m$.

We represent the material distribution as an indicator function χ_j that describes whether a cell at location j in the panel contains MPC or not. The appearance of a given material distribution and at a given angle is computed by ray tracing from the center of each pixel, i.e. tracing the paths of an array of light rays through the different voxels in the panel (see Fig. 7-2A). Here, we assume a diffuse light source illuminating the panels from below and assume that reflection and scattering are negligible. The observer is assumed to be looking at the panel from a sufficiently large distance above the panel. Letting c_{RIG} and c_{MPC} denote the light transmittances of RIG and MPC, the intensity I_k of a pixel k corresponding to a single ray can be written as

$$I_k = c_{RIG}^{d_{RIG}} \cdot c_{MPC}^{d_{MPC}}, \quad (7.1)$$

where d_{RIG} and d_{MPC} are the total distances traversed by the ray through RIG and MPC respectively. We use measured values of $c_{RIG} \approx 1$ and $c_{MPC} = 0.58$ for the transmittance (see Fig. 6-1). The transmittance through 5 layers of MPC, i.e. 3 % of the total thickness of the panels that we optimized in practice, is visually indistinguishable from that of a fully opaque material. Thus, to overcome the limited intensity resolution that can be achieved with MPC, we use half-toning and rely on

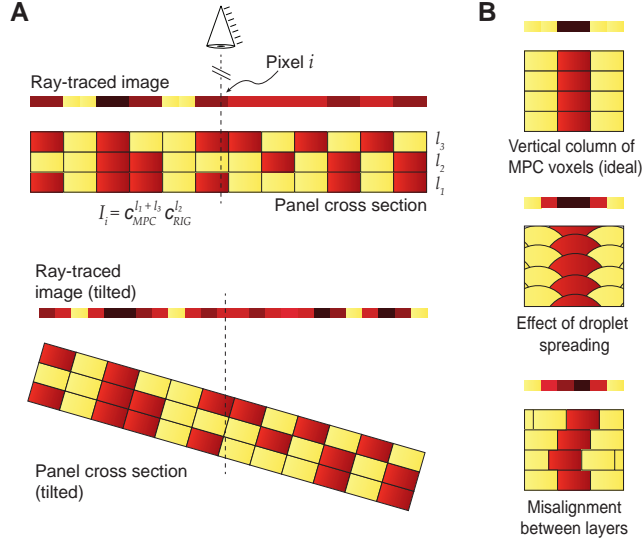


Figure 7-2: **Panel appearance computation.** **A.** The appearance of the panel as viewed from above is computed by shooting vertical rays through the panel. By computing the total distances traversed by each ray through each material, the ray-traced images can be obtained. Here three layers each filled with RIG and MPC are shown. Multiple images can be encoded in the volume based on the desired viewing angles. This can be seen in different ray-traced images obtained from a single structure with varying tilting angles. While not explicitly shown here, the volumetric positions of the MPC cells also define the torque in response to a magnetic field. **B.** A vertical column of MPC voxels (top) is widened in practice due to droplet spreading (middle) or slight misalignment in the positions of the drops in consecutive layers (bottom).

the ability of the human eye to fuse dotted patterns into continuous tones. We model this by blurring the ray-traced images $I^i(\chi)$ with a 5×5 pixel Gaussian convolution kernel p before comparing them to the input target images. In practice, as shown in Fig. 7-2B, the dot gain due to droplet spreading or misalignment plays a critical role in the overall appearance. We account for this by correcting the estimated fraction of the materials in each cell prior to ray-tracing by convolving the binary material assignment χ_j with a 3×3 kernel (experimental dot gain measurement samples are shown in Fig. 7-3 and modeling details are in the experimental methods section later).

The distribution of the MPC cells inside the panel not only affects its optical properties but also its mechanical behavior under the external magnetic field. More specifically, each MPC cell contributes to the net torque generated, τ^i , for a given distance d_i (between the panel and the magnet) depending on the position of the cell

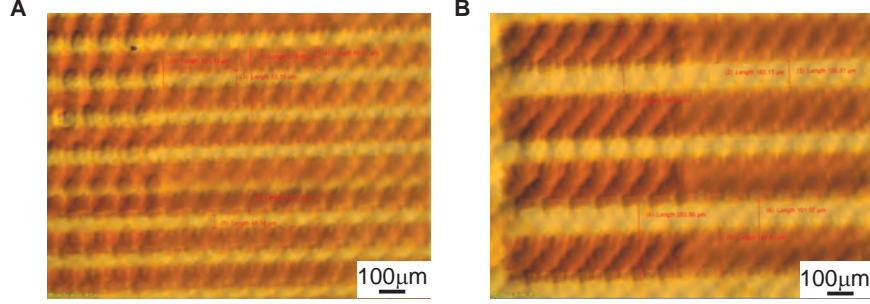


Figure 7-3: **Dot gain images.** **A.** 2-voxel wide stripes. **B.** 4-voxel wide stripes. Dark stripes are the cured MPC ink and the lighter stripes are the cured RIG ink.

in the panel. Assuming for now that each lateral ELA hinge connecting the panel to the rigid frame can be modeled as a torsion spring with torsion stiffness κ , the tilting angle assumed by the panel in its equilibrium state can be written as

$$\theta^i = \frac{\tau^i}{2\kappa}. \quad (7.2)$$

Controlling the torsion bars' stiffness by changing the geometry of the hinges is not sufficient since we want to control various tilting angles simultaneously. Therefore, we fix the dimensions of the hinges and precompute target torques $\tilde{\tau}^i$ to be exerted on the axis of the panel to make it rotate as desired. We then add hard constraints to the optimization that force the torques τ^i corresponding to the distribution χ to match these precomputed torques $\tilde{\tau}^i$. In practice, to account for the nonlinear behavior of the soft ELA hinges, the tilting angle corresponding to a given torque is computed using a finite element method that simulates the deformation of the hinges (soft-joint finite element solver is described in the experimental methods section). The target torques $\tilde{\tau}^i$ are then obtained by using a bisection method. Our original material distribution problem can then be cast as

$$\begin{aligned} \min_{\chi} E(\chi) &= \sum_i^n \|p * I^i(\chi) - \tilde{I}^i\|_4^4 \\ \text{s.t. } \tau^i - \tilde{\tau}^i &= 0, \forall i \in 1..n, \end{aligned} \quad (7.3)$$

where $*$ denotes the convolution operator. We use the L_4 norm, motivated by the fact

that it allows more uniform distribution of the error over entire images compared to norms with a smaller power. Inspired by stochastic halftoning techniques^{128,129}, we solve problem (7.3) using a simulated annealing (SA) procedure¹³⁰ augmented with a non-smooth penalty term, which, unlike quadratic penalty functions, allows for strict satisfaction of the constraints¹³¹. For our specific problem we write this additional term as

$$c(\chi) = \sum_i^n \max(0, \|\tau^i(\chi) - \tilde{\tau}^i\|_1 - \epsilon) \quad (7.4)$$

and use $\epsilon = 10^{-7}$ MPa to account for small rounding errors when evaluating the torques. The augmented objective \mathcal{L} is then expressed as

$$\mathcal{L}(\chi, T) = E(\chi) + \frac{1}{T}c(\chi), \quad (7.5)$$

where T is the simulated annealing temperature. We initialize χ with a 0-valued distribution. At each iteration of the algorithm, a candidate distribution is generated by changing the material assignment of two cells that are randomly selected. We accept the new distribution if it either lowers the objective value or if it raises it with a probability equal to $e^{(\mathcal{L}(\chi_{t-1}, T) - \mathcal{L}(\chi_t, T))/T}$, where $\mathcal{L}(\chi_{t-1}, T)$ and $\mathcal{L}(\chi_t, T)$ are the previous and current objective values and T is the current simulation temperature. This prevents the algorithm from getting trapped in local minima while simultaneously improving the exploration of the entire design space. For our final example, we use 10^8 steps and a linear cooling schedule. Contrary to gradient-based methods commonly used in topology optimization¹³², our SA procedure does not require a linear system to be solved at every step and can effectively cope with the high number of variables of our problem (one per panel voxel for a total of 10^6 cells). The large number of steps required to approximate a global optimum, typical of SA algorithms, is largely counterbalanced by the fast evaluation of the function (7.5), which, in practice, can be effectively computed by noting that a change in a voxel material only impacts a few pixels in the ray-traced images.

7.2 Printed topology-optimized actuators

We applied this methodology for the design and optimization of two different structures, the results of which can be directly fabricated using our printer using materials, designs and techniques discussed in the previous chapter. The first example consists of a single rotating panel which reveals two different images; one in the rest state and the other at a tilting angle of 30° when placed 1 cm from the permanent magnet. The images correspond to grayscale 186×186 pixel versions of the two paintings *Self-Portrait with Grey Felt Hat* by Van Gogh and *The Scream* by Munch, whose pixel intensities were linearly rescaled to map the range from 0.2 to 0.8. Assignments for the materials are considered at a resolution of $101.5 \mu\text{m} \times 101.2 \mu\text{m} \times 6.4 \mu\text{m}$ for the panel with external dimensions $18.89 \text{ mm} \times 18.83 \text{ mm} \times 1.025 \text{ mm}$. As shown in Fig. 7-4, the panel rotates under the applied external magnetic field and displays images that are in good agreement with simulation. The results are shown past the 30° tilt angle; the panel appears narrower in width on tilting. Due to the limit set by the tilting angle, ghosting in areas corresponding to very different intensities in the two target images is visible in the results of the optimization, and replicated in the prints. This effect is expected and can be reduced by decreasing the dynamic range of the input images a priori.

We characterized the forces generated by the optimized actuator (Fig. 7-5) A. The typical blocking force generated by the actuator when the magnet is held 1 cm away is $100 \mu\text{N}$. The blocking force was measured using the same polyimide cantilevers and the permanent magnet described in the previous chapter. The measured angular deflection of the actuator is shown as a function of the magnetic field in Fig. 7-5B. There appears to be small amount of hysteresis depending on the whether the magnet is brought closer or taken further away. This is because the angular deflection itself also has an effect on the actual magnetic field experienced by the panel. In general, as the panel tilts more, it is brought closer to the magnet and up until ~ 1 cm, this results in an increase in the magnetic field. This is more prominent in large size actuators ($l_p/2 \geq \sim 1$ cm). Long term performance of these large actuators was evaluated with

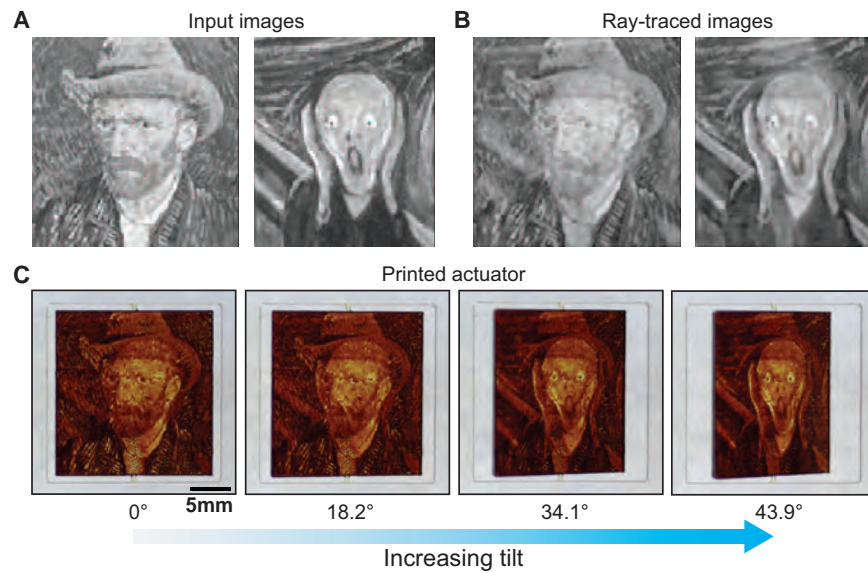


Figure 7-4: **Panel optimization for both optical and mechanical properties.** **A.** Given a pair of target grayscale images corresponding to desired top views of the panel array at two different tilting angles (here, 0° and 30°), our topology optimization framework optimizes the distribution of the RIG and MPC in the panels such that they tilt to the desired angles and their appearances match the target images. **B.** Optimized panel appearances as computed by our ray-tracer. **C.** Photographs of the 3D-printed topology optimized sample showing the gradual transition from the “Van Gogh” portrait to the “Scream” image with increasing tilt angle.

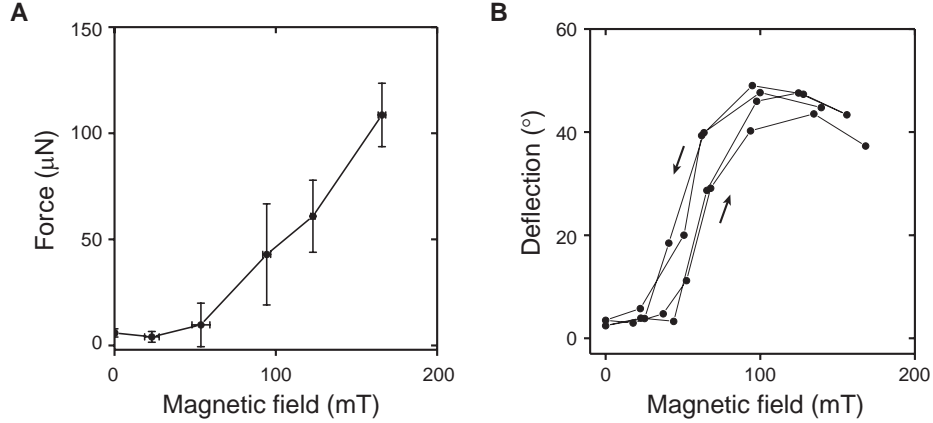


Figure 7-5: **Force and deflection measurement of the topology optimized actuator.** **A.** Measured blocking force of the van Gogh actuator in the presence of a magnetic field. The field here was generated using the 2" \times 2" \times 0.5" magnet described in the previous chapter. **B.** Measured angular deflection as a function of magnetic field. Note that our actuator exhibits a small amount of hysteresis since there are two stable positions depending on the direction of sweep for this particular magnetic field profile. The magnetic field was varied by changing the distance between the magnet and the actuator (Fig. 6-8C).

an actuator of the same size as the van Gogh actuator but made of the general design in Fig. 6-7A. This was used to test the reliability of the ELA hinges. It is seen from Fig. 7-6 that there is little to no change in performance after 1000 cycles at 0.56 Hz. The setup used to perform long term cycling is identical to the setup in the previous chapter.

The demonstrated scheme can be easily extended to larger arrays and different images. We demonstrate this with a second example, featuring a 3 \times 3 panel array with external dimension 30 mm \times 30 mm \times 1.025 mm, which is optimized to replicate two textures (grass and stones) at 0° and 30° respectively (see Fig. 7-7). When the panels are made small, the fraction of MPC required to rotate the panels to the desired angles is significant. This translates into a globally darker area on one half of each panel. Overall, the actuators generated by topology optimization demonstrate the ability of our overall scheme in optimizing complex actuators and its enabling potential in the use of magnetic soft actuators for camouflage applications.

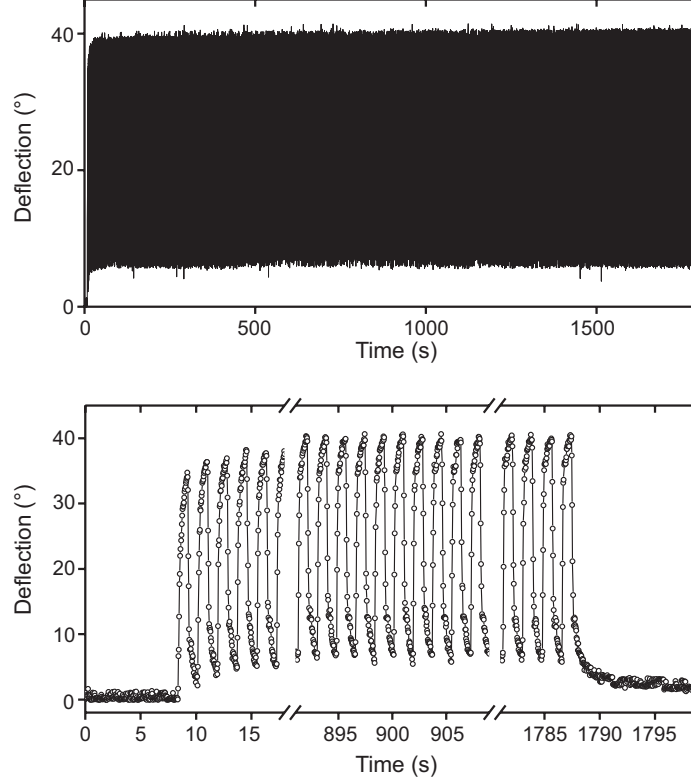


Figure 7-6: **Long term cycling test of $l_p \approx 19$ mm actuators.** The first plot shows the measured angular deflection of an actuator identical in dimensions to the van Gogh actuator. The actual design used is based on the simple actuator design in Fig. 6-7A. The maximum and minimum deflections remain stable over the 1000 cycles. The second plot shows a few cycles at the start and end. The measurement setup is identical to the description in the previous chapter.

7.3 Experimental methods

Dot gain measurements and simulation details: Dot gain measurements were performed by 3D-printing two striped-pattern prints (2 voxel wide and 4 voxel wide stripes) of the MPC and the rigid polymer ink. Dot gain was computed by measuring the actual width with respect to the expected design width. Samples were imaged using an optical microscope SZ61 (Olympus Corp. Tokyo, Japan) fitted with the SC30 digital camera (Olympus Corp. Tokyo, Japan). The widths of the stripes of both prints were measured using the Stream start software (Olympus Corp., Japan). The width of the MPC traces and the rigid ink of the 2-voxel wide stripes were $\sim 90 \mu\text{m}$ and $\sim 50 \mu\text{m}$ respectively. The corresponding widths for the 4-voxel wide

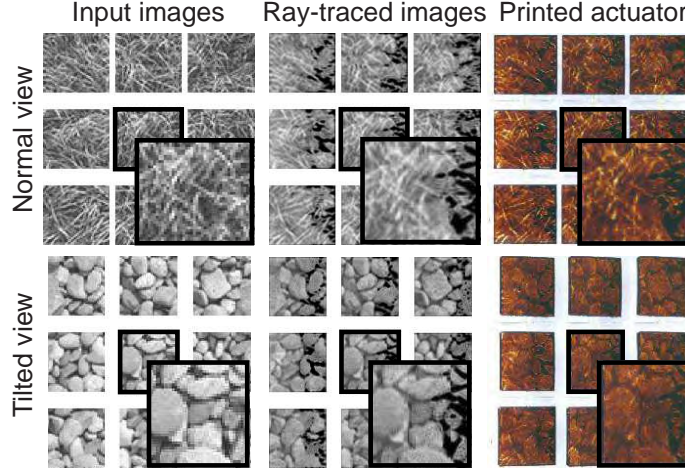


Figure 7-7: **Topology optimized actuator array - grass and stones.** Another example of topology optimized actuators showing the transition from images of grass to stones when a magnetic field is applied. The topology optimization strategy distributes the materials such that the panels tilt to the desired angles and force the appearance to match the target images. Photographs of the 3D-printed panels under no external magnetic field (top) and under an external magnetic field (bottom) are shown on the right.

stripes were $\sim 180 \mu\text{m}$ and $\sim 100 \mu\text{m}$ respectively (Fig. 7-3). The dot gain of the droplets are typically symmetric in the in-plane directions, and are assumed to be so here.

So in practice, a column of voxels containing MPC appears, on average, $30 \mu\text{m}$ wider than the width of the original droplets deposited by the printer. Dot gain is typically due to drop spreading and slight misalignment in the positions of the drops of consecutive layers. To account for these effects, we correct the estimated fraction, or presence probability, of magnetic ink in each voxel prior to ray-tracing the light. This is performed layer-by-layer by convolving the original binary material distribution with a 3×3 kernel q of the form

$$q = \frac{u}{\|u\|} \frac{v^T}{\|v\|}, \quad u^T = [s_x r_x s_x], \quad v^T = [s_y r_y s_y], \quad (7.6)$$

where $s_i = 15 \mu\text{m}$, for $i = \{x, y\}$, is the measured lateral spread of the drops in the in-plane directions and r_x and r_y are the voxel resolution along x and y respectively. The filtered material ratios are used to scale the individual distance contributions of

voxels in the calculation of the total distances d_{RG} and d_{MPC} traversed by the rays.

Soft-joint simulation: Each joint connecting the panels to the frame is modeled as a hexahedral lattice with 16^3 elements and simulated with a finite element method using linear basis functions and 8 quadrature points per element. For the ELA material, we use a Neo Hookean material model with energy density $W = \frac{\mu}{2}(I_1 - 3 - 2\ln(J)) + \frac{\kappa}{2}(\ln(J))^2$, where I_1 and J are respectively the first invariant of the right Cauchy-Green deformation tensor and the determinant of the deformation gradient and μ and κ correspond to the shear modulus and the bulk modulus of the material. The panels and the frame are treated as rigid bodies. The forces acting on the panels are computed on a voxelized representation of the panel geometry. We consider both gravitational forces acting on all the voxels of the panels, and magnetic forces due to the external magnetic field acting on the MPC cells. Each of these voxels is modeled as a magnetic dipole with moment \mathbf{m}_i located at the center \mathbf{c}_i of the voxel and aligned with the external magnetic field. The force \mathbf{F}_i acting on the magnetized voxel is thus described by $\mathbf{F}_i = \nabla(\mathbf{m}_i \cdot \mathbf{B})$. We model the magnetization of the MPC cell using the hyperbolic tangent function as $M(\mathbf{H}) = \pm 5.67 \tanh(2.8 \times 10^{-2} \sqrt{\|\mathbf{H}\|_2})$, with \mathbf{H} expressed in $[Oe]$ (see magnetization curves in the previous chapter). The magnitude m_i of the moment \mathbf{m}_i is then approximated by $m_i(\mathbf{c}_i) = M(\mathbf{H}(\mathbf{c}_i))\rho_{MPC}dV$, where $\rho_{MPC} \approx 1.2 \text{ g/cm}^3$ denotes the density of the cured MPC material and dV corresponds to the volume of an individual voxel. Note that the moment generated by an MPC cell is not constant but depends on the current location of the voxel center which is affected by the rotation of the panel.

Part IV

Tactile Skins for Understanding Human Grasp

Chapter 8

Tactile sensor arrays & gloves

Humans perform dexterous tasks every day that are extremely challenging for robots to replicate. Tactile feedback is a key enabler for the this, i.e. the primate grasp. In contrast, modern day robots lack the dense network of tactile information we take for granted; in that sense robots are tactile blind. The human hand consists of primarily 4 types of mechanoreceptors⁷ that enable us to grasp objects with the right amount of force: Slow adapting (SA-I), SA-II that sense static signals and fast adapting FA-I and FA-II receptors that respond to vibrations¹³³. Using these inputs, we learn a sensorimotor control policy to generate actions for a goal, like grasping a specific object¹³⁴. Given the importance of control policies in robotics, creating an analogue of the natural tactile system has been of extreme interest for decades. The inability to replicate the natural sensor network in the primate hand also restricts our fundamental understanding of simple actions like the grasp.

The challenges in making a sensor laden artificial hand are large. The hand consists of a multitude of sensors including temperature sensors and pain receptors which are neatly integrated into the cutaneous and subcutaneous regions of the skin. The skin itself is a complex mechanical matrix that regulates our interactions with the outside world - it is stretchable, has a dynamic stiffness¹³⁵, is self-healing and extremely robust. Interest in the field of electronic skins has mainly been driven by this broad goal. Most recent works demonstrate a rectangular grid of sensing elements both active and passively addressed. Some of the most recent works are:

a microstructured rubber based tactile sensory array⁴⁰, a nanowire active-matrix based macroscale skin¹³⁶, interlocking nanofiber based sensor array¹³⁷, electronic skin with a focus on the user interface¹³⁸. The focus shifted to making flexible active circuits that can route signals from the sensor array^{45,139} rather than focusing only on the active pressure sensitive material. More recently, bending insensitive arrays¹⁴⁰, and multimodal sensor arrays¹⁴¹ (force and temperature) have been demonstrated. Most of these works demonstrate sensor arrays with ~ 100 s of elements. A more comprehensive review of this vast field is in a recent review article¹³³. In spite of the great progress made so far in making planar, stretchable tactile arrays, translating this to an arbitrary curved surface (e.g. non flat-foldable) is still challenging. Works demonstrating tactile gloves are even more limited, and most recent tactile gloves only consist of 10s of elements. Two recent demonstrations that focus heavily on translating these tactile sensors to a stretchable and robust glove, contain 54 and 10 elements respectively^{142,143}. This limited density poses a couple challenges: (i) the resolution of tactile signatures that can be recorded is poor, and (ii) recent machine learning algorithms have mostly been tested on inputs that have a minimum of ~ 1000 dimensions (or a 32×32 array).

The main objective here is to fabricate a sensor array (with 32×32 tactile elements), that can be attached to a glove. The components used in making the array are chosen from readily available materials and the sensor array can be rapidly fabricated. A readout circuit is used to acquire the sensor readings. First prototypes of the glove shell (that can be attached to a glove) are also demonstrated here. A short summary of the next steps towards dataset acquisition and processing is included in the end of this chapter.

8.1 Fabrication of a regular array

The tactile sensor system described here is made of piezoresistive elements in a single force sensitive film. A planar sensor array with a regular grid is used to test the general fabrication strategy, characterize the sensor and the accompanying electronics. The

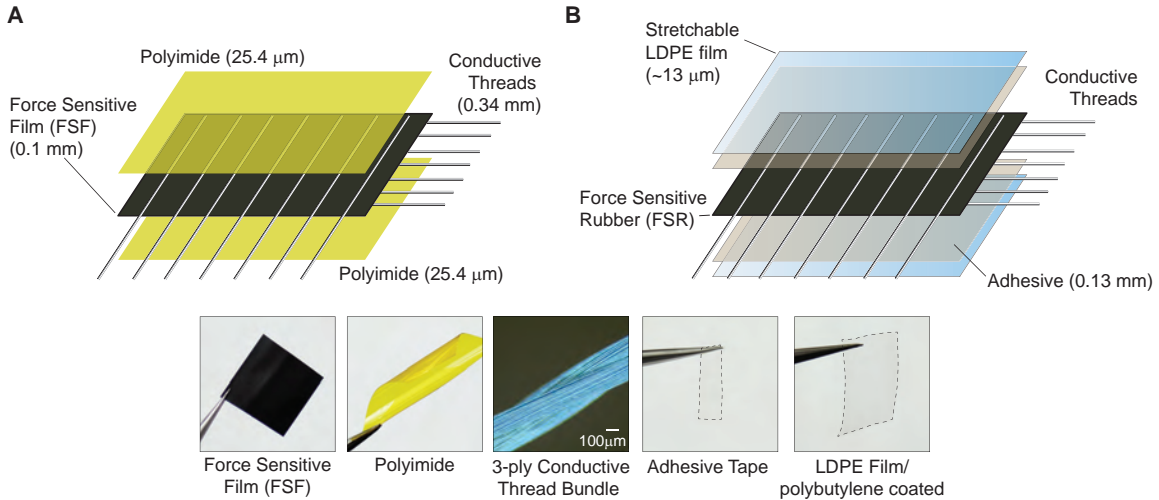


Figure 8-1: **Schematic of the tactile sensor array.** **A.** Sensor array with overlapping conductive thread electrodes on either side of a pressure sensitive film. The regions of overlap are force sensitive points. The device is insulated on each side using a polyimide film. **B.** Improved version of the device replaces the insulating polyimide film with an acrylic adhesive film that holds the conductive threads in a more tightly constrained window. Images show the individual components of the sensor array.

general architecture of the sensor array is shown in Fig. 8-1. The active pressure sensitive material is a commercially made force sensitive film (FSF) (3MTM VelostatTM electrically conductive EVA copolymer). It is conventionally used as a packaging material that is made conductive by impregnation with carbon black. The application of pressure on the film reduces the electrical resistance through its thickness. Figure 8-1A shows a planar sensor architecture with a grid of conductive thread electrodes (3-ply conductive threads ~ 0.34 mm diameter) on either side of the film. Regions of overlap between the threads on each side are the sensitive regions of the device. The electrodes are insulated with an adhesive-coated polyimide film on each side. Images of the individual components are included below the schematic. Figure 8-1B shows an improved design that restricts the movement on the electrodes. In this case, the insulation film is replaced with a thin acrylic adhesive tape (3MTM 468MP 200MP adhesive). The stretchable adhesive film holds the conductive threads in place even when bent significantly. The exposed sides of the adhesive are covered with a thin stretchable LDPE film.

The sensor is constructed by first cutting squares ($\sim 9 \text{ cm} \times 9 \text{ cm}$) from the pressure sensitive film. The electrodes are placed on to the adhesive side of the polyimide insulation. A piece of acrylic sheet is laser cut with groves to make a “needle” with 32 uniformly spaced holes (2.5 mm apart). This ensures that the conductive threads are uniformly spaced and completely aligned. The polyimide film with the conductive thread electrodes are attached on either side of pressure sensitive film. With these few steps the sensor with a uniformly spaced grid can be constructed rapidly with just a pair of scissors. Most of the results described later were obtained by constructing a 32×32 sensor array (with 1024 elements).

8.2 Sensor characterization

Several small sections ($\sim 1'' \times 1''$) were cut out from the pressure sensitive film and one conductive thread was attached on either side using a polyimide tape. This allows us to probe the properties of an individual element without any cross-talk with adjacent elements that is expected in the larger sensor array. Resistance as a function of the load is the key characteristic for this sensor. So several mechanical loading tests were performed on many identical devices using the mechanical testing system (Instron 5944, Instron, Norwood, MA). Figure 8-2A shows the main sensor characteristic as the applied force is increased to 0.5 N and then cycled back to 0 N. The resistance drops from $3.8 \text{ k}\Omega$ to $1.8 \text{ k}\Omega$, and the device shows some hysteresis between the forward and the reverse cycles (loading rate is 0.5 mm/min). The response is almost linear in the log scale as shown in the inset. Further, the resistance appears to reach a steady value beyond 0.5 N. Note that 0.5 N corresponds to 4.3 MPa (or 626.6 psi) when applied over the area defined by the diameters of the two conductive threads (0.34 mm). To test the actual working range of the sensor, a large load was applied (5 N) and the resistance change was measured (Fig. 8-2B). It can be seen that below 0.03 N, the sensor does not show any drop in resistance, and the sensor response is linear in the log scale until 0.5 N. The sensor does not fail (or punch through) at loads up to 5 N (43.2 MPa), and the resistance reaches a minimum of

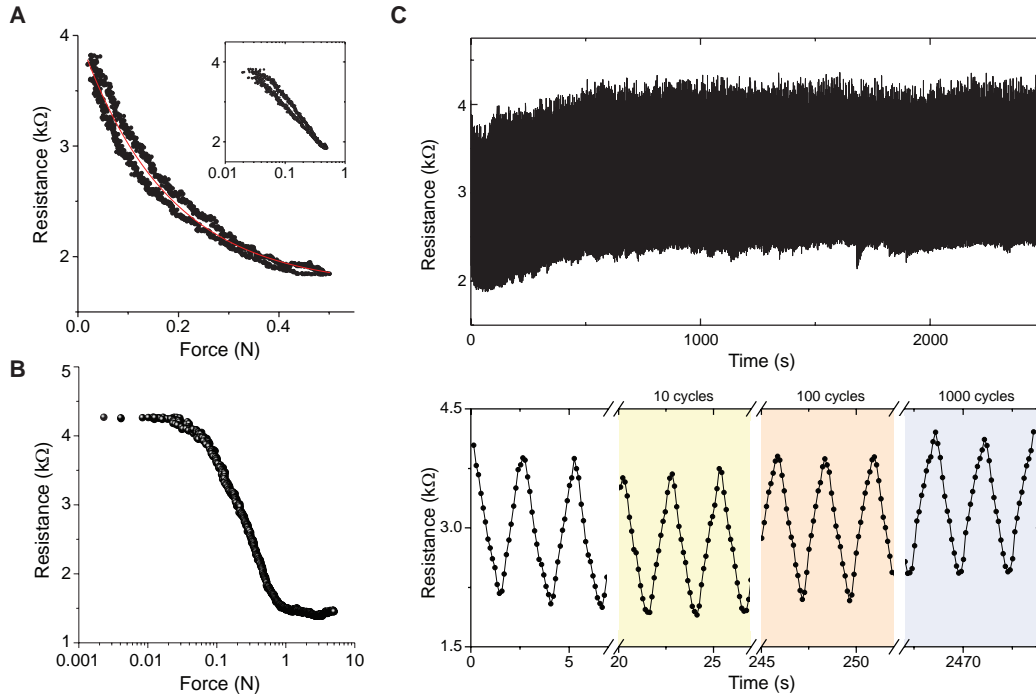


Figure 8-2: **Strain sensor characteristics and long term cycling.** **A.** Force response curve for a single element of the sensor array. The measurements were performed at a strain rate of 0.05 mm/min **B.** Resistance measurement up to a higher load (5 N) shows that the forces below 0.05 N are not picked up by the sensor, and the resistance saturates beyond 1 N. The device does not fail until 5 N of force. **C.** Long term cycling measurement shows the resistance as a function of time for 1000 cycles up to 0.5 N using a controlled strain rate (2.5 mm/min).

$\sim 1.4 \text{ k}\Omega$. The sensor elements were also cycled up to 1000 cycles and the performance is seen to reach a steady range after the initial 100 cycles. The measured resistance is shown as a function of time in Fig. 8-2C. These measurements so far represent the characteristics of a typical device, and are repeatable across a few devices. The sensor characteristics and long term measurements are shown in Fig. 8-3. It is to be noted that for the long term tests, the test were performed at a constant strain rate across all devices up to a force of 0.5 N - so the actual number of cycles vary across devices shown in Fig. 8-3B. Between 800 and 1000 cycles fit into the 2500 s measurement shown in Fig. 8-3B. Overall, the sensors show low variability. It is to be noted that some of the variation see here might be a function of the contact made by the 3-ply conductive thread bundle. Nonetheless, it might be useful to characterize this factor more precisely if the device level variation needs to be further reduced.

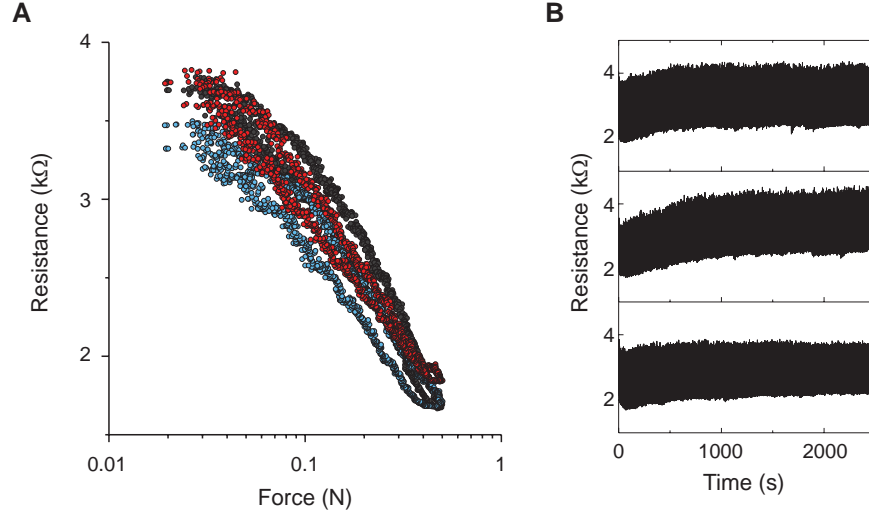


Figure 8-3: **Sensor characteristics of 3 devices.** **A.** Force response curve of 3 identical devices. **B.** Long term cycling measurement on 3 identical devices. The cycling tests were performed using a controlled strain rate up to a maximum load of 0.5 N for 1000 cycles. The exact number of cycles varies a little in these measurements shown up to 2500 s.

8.3 Sensor array and readout circuit

The passive matrix design makes the sensor design and fabrication simple, however, there is a possibility for extensive crosstalk between sensors in close proximity. This problem has been studied quite extensively¹⁴⁵, and it is possible to eliminate a majority of these effects using well designed readout schemes^{144,146}. Briefly, in the idealized representation of the sensor array in Fig. 8-4, when a single sensor is to be read, the corresponding row is set to 0 V. Every other row is connected to a reference voltage V_{ref} . The analog switch at the end of the columns connects one of the amplifier outputs to the measurement device - an analog-to-digital converter (ADC, not shown). Due to the fact that the input pins of the amplifiers are maintained at identical reference voltages, All current paths from rows connected to V_{ref} appear to be non-existent since there is no potential difference. This circuit therefore allows virtual grounding of all elements that are currently not probed and avoids electrical cross talk. The circuit in Fig. 8-4 is based on the grounding-based topology used previously¹⁴⁴. The charging resistors ($R_c = 900 \Omega$) are added here to reduce the input noise at the inverting terminal of the amplifiers. The low resistance enables the input node to charge

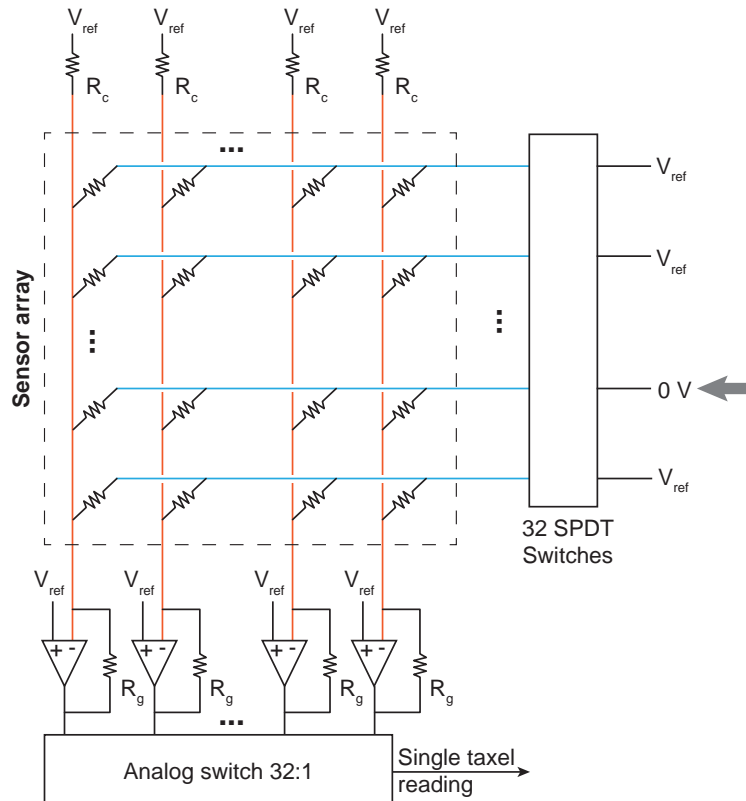


Figure 8-4: **Readout scheme for the tactile sensor array.** The readout circuit is based on a virtual grounding topology¹⁴⁴ that effectively removes electrical cross-talk from adjacent sensors. Here $R_c = 900 \Omega$ and $R_g = 1 \text{ k}\Omega$. The 32 SPDT switching array is constructed from 8 quad SPDT switches (ADG333A). The amplifiers are made using LMV324 and connected to a 32:1 analog switch ADG732. The output of the switch is connected to an analog-to-digital converter (ADC, not shown). The row and column switches are controlled by a microcontroller. At a given time, the row currently being read is grounded (indicated by an arrow).

rapidly in the presence of a large parasitic capacitance at the input. The circuit can be improved by adding buffers both to the outputs of the readout matrix amplifiers and the active switching matrix connected to the rows with the single-pole double-throw (SPDT) switches. Here, 8 quad SPDT switches (ADG333A) are used for actively switching the row voltages, along with 8 quad operational amplifiers (LMV324) and a 32:1 analog switch (ADG732). The output of the analog switch is connected to an ADC while a microcontroller is used to actively switch the rows and columns being read out. The data from the microcontroller is transmitted serially and the full array frame rate achieved with an ATmega328 is $\sim 10 \text{ Hz}$. The current limitation on the

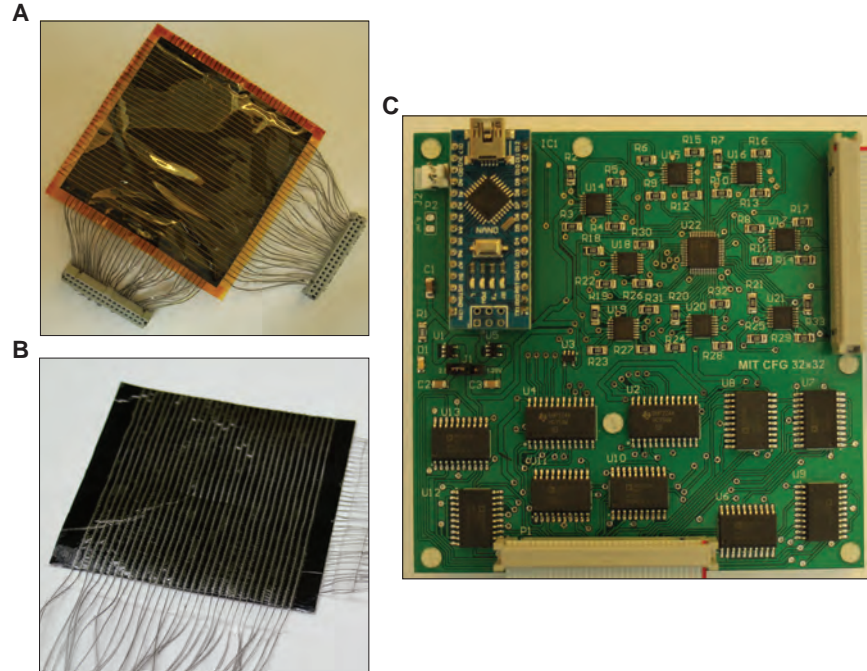


Figure 8-5: **Fabricated 32×32 sensor arrays.** **A** and **B** show fabricated sensor arrays with 1024 elements each (see Fig. 8-1A & B for designs). **C.** Printed circuit board with the readout circuit described in Fig. 8-4. The two insulation-displacement connectors (IDCs) on the right and the bottom show the connections to the sensor array.

frame rate comes from the time for serial transmission of data. This frame rate is sufficient for our task and can be improved further if needed.

The fabricated sensor arrays for the two designs in Fig. 8-1A & B are shown in Fig. 8-5A & B respectively. The spacing between the electrodes in both devices is 2.5 mm and the active sensing area is 8 cm \times 8 cm. One of the key challenges in making the devices is making the connectors and insulating the conductive threads outside the sensing area. Coating the conductive thread electrodes with a layer of polydimethylsiloxane (PDMS) and then curing it was found to be an effective way to perform this. The wires were then individually attached to an insulation-displacement connector (IDC) to form robust contacts that can be connected with the readout circuit (Fig. 8-5C) easily.

The readout circuit transmits data to the computer serially using a USB connector. We wrote a program to capture synchronized frames of video (Point Grey GS2-GE-

20S4C camera) and tactile data. This allows us to obtain visual and tactile data that are synchronized that can be used to learn relationships between objects and pressure maps. To test this scheme, we recorded video and pressure maps as 10 common daily objects were placed and moved around on the tactile array placed on the top of a flat desk. Frames from these videos are shown in Fig. 8-6. Interesting patterns appear - for e.g., the *kiwano* (horned melon) rests on only 3 sharp points while the visually similar orange has a ring-shaped contact. Another example is the milk carton which - appears to rest on a flat contact - actually experiences sufficiently larger loads at the seams of the carton. It can also be seen that single pixel resolution is available when objects like the tip of a pen are pushed against the sensor array. This preliminary dataset shows that structural features of the contact can be extracted from the sensor array quite reliably. The frame rate of the combined visual and tactile recording system is ~ 6.5 Hz.

8.4 Extensions to the sensor array

The pressure sensitive film used here is thin and flexible but is not stretchable. Therefore, the sensor array does not conform to surfaces with high curvatures nor does it stretch locally. To overcome some of these limitations, it is possible to laser-cut auxetic patterns¹⁴⁷ in the pressure sensitive film to improve its in-plane stretchability. A simple pattern is shown in Fig. 8-7A. In this case, the slender elements can be straightened and the patch effectively behaves like a negative Poisson's ratio structure that allows local areal expansion. This concept was improved to the design shown in Fig. 8-7B. Here the squares (sensing elements) rotate with respect to each other and have an effective negative Poisson's ratio. The slots allow the square to rotate while the small holes are guides for routing the conductive threads. The laser-cut pattern supports a 10×10 array of electrodes that overlap on either side of each square (Fig. 8-7C). The close up of the squares showing the conductive threads on one side is shown in Fig. 8-7D. One of the main concerns of this approach is that the heat generated during the laser cutting process would adversely affect the sensor.

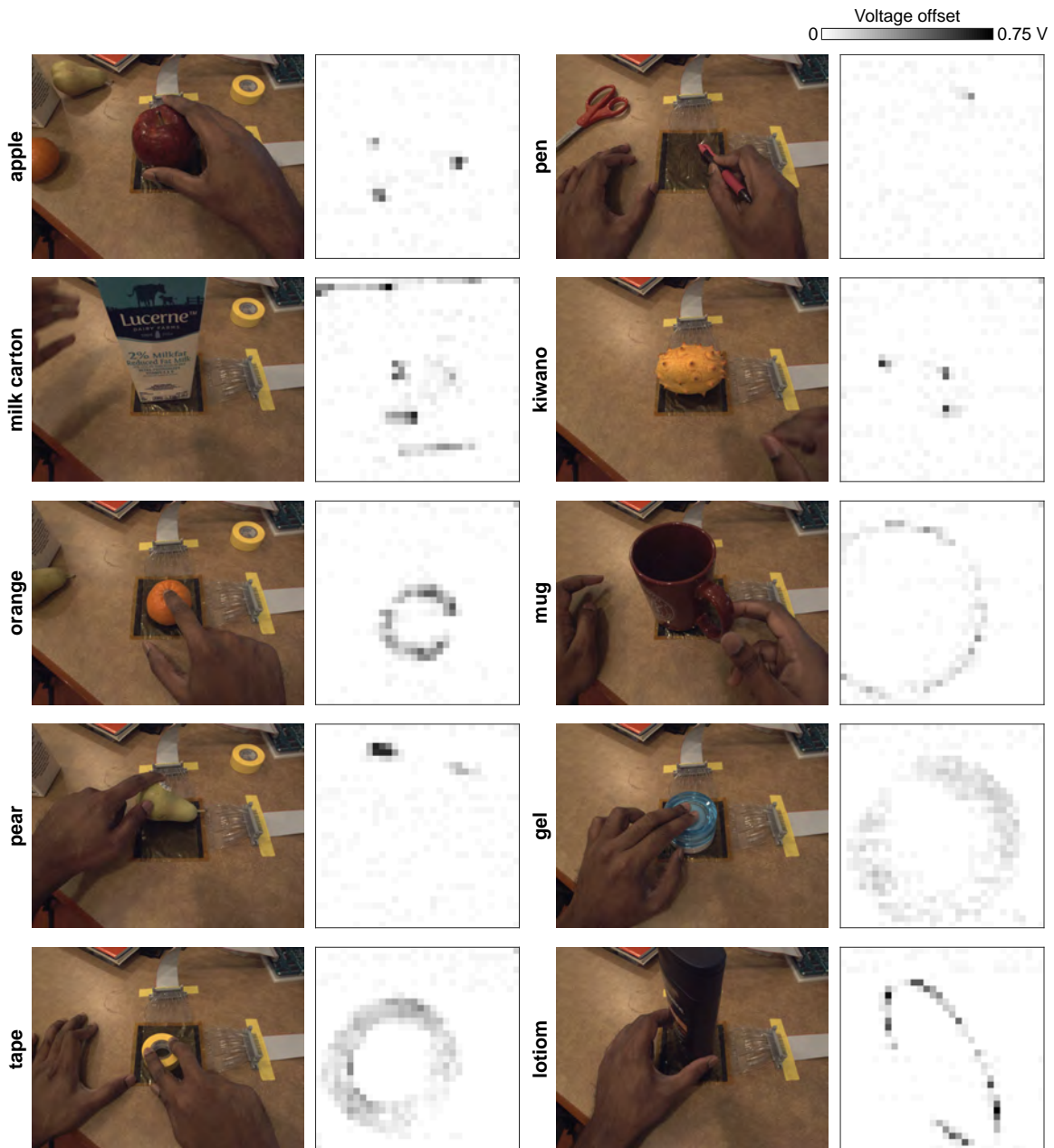


Figure 8-6: **Captured 10 object dataset of visual and tactile images.** The tactile sensor array was used along with a Point Grey GS2-GE-20S4C camera to capture videos of synchronized tactile and visual images. Photos and corresponding tactile images are shown for 10 common objects moved on the sensor array: apple, milk carton, orange, pear, tape, pen, kiwano, mug, gel and lotion.

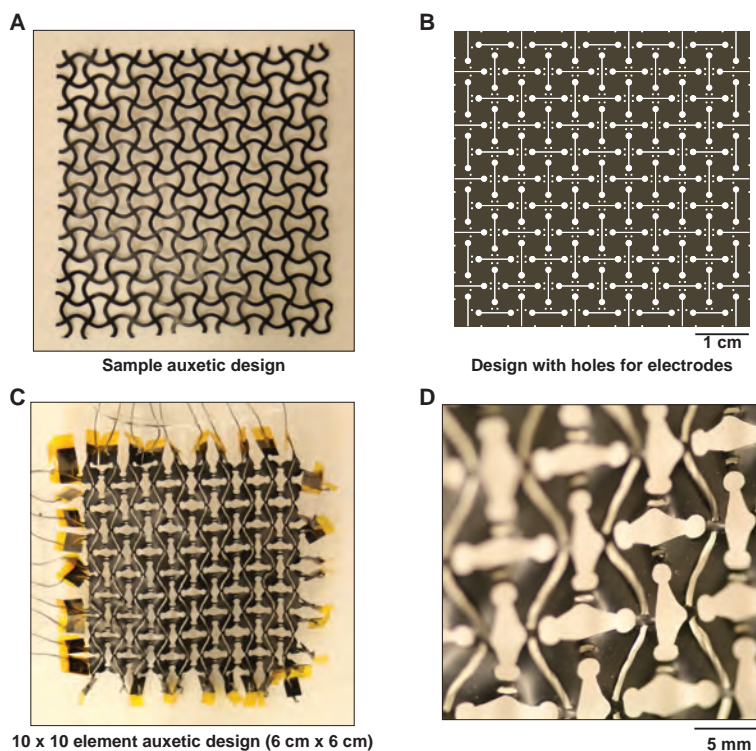


Figure 8-7: **Auxetic patterns for sensor arrays.** **A.** Example auxetic pattern laser cut onto the pressure sensitive film. **B.** Final design of the auxetic pattern contains rotating squares which are the sensor elements. Small holes cut into the pattern allow routing wires on both sides of the pattern so that they overlap with each other at the center of the square. **C.** Fabricated 10×10 sensor array that can be stretched. **D.** Close-up of the array showing individual square sensor elements and the conductive thread electrodes.

However, it was seen that the base resistance did not change, and that 5 mm squares could be cut without degrading the film. This approach enables building a stretchable array but note that cutting slots into the film comes with the compromise of reduced spatial resolution. Auxetic patterning has been used to enhance the sensitivity of the sensors themselves¹⁴⁸ but this is not explored here.

It is possible to computationally design auxetic materials to cover arbitrary surfaces¹⁴⁹, however folding the planar sensor film to the final shape is a challenge. It would be more convenient if the film can be directly thermoformed into a desired 3D surface (Velostat is sold as a film that can be thermoformed). To study the viability for this more closely, samples of the pressure sensitive film were analyzed using the differential scanning calorimeter (DSC) to understand the melting profile (Fig. 8-8).

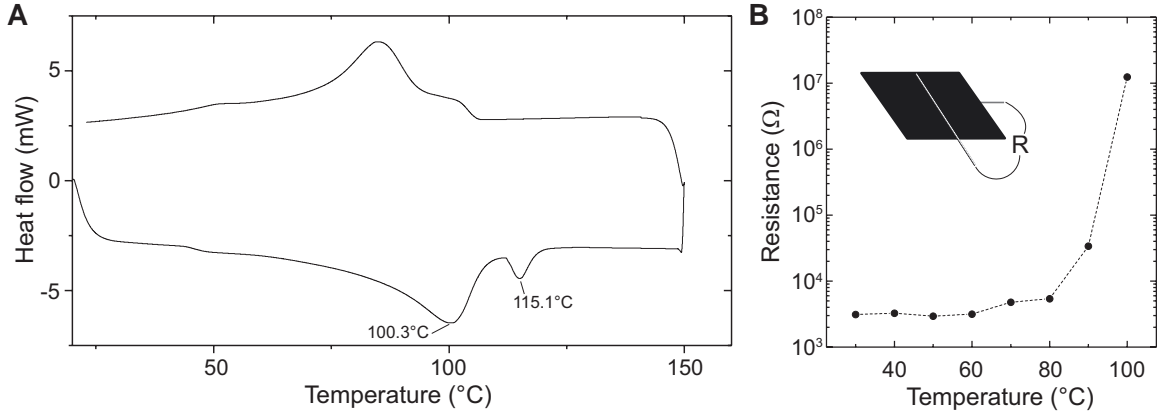


Figure 8-8: **Thermal characteristics of the pressure sensitive film.** **A.** Differential scanning calorimetry (DSC) measurements performed with a sample of the pressure sensitive film (7.9 mg). It can be seen that the film is made with a polymer blend. **B.** Measurement of resistance through the film after 10 min at a controlled temperature in a convection oven. The resistance through the film changes marginally above 60 °C, and significantly beyond 80 °C.

It can be seen that the pressure sensitive film consists of a two polymer blend (at least) with two distinct melting peaks. However, when small samples are cut and kept in a convection oven for 10 mins, the resistance through the film is affected for temperatures above 60 °C. However, the resistance increase is marginal until 80 °C. Therefore thermoforming may be possible within a small temperature range (60 °C - 80 °C). Our thermoforming attempts were not successful (resulted in films with very high resistance) since general purpose thermoforming machines, including the one we used, do not provide fine control of the thermoforming temperature.

8.5 Towards tactile gloves

The choice of materials and the fabrication methods described so far were motivated by a possible extension to a skin that can be attached to gloves. Figure 8-9A shows the receptor field on the pattern of a hand constructed from a 32×32 array of electrodes. The corresponding map on the sensor is shown on the right. To make this sensor array, the electrodes are woven into a mesh with the pressure sensitive film in between each crossing, that acts as a sensor node. Therefore, unlike the regular

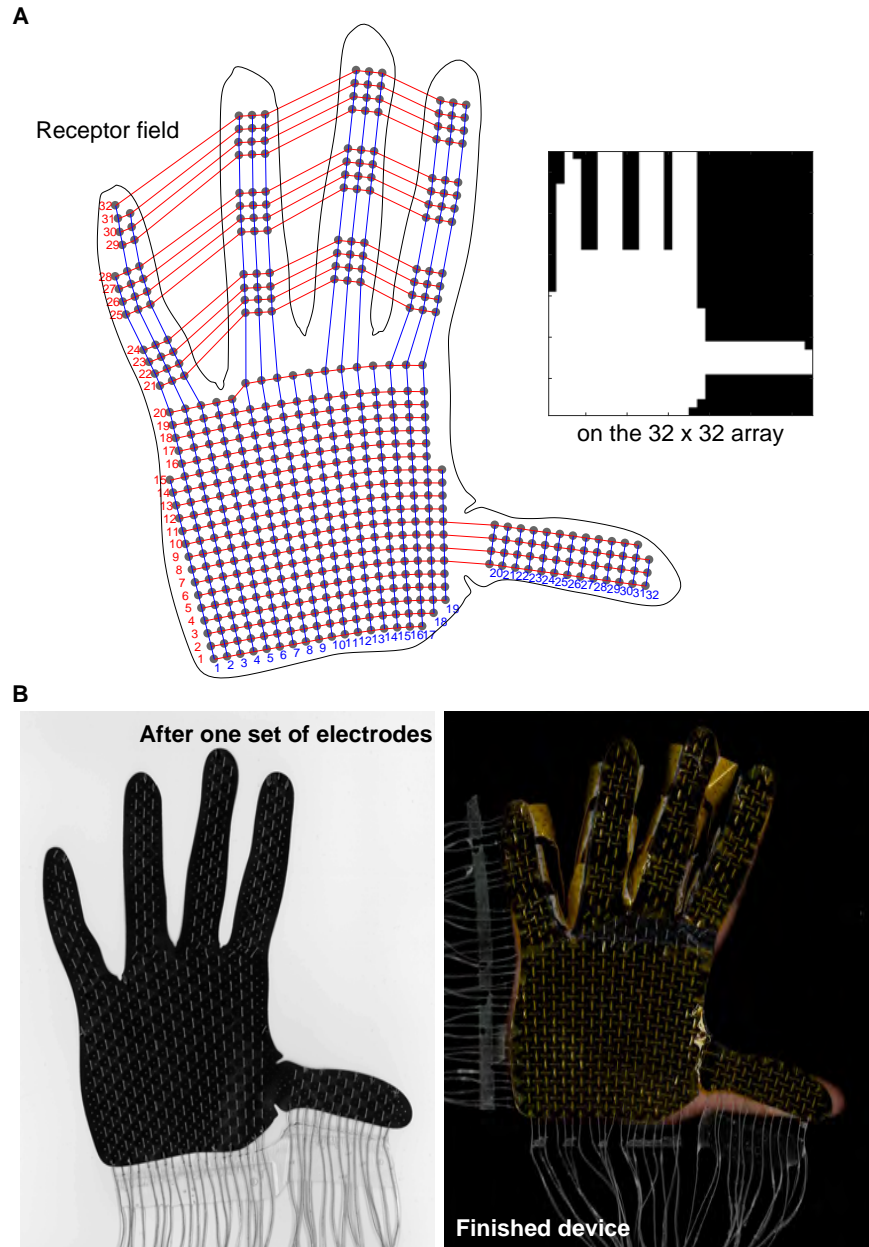


Figure 8-9: **Tactile glove.** **A.** Schematic shows the positions of the 555 sensors on the hand (receptive field). The image on the right shows the mapping of these 555 points on to the 32×32 element read out array. **B.** Fabricated sensor array with one set of electrodes (left). The image on the right shows the finished glove that can be stuck on to a standard nitrile glove. The interconnects running between the fingers are partly visible.

grid where each electrode remains on one side, here the electrodes cross over into alternate sides at regular spatial intervals. The pattern in 8-9B is laser cut along with holes that allow the conductive threads to crossover to the other side. The image shows the pattern with one set of electrodes sewn on to the glove through the laser cut pattern. The ends of the conductive threads here are insulated using PDMS as outlined earlier. Finally, the other set of orthogonal electrodes are woven into the glove and the finished device is shown in the right.

The fabrication of the glove takes more than a day currently since the threading process is done manually. Further, the interconnects between the fingers have to be implemented such that there are no short circuits and that they do not restrict the movement of the fingers themselves. One other important factor is that the glove cannot form sharp bends seen in the human skin near all the joints in the hand. Despite these current limitations, the glove enables acquiring tactile images while grasping objects. Next steps here are to evaluate the glove and capture datasets similar to those in Fig. 8-6.

8.6 Future work

The number of sensors in the tactile glove here approaches the minimum number of pixels required to understand images, identity and scenes^{150,151}. We therefore think this is a good starting point to acquire larger datasets of visual images and corresponding tactile images as objects are grasped. Figure 8-10A shows a scheme where tactile images and optical images can be coupled along with geometry information or hand pose to learn a common multimodal representation¹⁵²⁻¹⁵⁵. This will allow one to relate information from the appearance of an object to the corresponding grasp. Sensorimotor control policies related to such tasks are currently hard for a robot to learn today. At a more basic level, tactile images allow one to infer additional information in the presence of occlusions in a visual image, or detect and localize physical contacts. A broader objective is to learn the grasp signature of a set of objects using unsupervised learning based approaches and clustering techniques - to group objects

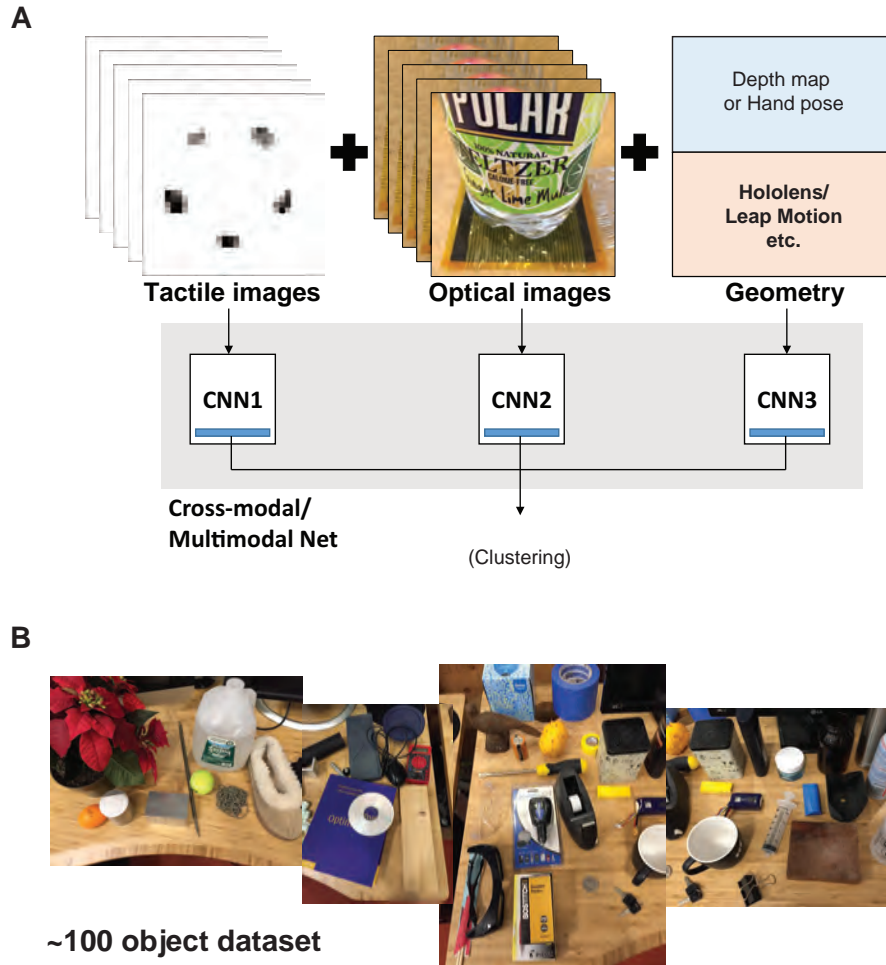


Figure 8-10: **Future work.** **A.** A general strategy to learn multimodal representation of visual images, tactile images and geometry information. **B.** Samples from our 100 object dataset that will be used for acquiring tactile images from the glove.

based on the typical tactile signatures associated with objects. We are currently working on collecting 100 common objects that humans can hold and interact with using a diverse set of grasps (some objects are shown in Fig. 8-10B) for our dataset.

Chapter 9

Conclusions

Overall, this thesis presents a full toolkit consisting of new materials, design & fabrication strategies, and device architectures to unify form and function together. The assembly of mass manufactured parts used in conventional fabrication is a limiting strategy - for instance, at the mesoscale scale. The drawbacks of mass manufacturing and assembly are further accentuated when customization of each part is required. 3D-printing strategies and associated methods we described here allow us overcome some of the challenges of an assembly-centric approach, and enable the integration of several functions (sensors, processors and actuators) inside a printed object without the need for external assembly. This is possible both due to the freedom in material choices (solids, liquids and thin-films) but also in the complexity of designs that can be fabricated. The ability to encapsulate liquids inside our printed parts over long periods of time along with the freedom in controlling material interfaces (geometry, texture, surface energies etc.) are key enabling factors. Our additive manufacturing approach also opens up the possibility for achieving complex, evolving form by using self-folding strategies using the residual stress within a printed part. The high-dimensional design space available in a 3D-printing process offers new possibilities in fabrication - our work on printed “appearance-changing” actuators highlights the role of automated design in this complex design space.

9.1 Future work

The material assembly strategies outlined in the thesis enable a host a new devices that are yet to be explored. It is when these new devices are integrated together to form fully autonomous and self-sufficient systems that the true potential of our techniques emerge. As we achieve the ability to tailor material interfaces and functions inside a complex, freeform structure, we start blurring the lines between materials and machines - the idea of autonomous composites is built on this foundation. Printed actuators with very high power density, and long-term batteries are key fundamental blocks that are required to enable the level of self-sufficiency we see in any natural organism⁹.

- In the first part of the thesis, we demonstrated electrical elements printed on top of enclosed microchannels containing a fluid. The channel profile can be varied easily and so can the materials exposed in the channel. Many layers of electronics and microchannels can be stacked on top of each other, or be fully interconnected. These architectures have been traditionally hard to fabricate. One can now envision the use of a similar system with microchannels and embedded electrodes for bio-sensing or for monitoring cellular (epithelial/endothelial) barriers¹⁵⁶.
- The residual stress-based folding system we described in part II provides a new approach to spontaneous folding. However, the process of polymer swelling it is based on has a wider applicability, especially in reducing the typical warping of UV-cured 3D-printed parts. This shifts the focus onto the material formulation and the general design of the curing process parameters. Actively controlling polymer swelling during the printing process provides a new mode of control that was previously not used.
- The automated design and fabrication system which was covered in part III of the thesis is still nascent. It has wide applicability in areas ranging from structural design¹²⁴ to tissue engineering¹²⁶. While optimization algorithms

have existed for a while, merging them with fabrication techniques uniquely enables the actual realization of these parts. The automated design and fabrication strategy is an essential component for a “closed-loop fabrication and evaluation plan” where large number of parts with different designs can be sampled, fabricated and tested. This opens up a new avenue for fabrication-aware optimization.

- Part IV of the thesis provides a rapidly scalable tactile strategy towards learning grasp. The approach can also be used for robot surfaces. The sensor is constructed using inexpensive materials but this does not compromise its repeatability since the raw materials are made in a large commercial process with tight tolerances. We expect this approach to democratize or provide easy access to tactile skins at multiple length scales. Further, the easy availability of these materials will hopefully make the acquired datasets easy to replicate and use.

In summary, the ideas presented in this thesis allow us to design new functional elements and envision their subsequent integration inside a shape. This enables an exploration of both low-level details (material and device engineering) and elements at higher levels of abstraction (integration and network topology).

Appendix A

Ink formulations

The complete ink formulations are listed below in this appendix. Broadly, there are two families of inks that were used throughout this thesis - rigid material (RIG) and elastic matrix material (ELA) - but the specific formulations were tuned for each project to improve properties. Here the full formulations are listed for each part of the thesis. Briefly, the different components are homogenized and left to mix overnight using a magnetic stirrer. Finally, the ink is filtered using a 1 μm filter and degassed using a vacuum pump to remove small bubbles. The complete list of inks used in Part I is described in Table A.1. The formulations for two main inks used in Part II are listed in Table A.2. The inks used in making the magnetic actuators (Part III) are listed in Table A.3. Here, RIG and ELA are processed as described earlier simply by mixing with a magnetic stirrer overnight. The magnetic nanoparticle-based MPC ink was formulated as follows: 12 wt% of Iron(III)-Oxide nano-particles(Fe_3O_4), 80 wt% of the rigid ink formulation (without photoinitiators and photoinhibitors), and 8 wt% of Genomer 1116 were mixed together. 5 wt% of nonionic dispersant DISPERBYK110 was added on top of the total weight of the iron(III)oxide mixture (5 g of dispersant added for every 100 g of magnetic ink). The magnetic ink was then run on a bead-mill (M100 VSE TEFC, Engineered Mills, Inc., USA) with 300 μm yttria-stabilized zirconia beads for 7 h at 4000 rpm to break down agglomeration and stabilize the nano-particles within the suspension. After milling was completed, the ink was then transferred to a clean 250 mL container. 2 wt% of Irgacure819 and ITX were added

to the suspension and mixed vigorously with a spatula for several minutes. 0.1 wt% of 4-methoxyphenol was added finally as a photo-polymerization inhibitor. The ink was allowed to sit for 6 h to completely dissolve the photoinitiators in the ink. The ink was then filtered with a 1 μm filter before use.

Table A.1: Ink formulations for devices in Part I

Ink	Name/type (trade name)	Supplier	Content
Rigid polymer (RIG) (204.2 g)	cyclic trimethylolpropane acrylate (Genomer 1117)	Rahn USA Corp.	118 g
	bisphenol A epoxy diacrylate in 25% GPTA (Genomer 2252/GP25)	Rahn USA Corp.	64 g
	acrylic acid ester (Miramer 300)	Rahn USA Corp.	18 g
	bis(2,4,6-trimethylbenzoyl)-phenylphosphineoxide (Irgacure 819)	BASF, Germany	2 g
	2-isopropylthioxanthone(ITX)	Rahn USA Corp.	2 g
	4-methoxyphenol (MEHQ)	Sigma-Aldrich, USA	0.2 g
Elastic polymer (ELA) (201.25 g)	Low viscosity acrylic oligomer (CN3105)	Sartomer, USA	96 g
	isooctyl acrylate (SR440)	Sartomer, USA	34 g
	ethoxylated nonyl-phenol acrylate (SR504)	Sartomer, USA	32 g
	alkyl methacrylate (SR313B)	Sartomer, USA	20 g
	aliphatic urethane acrylate (Genomer 4215)	Rahn USA Corp.	16 g
	bis(2,4,6-trimethylbenzoyl)-phenylphosphineoxide	BASF, Germany	2 g
	2-isopropylthioxanthone (ITX)	Rahn USA Corp.	1 g
	4-methoxyphenol (MEHQ)	Sigma-Aldrich, USA	0.25 g
Silver ink (26.94 g)	ethanol, 200 proof	Koptec/VWR, USA	15.78 g
	butylamine, 99.5%	Sigma-Aldrich, USA	5.92 g
	silver acetate, anhydrous, 99%	Alfa Aesar, USA	4 g
	formic acid, ACS reagent >88%	Sigma-Aldrich, USA	0.976 g
	hydroxyethyl-cellulose	Sigma-Aldrich, USA	0.267 g
PEDOT:PSS ink (21 g)	poly(3,4-ethylenedioxythiophene) doped with polystyrene sulphonate (Clevios TM P Jet 700N)	Heraeus, Germany	20 g
	dimethyl sulfoxide, 99+% (DMSO)	Alfa Aesar, USA	1 g
Electrolyte (25.15 g)	Water, ACS reagent grade	RICCA Chem., USA	20 g
	glycerol, >99.5%	Sigma-Aldrich, USA	5 g
	potassium chloride	Macron Fine Chem.	0.15 g
Hydraulic fluid (25 g)	Viscosity standard mineral oil (S20)	Cannon Inst. Co.	25 g

Table A.2: Ink formulations for devices in Part II

Ink	Name/type (trade name)	Supplier	Content
Residual stress polymer (STR)	Low viscosity acrylic oligomer (CN3105)	Sartomer, USA	53.1 wt%
	isooctyl acrylate (SR440)	Sartomer, USA	18.8 wt%
	ethoxylated nonyl-phenol acrylate (SR504)	Sartomer, USA	17.7 wt%
	aliphatic urethane acrylate (Genomer 4215)	Rahn USA Corp.	8.85 wt%
	bis(2,4,6-trimethylbenzoyl)-phenylphosphineoxide (Irgacure 819)	BASF, Germany	1 wt%
	2-isopropylthioxanthone (ITX)	Rahn USA Corp.	0.5 wt%
	4-methoxyphenol (MEHQ)	Sigma-Aldrich, USA	0.05 wt%
Rigid polymer (RIG)	cyclic trimethylolpropane acrylate (Genomer 1117)	Rahn USA Corp.	57.8 wt%
	bisphenol A epoxy diacrylate in 25% GPTA (Genomer 2252/GP25)	Rahn USA Corp.	31.3 wt%
	acrylic acid ester (Miramer 300)	Rahn USA Corp.	8.8 wt%
	bis(2,4,6-trimethylbenzoyl)-phenylphosphineoxide (Irgacure 819)	BASF, Germany	1 wt%
	2-isopropylthioxanthone(ITX)	Rahn USA Corp.	1 wt%
	4-methoxyphenol (MEHQ)	Sigma-Aldrich, USA	0.1 wt%
Other inks	Same as in Table A.1		

Table A.3: Ink formulations for devices in Part III

Ink	Name/type (trade name)	Supplier	Content
Rigid polymer (RIG)	cyclic trimethylolpropane acrylate (Genomer 1117)	Rahn USA Corp.	57.8 wt%
	bisphenol A epoxy diacrylate in 25% GPTA (Genomer 2252/GP25)	Rahn USA Corp.	31.3 wt%
	acrylic acid ester (Miramer 300)	Rahn USA Corp.	8.8 wt%
	bis(2,4,6-trimethylbenzoyl)-phenylphosphineoxide (Irgacure 819)	BASF, Germany	2 wt%
	4-methoxyphenol (MEHQ)	Sigma-Aldrich, USA	0.1 wt%
Elastic polymer (ELA)	Low viscosity acrylic oligomer (CN3105)	Sartomer, USA	49.2 wt%
	ethoxylated nonyl-phenol acrylate (SR504)	Sartomer, USA	33.85 wt%
	alkyl methacrylate (SR313B)	Sartomer, USA	10.3 wt%
	aliphatic urethane acrylate (Genomer 4215)	Rahn USA Corp.	5.1 wt%
	bis(2,4,6-trimethylbenzoyl)-phenylphosphineoxide (Irgacure 819)	BASF, Germany	1 wt%
	2-isopropylthioxanthone (ITX)	Rahn USA Corp.	0.5 wt%
	4-methoxyphenol (MEHQ)	Sigma-Aldrich, USA	0.05 wt%
Magnetic nanoparticle-polymer composite ink (MPC)	Iron(III)-Oxide nano-particles - Fe ₃ O ₄	US Research Nanomaterials	12 wt%
	Rigid ink fomulation (RIG) - without photoinitiators & photoinhibitors (Genomer 1116)	Rahn USA Corp.	80 wt% 8 wt%
	Nonionic dispersant (DISPERBYK110) 5g added to every 100g of above mixture, then bead-milled	BYK Additives & Instruments	(to mixture)
	bis(2,4,6-trimethylbenzoyl)-phenylphosphineoxide (Irgacure 819)	BASF, Germany	+2 wt%
	2-isopropylthioxanthone (ITX)	Rahn USA Corp.	+2 wt%
	4-methoxyphenol (MEHQ)	Sigma-Aldrich, USA	+0.1 wt%

Bibliography

- [1] Betty J Meggers and Clifford Evans. A transpacific contact in 3000 BC. *Scientific American*, 214(1):28–35, 1966.
- [2] Wenwu Cao, Harley H Cudney, and Rainer Waser. Smart materials and structures. *Proceedings of the National Academy of Sciences*, 96(15):8330–8331, 1999.
- [3] Yiğit Mengüç, Nikolaus Correll, Rebecca Kramer, and Jamie Paik. Will robots be bodies with brains or brains with bodies? *Science Robotics*, 2(12):eaar4527, 2017.
- [4] Harold Abelson, Don Allen, Daniel Coore, Chris Hanson, George Homsy, Thomas F Knight Jr, Radhika Nagpal, Erik Rauch, Gerald Jay Sussman, and Ron Weiss. Amorphous computing. *Communications of the ACM*, 43(5):74–82, 2000.
- [5] Michael Andrew McEvoy and Nikolaus Correll. Materials that couple sensing, actuation, computation, and communication. *Science*, 347(6228):1261689, 2015.
- [6] Leila F Deravi, Andrew P Magyar, Sean P Sheehy, George RR Bell, Lydia M Mähger, Stephen L Senft, Trevor J Wardill, William S Lane, Alan M Kuzirian, Roger T Hanlon, et al. The structure–function relationships of a natural nanoscale photonic device in cuttlefish chromatophores. *Journal of The Royal Society Interface*, 11(93):20130942, 2014.
- [7] Roland S Johansson and AB Vallbo. Tactile sensibility in the human hand: rel-

- ative and absolute densities of four types of mechanoreceptive units in glabrous skin. *The Journal of physiology*, 286(1):283–300, 1979.
- [8] Sawyer Buckminster Fuller, Andrew D Straw, Martin Y Peek, Richard M Murray, and Michael H Dickinson. Flying drosophila stabilize their vision-based velocity controller by sensing wind with their antennae. *Proceedings of the National Academy of Sciences*, 111(13):E1182–E1191, 2014.
- [9] Guang-Zhong Yang, Jim Bellingham, Pierre E Dupont, Peer Fischer, Luciano Floridi, Robert Full, Neil Jacobstein, Vijay Kumar, Marcia McNutt, Robert Merrifield, et al. The grand challenges of science robotics. *Science Robotics*, 3(14):eaar7650, 2018.
- [10] George M Whitesides and Bartosz Grzybowski. Self-assembly at all scales. *Science*, 295(5564):2418–2421, 2002.
- [11] Joseph M Kahn, Randy H Katz, and Kristofer SJ Pister. Next century challenges: mobile networking for smart dust. In *Proceedings of the 5th annual ACM/IEEE international conference on Mobile computing and networking*, pages 271–278. ACM, 1999.
- [12] V Mironov, T Trusk, V Kasyanov, S Little, R Swaja, and R Markwald. Biofabrication: a 21st century manufacturing paradigm. *Biofabrication*, 1(2):022001, 2009.
- [13] Hideo Kodama. Automatic method for fabricating a three-dimensional plastic model with photo-hardening polymer. *Review of scientific instruments*, 52(11):1770–1773, 1981.
- [14] Charles W Hull. Apparatus for production of three-dimensional objects by stereolithography, March 11 1986. US Patent 4,575,330.
- [15] Zak C Eckel, Chaoyin Zhou, John H Martin, Alan J Jacobsen, William B Carter, and Tobias A Schaedler. Additive manufacturing of polymer-derived ceramics. *Science*, 351(6268):58–62, 2016.

- [16] Adam E Jakus, Alexandra L Rutz, Sumanas W Jordan, Abhishek Kannan, Sean M Mitchell, Chawon Yun, Katie D Koube, Sung C Yoo, Herbert E Whiteley, Claus-Peter Richter, et al. Hyperelastic bone: A highly versatile, growth factor-free, osteoregenerative, scalable, and surgically friendly biomaterial. *Science translational medicine*, 8(358):358ra127–358ra127, 2016.
- [17] Frederik Kotz, Karl Arnold, Werner Bauer, Dieter Schild, Nico Keller, Kai Sachsenheimer, Tobias M Nargang, Christiane Richter, Dorothea Helmer, and Bastian E Rapp. Three-dimensional printing of transparent fused silica glass. *Nature*, 544(7650):337, 2017.
- [18] Y Morris Wang, Thomas Voisin, Joseph T McKeown, Jianchao Ye, Nicholas P Calta, Zan Li, Zhi Zeng, Yin Zhang, Wen Chen, Tien Tran Roehling, et al. Additively manufactured hierarchical stainless steels with high strength and ductility. *Nature materials*, 17(1):63, 2018.
- [19] Ke Sun, Teng-Sing Wei, Bok Yeop Ahn, Jung Yoon Seo, Shen J Dillon, and Jennifer A Lewis. 3D printing of interdigitated li-ion microbattery architectures. *Advanced materials*, 25(33):4539–4543, 2013.
- [20] Yong Lin Kong, Ian A Tamargo, Hyoungsoo Kim, Blake N Johnson, Maneesh K Gupta, Tae-Wook Koh, Huai-An Chin, Daniel A Steingart, Barry P Rand, and Michael C McAlpine. 3D printed quantum dot light-emitting diodes. *Nano letters*, 14(12):7017–7023, 2014.
- [21] Joseph T Muth, Daniel M Vogt, Ryan L Truby, Yiğit Mengüç, David B Kolesky, Robert J Wood, and Jennifer A Lewis. Embedded 3D printing of strain sensors within highly stretchable elastomers. *Advanced Materials*, 26(36):6307–6312, 2014.
- [22] William M Marshall, James D Stegeman, Michael Zemba, Eric MacDonald, Corey Shemelya, Ryan Wicker, Andrew Kwas, and Craig Kief. Using additive manufacturing to print a cubesat propulsion system. In *51st AIAA/SAE/ASEE Joint Propulsion Conference*, page 4184, 2015.

- [23] Robert MacCurdy, Robert Katzschmann, Youbin Kim, and Daniela Rus. Printable hydraulics: a method for fabricating robots by 3D co-printing solids and liquids. In *Robotics and Automation (ICRA), 2016 IEEE International Conference On*, pages 3878–3885. IEEE, 2016.
- [24] David McCoul, Samuel Rosset, Samuel Schlatter, and Herbert Shea. Inkjet 3D printing of UV and thermal cure silicone elastomers for dielectric elastomer actuators. *Smart Materials and Structures*, 26(12):125022, 2017.
- [25] Brian Derby. Inkjet printing of functional and structural materials: fluid property requirements, feature stability, and resolution. *Annual Review of Materials Research*, 40:395–414, 2010.
- [26] Paul Calvert. Inkjet printing for materials and devices. *Chemistry of materials*, 13(10):3299–3305, 2001.
- [27] H Sirringhaus, T Kawase, RH Friend, T Shimoda, M Inbasekaran, W Wu, and EP Woo. High-resolution inkjet printing of all-polymer transistor circuits. *Science*, 290(5499):2123–2126, 2000.
- [28] Stephen R Forrest. The path to ubiquitous and low-cost organic electronic appliances on plastic. *Nature*, 428(6986):911, 2004.
- [29] Ana Claudia Arias, J Devin MacKenzie, Iain McCulloch, Jonathan Rivnay, and Alberto Salleo. Materials and applications for large area electronics: solution-based approaches. *Chemical reviews*, 110(1):3–24, 2010.
- [30] Michele A Cleary, Kristopher Kilian, Yanqun Wang, Jeff Bradshaw, Guy Cavet, Wei Ge, Amit Kulkarni, Patrick J Paddison, Kenneth Chang, Nihar Sheth, et al. Production of complex nucleic acid libraries using highly parallel in situ oligonucleotide synthesis. *Nature methods*, 1(3):241, 2004.
- [31] Tao Xu, Joyce Jin, Cassie Gregory, James J Hickman, and Thomas Boland. Inkjet printing of viable mammalian cells. *Biomaterials*, 26(1):93–99, 2005.

- [32] Thomas Boland, Tao Xu, Brook Damon, and Xiaofeng Cui. Application of inkjet printing to tissue engineering. *Biotechnology journal*, 1(9):910–917, 2006.
- [33] Pitchaya Sitthi-Amorn, Javier E Ramos, Yuwang Wang, Joyce Kwan, Justin Lan, Wenshou Wang, and Wojciech Matusik. Multifab: a machine vision assisted platform for multi-material 3D printing. *ACM Transactions on Graphics (TOG)*, 34(4):129, 2015.
- [34] Kevin J McHugh, Thanh D Nguyen, Allison R Linehan, David Yang, Adam M Behrens, Sviatlana Rose, Zachary L Tochka, Stephany Y Tzeng, James J Norman, Aaron C Anselmo, et al. Fabrication of fillable microparticles and other complex 3D microstructures. *Science*, 357(6356):1138–1142, 2017.
- [35] CJ Van Oss, RJ Good, and MK Chaudhury. Additive and nonadditive surface tension components and the interpretation of contact angles. *Langmuir*, 4(4):884–891, 1988.
- [36] Dan Soltman and Vivek Subramanian. Inkjet-printed line morphologies and temperature control of the coffee ring effect. *Langmuir*, 24(5):2224–2231, 2008.
- [37] Erica Lin, Yaning Li, Christine Ortiz, and Mary C Boyce. 3D printed, bio-inspired prototypes and analytical models for structured suture interfaces with geometrically-tuned deformation and failure behavior. *Journal of the Mechanics and Physics of Solids*, 73:166–182, 2014.
- [38] Benjamin C-K Tee, Alex Chortos, Andre Berndt, Amanda Kim Nguyen, Ariane Tom, Allister McGuire, Ziliang Carter Lin, Kevin Tien, Won-Gyu Bae, Huiliang Wang, et al. A skin-inspired organic digital mechanoreceptor. *Science*, 350(6258):313–316, 2015.
- [39] Ho-Hsiu Chou, Amanda Nguyen, Alex Chortos, John WF To, Chien Lu, Jianguo Mei, Tadanori Kurosawa, Won-Gyu Bae, Jeffrey B-H Tok, and Zhenan Bao. A chameleon-inspired stretchable electronic skin with interactive colour changing controlled by tactile sensing. *Nature communications*, 6:8011, 2015.

- [40] Stefan CB Mannsfeld, Benjamin CK Tee, Randall M Stoltenberg, Christopher V HH Chen, Soumendra Barman, Beinn VO Muir, Anatoliy N Sokolov, Colin Reese, and Zhenan Bao. Highly sensitive flexible pressure sensors with microstructured rubber dielectric layers. *Nature materials*, 9(10):859, 2010.
- [41] John A Rogers, Takao Someya, and Yonggang Huang. Materials and mechanics for stretchable electronics. *Science*, 327(5973):1603–1607, 2010.
- [42] Dae-Hyeong Kim, Nanshu Lu, Rui Ma, Yun-Soung Kim, Rak-Hwan Kim, Shuodao Wang, Jian Wu, Sang Min Won, Hu Tao, Ahmad Islam, et al. Epidermal electronics. *Science*, 333(6044):838–843, 2011.
- [43] Christina Larson, B Peele, S Li, S Robinson, M Totaro, L Beccai, B Mazzolai, and R Shepherd. Highly stretchable electroluminescent skin for optical signaling and tactile sensing. *Science*, 351(6277):1071–1074, 2016.
- [44] Tsuyoshi Sekitani, Ute Zschieschang, Hagen Klauk, and Takao Someya. Flexible organic transistors and circuits with extreme bending stability. *Nature materials*, 9(12):1015, 2010.
- [45] Martin Kaltenbrunner, Tsuyoshi Sekitani, Jonathan Reeder, Tomoyuki Yokota, Kazunori Kuribara, Takeyoshi Tokuhara, Michael Drack, Reinhard Schwödiauer, Ingrid Graz, Simona Bauer-Gogonea, et al. An ultra-lightweight design for imperceptible plastic electronics. *Nature*, 499(7459):458, 2013.
- [46] B Crone, A Dodabalapur, Y-Y Lin, RW Filas, Z Bao, A LaDuca, R Sarpeshkar, HE Katz, and W Li. Large-scale complementary integrated circuits based on organic transistors. *Nature*, 403(6769):521, 2000.
- [47] Hagen Klauk, Ute Zschieschang, Jens Pflaum, and Marcus Halik. Ultralow-power organic complementary circuits. *Nature*, 445(7129):745, 2007.
- [48] Magnus Berggren, David Nilsson, and Nathaniel D Robinson. Organic materials for printed electronics. *Nature materials*, 6(1):3, 2007.

- [49] Jeong Ho Cho, Jiyoul Lee, Yu Xia, Bongsoo Kim, Yiyong He, Michael J Renn, Timothy P Lodge, and C Daniel Frisbie. Printable ion-gel gate dielectrics for low-voltage polymer thin-film transistors on plastic. *Nature materials*, 7(11):900, 2008.
- [50] He Yan, Zhihua Chen, Yan Zheng, Christopher Newman, Jordan R Quinn, Florian Dötz, Marcel Kastler, and Antonio Facchetti. A high-mobility electron-transporting polymer for printed transistors. *Nature*, 457(7230):679, 2009.
- [51] Ji-Hyuk Choi, Han Wang, Soong Ju Oh, Taejong Paik, Pil Sung, Jinwoo Sung, Xingchen Ye, Tianshuo Zhao, Benjamin T Diroll, Christopher B Murray, et al. Exploiting the colloidal nanocrystal library to construct electronic devices. *Science*, 352(6282):205–208, 2016.
- [52] John R Tumbleston, David Shirvanyants, Nikita Ermoshkin, Rima Januszewicz, Ashley R Johnson, David Kelly, Kai Chen, Robert Pinschmidt, Jason P Rolland, Alexander Ermoshkin, et al. Continuous liquid interface production of 3D objects. *Science*, 347(6228):1349–1352, 2015.
- [53] Dimitri Kokkinis, Manuel Schaffner, and André R Studart. Multimaterial magnetically assisted 3D printing of composite materials. *Nature communications*, 6:8643, 2015.
- [54] Neralagatta M Sangeetha, Nicolas Decorde, Benoit Viallet, Guillaume Viau, and Laurence Ressler. Nanoparticle-based strain gauges fabricated by convective self assembly: Strain sensitivity and hysteresis with respect to nanoparticle sizes. *The Journal of Physical Chemistry C*, 117(4):1935–1940, 2013.
- [55] Giuseppe Tarabella, Clara Santato, Sang Yoon Yang, Salvatore Iannotta, George G Malliaras, and Fabio Cicoira. Effect of the gate electrode on the response of organic electrochemical transistors. *Applied Physics Letters*, 97(12):205, 2010.

- [56] Dion Khodagholy, Jonathan Rivnay, Michele Sessolo, Moshe Gurfinkel, Pierre Leleux, Leslie H Jimison, Eleni Stavrinidou, Thierry Herve, Sébastien Sanaur, Róisín M Owens, et al. High transconductance organic electrochemical transistors. *Nature communications*, 4:2133, 2013.
- [57] Peter Andersson Ersman, David Nilsson, Jun Kawahara, Göran Gustafsson, and Magnus Berggren. Fast-switching all-printed organic electrochemical transistors. *Organic electronics*, 14(5):1276–1280, 2013.
- [58] Steven B Walker and Jennifer A Lewis. Ink composition for making a conductive silver structure, October 18 2016. US Patent 9,469,773.
- [59] Mark G Allen, Mehran Mehregany, Roger T Howe, and Stephen D Senturia. Microfabricated structures for the insitu measurement of residual stress, youngs modulus, and ultimate strain of thin films. *Applied Physics Letters*, 51(4):241–243, 1987.
- [60] E Chason, BW Sheldon, LB Freund, JA Floro, and SJ Hearne. Origin of compressive residual stress in polycrystalline thin films. *Physical Review Letters*, 88(15):156103, 2002.
- [61] RG Treuting and WT Read Jr. A mechanical determination of biaxial residual stress in sheet materials. *Journal of Applied Physics*, 22(2):130–134, 1951.
- [62] C Casavola, A Cazzato, V Moramarco, and G Pappalettera. Preliminary study on residual stress in fdm parts. In *Residual Stress, Thermomechanics & Infrared Imaging, Hybrid Techniques and Inverse Problems, Volume 9*, pages 91–96. Springer, 2017.
- [63] Peter Mercelis and Jean-Pierre Kruth. Residual stresses in selective laser sintering and selective laser melting. *Rapid prototyping journal*, 12(5):254–265, 2006.
- [64] Christian Decker. The use of UV irradiation in polymerization. *Polymer International*, 45(2):133–141, 1998.

- [65] Paul So and Lawrence J Broutman. Residual stresses in polymers and their effect on mechanical behavior. *Polymer Engineering & Science*, 16(12):785–791, 1976.
- [66] Limei Huang, Ruiqi Jiang, Jingjun Wu, Jizhou Song, Hao Bai, Bogeng Li, Qian Zhao, and Tao Xie. Ultrafast digital printing toward 4D shape changing materials. *Advanced Materials*, 29(7), 2017.
- [67] Elliot Hawkes, B An, Nadia M Benbernou, H Tanaka, S Kim, ED Demaine, D Rus, and Robert J Wood. Programmable matter by folding. *Proceedings of the National Academy of Sciences*, 107(28):12441–12445, 2010.
- [68] Samuel Felton, Michael Tolley, Erik Demaine, Daniela Rus, and Robert Wood. A method for building self-folding machines. *Science*, 345(6197):644–646, 2014.
- [69] Xiaoying Guo, Huan Li, Bok Yeop Ahn, Eric B Duoss, K Jimmy Hsia, Jennifer A Lewis, and Ralph G Nuzzo. Two-and three-dimensional folding of thin film single-crystalline silicon for photovoltaic power applications. *Proceedings of the National Academy of Sciences*, 106(48):20149–20154, 2009.
- [70] Gerard J Hayes, Ying Liu, Jan Genzer, Gianluca Lazzi, and Michael D Dickey. Self-folding origami microstrip antennas. *IEEE Transactions on Antennas and Propagation*, 62(10):5416–5419, 2014.
- [71] Young Min Song, Yizhu Xie, Viktor Malyarchuk, Jianliang Xiao, Inhwa Jung, Ki-Joong Choi, Zhuangjian Liu, Hyunsung Park, Chaofeng Lu, Rak-Hwan Kim, et al. Digital cameras with designs inspired by the arthropod eye. *Nature*, 497(7447):95, 2013.
- [72] Sergei A Zotov, Montgomery C Rivers, Alexander A Trusov, and Andrei M Shkel. Folded MEMS pyramid inertial measurement unit. *IEEE Sensors Journal*, 11(11):2780–2789, 2011.
- [73] Sheng Xu, Zheng Yan, Kyung-In Jang, Wen Huang, Haoran Fu, Jeonghyun Kim, Zijun Wei, Matthew Flavin, Joselle McCracken, Renhan Wang, et al.

- Assembly of micro/nanomaterials into complex, three-dimensional architectures by compressive buckling. *Science*, 347(6218):154–159, 2015.
- [74] André R Studart and Randall M Erb. Bioinspired materials that self-shape through programmed microstructures. *Soft matter*, 10(9):1284–1294, 2014.
- [75] Samuel M Felton, Michael T Tolley, ByungHyun Shin, Cagdas D Onal, Erik D Demaine, Daniela Rus, and Robert J Wood. Self-folding with shape memory composites. *Soft Matter*, 9(32):7688–7694, 2013.
- [76] Qian Zhao, Weike Zou, Yingwu Luo, and Tao Xie. Shape memory polymer network with thermally distinct elasticity and plasticity. *Science advances*, 2(1):e1501297, 2016.
- [77] Johannes TB Overvelde, Twan A De Jong, Yanina Shevchenko, Sergio A Bercerra, George M Whitesides, James C Weaver, Chuck Hoberman, and Katia Bertoldi. A three-dimensional actuated origami-inspired transformable metamaterial with multiple degrees of freedom. *Nature communications*, 7:10929, 2016.
- [78] Jun-Hee Na, Arthur A Evans, Jinhye Bae, Maria C Chiappelli, Christian D Santangelo, Robert J Lang, Thomas C Hull, and Ryan C Hayward. Programming reversibly self-folding origami with micropatterned photo-crosslinkable polymer trilayers. *Advanced Materials*, 27(1):79–85, 2015.
- [79] Jiuke Mu, Chengyi Hou, Hongzhi Wang, Yaogang Li, Qinghong Zhang, and Meifang Zhu. Origami-inspired active graphene-based paper for programmable instant self-folding walking devices. *Science advances*, 1(10):e1500533, 2015.
- [80] Melina K Blees, Arthur W Barnard, Peter A Rose, Samantha P Roberts, Kathryn L McGill, Pinshane Y Huang, Alexander R Ruyack, Joshua W Kevek, Bryce Kobrin, David A Muller, et al. Graphene kirigami. *Nature*, 524(7564):204, 2015.

- [81] Timothy F Scott, Andrew D Schneider, Wayne D Cook, and Christopher N Bowman. Photoinduced plasticity in cross-linked polymers. *Science*, 308(5728):1615–1617, 2005.
- [82] Ying Liu, Julie K Boyles, Jan Genzer, and Michael D Dickey. Self-folding of polymer sheets using local light absorption. *Soft Matter*, 8(6):1764–1769, 2012.
- [83] Ying Liu, Matthew Miskiewicz, Michael J Escuti, Jan Genzer, and Michael D Dickey. Three-dimensional folding of pre-strained polymer sheets via absorption of laser light. *Journal of Applied Physics*, 115(20):204911, 2014.
- [84] Oliver G Schmidt and Karl Eberl. Nanotechnology: Thin solid films roll up into nanotubes. *Nature*, 410(6825):168, 2001.
- [85] Bin Xu and Ryan C Hayward. Low-voltage switching of crease patterns on hydrogel surfaces. *Advanced Materials*, 25(39):5555–5559, 2013.
- [86] Qi Ge, H Jerry Qi, and Martin L Dunn. Active materials by four-dimension printing. *Applied Physics Letters*, 103(13):131901, 2013.
- [87] Dan Raviv, Wei Zhao, Carrie McKnelly, Athina Papadopoulou, Achuta Kadambi, Boxin Shi, Shai Hirsch, Daniel Dikovsky, Michael Zyracki, Carlos Olguin, et al. Active printed materials for complex self-evolving deformations. *Scientific reports*, 4:7422, 2014.
- [88] Skylar Tibbits. 4D printing: multi-material shape change. *Architectural Design*, 84(1):116–121, 2014.
- [89] Yiqi Mao, Kai Yu, Michael S Isakov, Jiangtao Wu, Martin L Dunn, and H Jerry Qi. Sequential self-folding structures by 3D printed digital shape memory polymers. *Scientific reports*, 5:13616, 2015.
- [90] A Sydney Gladman, Elisabetta A Matsumoto, Ralph G Nuzzo, L Mahadevan, and Jennifer A Lewis. Biomimetic 4D printing. *Nature materials*, 15(4):413, 2016.

- [91] Quan Zhang, Kai Zhang, and Gengkai Hu. Smart three-dimensional lightweight structure triggered from a thin composite sheet via 3D printing technique. *Scientific reports*, 6:22431, 2016.
- [92] Yiqi Mao, Zhen Ding, Chao Yuan, Shigang Ai, Michael Isakov, Jiangtao Wu, Tiejun Wang, Martin L Dunn, and H Jerry Qi. 3D printed reversible shape changing components with stimuli responsive materials. *Scientific reports*, 6:24761, 2016.
- [93] Jiangtao Wu, Chao Yuan, Zhen Ding, Michael Isakov, Yiqi Mao, Tiejun Wang, Martin L Dunn, and H Jerry Qi. Multi-shape active composites by 3D printing of digital shape memory polymers. *Scientific reports*, 6:24224, 2016.
- [94] Qi Ge, Amir Hosein Sakhaei, Howon Lee, Conner K Dunn, Nicholas X Fang, and Martin L Dunn. Multimaterial 4D printing with tailorable shape memory polymers. *Scientific Reports*, 6:31110, 2016.
- [95] David Espalin, Danny W Muse, Eric MacDonald, and Ryan B Wicker. 3D printing multifunctionality: structures with electronics. *The International Journal of Advanced Manufacturing Technology*, 72(5-8):963–978, 2014.
- [96] Hiroki Ota, Sam Emaminejad, Yuji Gao, Allan Zhao, Eric Wu, Samyuktha Challa, Kevin Chen, Hossain M Fahad, Amit K Jha, Daisuke Kiriya, et al. Application of 3D printing for smart objects with embedded electronic sensors and systems. *Advanced Materials Technologies*, 1(1), 2016.
- [97] Eric MacDonald and Ryan Wicker. Multiprocess 3D printing for increasing component functionality. *Science*, 353(6307):aaf2093, 2016.
- [98] Matt Zarek, Michael Layani, Ido Cooperstein, Ela Sachyani, Daniel Cohn, and Shlomo Magdassi. 3D printing of shape memory polymers for flexible electronic devices. *Advanced Materials*, 28(22):4449–4454, 2016.

- [99] Jennifer N Rodriguez, Cheng Zhu, Eric B Duoss, Thomas S Wilson, Christopher M Spadaccini, and James P Lewicki. Shape-morphing composites with designed micro-architectures. *Scientific reports*, 6:27933, 2016.
- [100] Zhen Ding, Chao Yuan, Xirui Peng, Tiejun Wang, H Jerry Qi, and Martin L Dunn. Direct 4D printing via active composite materials. *Science advances*, 3(4):e1602890, 2017.
- [101] Stephen Timoshenko. Analysis of bi-metal thermostats. *JOSA*, 11(3):233–255, 1925.
- [102] Casper L Van Oosten, Cees WM Bastiaansen, and Dirk J Broer. Printed artificial cilia from liquid-crystal network actuators modularly driven by light. *Nature materials*, 8(8):677, 2009.
- [103] Jaakko VI Timonen, Christoffer Johans, Ky“osti Kontturi, Andreas Walther, Olli Ikkala, and Robin HA Ras. A facile template-free approach to magnetodiven, multifunctional artificial cilia. *ACS applied materials & interfaces*, 2(8):2226–2230, 2010.
- [104] Ambarish Ghosh and Peer Fischer. Controlled propulsion of artificial magnetic nanostructured propellers. *Nano letters*, 9(6):2243–2245, 2009.
- [105] Tian-Yun Huang, Mahmut Selman Sakar, Angelo Mao, Andrew J Petruska, Famin Qiu, Xue-Bo Chen, Stephen Kennedy, David Mooney, and Bradley J Nelson. 3D printed microtransporters: Compound micromachines for spatiotemporally controlled delivery of therapeutic agents. *Advanced Materials*, 27(42):6644–6650, 2015.
- [106] Lindsey Hines, Kirstin Petersen, Guo Zhan Lum, and Metin Sitti. Soft actuators for small-scale robotics. *Advanced Materials*, 29(13), 2017.
- [107] Jiyun Kim, Su Eun Chung, Sung-Eun Choi, Howon Lee, Junhoi Kim, and Sunghoon Kwon. Programming magnetic anisotropy in polymeric microactuators. *Nature materials*, 10(10):747, 2011.

- [108] Yangying Zhu, Dion S Antao, Rong Xiao, and Evelyn N Wang. Real-time manipulation with magnetically tunable structures. *Advanced Materials*, 26(37):6442–6446, 2014.
- [109] Randall M Erb, Joshua J Martin, Rasam Soheilian, Chunzhou Pan, and Jabulani R Barber. Actuating soft matter with magnetic torque. *Advanced Functional Materials*, 26(22):3859–3880, 2016.
- [110] Orphee Cugat, Jerome Delamare, and Gilbert Reyne. Magnetic micro-actuators and systems (MAGMAS). *IEEE Transactions on magnetics*, 39(6):3607–3612, 2003.
- [111] Malcolm McCaig. *Permanent Magnets in Theory and Practice*. Wiley, 1977.
- [112] Larry J Hornbeck. 128×128 deformable mirror device. *IEEE Transactions on Electron Devices*, 30(5):539–545, 1983.
- [113] Cuiling Gong and Tim Hogan. CMOS compatible fabrication processes for the digital micromirror device. *IEEE Journal of the Electron Devices Society*, 2(3):27–32, 2014.
- [114] Peter Vettiger, G Cross, M Despont, U Drechsler, U Durig, B Gotsmann, W Haberle, MA Lantz, HE Rothuizen, R Stutz, et al. The “millipede”-nanotechnology entering data storage. *IEEE Transactions on nanotechnology*, 99(1):39–55, 2002.
- [115] Katie L Hoffman and Robert J Wood. Passive undulatory gaits enhance walking in a myriapod millirobot. In *Intelligent Robots and Systems (IROS), 2011 IEEE/RSJ International Conference on*, pages 1479–1486. IEEE, 2011.
- [116] Yunhan Huang, Arvind Sai Sarathi Vasan, Ravi Doraiswami, Michael Osterman, and Michael Pecht. MEMS reliability review. *IEEE Transactions on Device and Materials Reliability*, 12(2):482–493, 2012.

- [117] Li Wen, James C Weaver, Patrick JM Thornycroft, and George V Lauder. Hydrodynamic function of biomimetic shark skin: effect of denticle pattern and spacing. *Bioinspiration & Biomimetics*, 10(6):066010, 2015.
- [118] Amy W Lang, Michael T Bradshaw, Jonathon A Smith, Jennifer N Wheelus, Philip J Motta, Maria L Habegger, and Robert E Hueter. Movable shark scales act as a passive dynamic micro-roughness to control flow separation. *Bioinspiration & biomimetics*, 9(3):036017, 2014.
- [119] SIDNEY L Tamm. Mechanical synchronization of ciliary beating within comb plates of ctenophores. *Journal of experimental biology*, 113(1):401–408, 1984.
- [120] B Anderson, J Shultz, and B Jayne. Axial kinematics and muscle activity during terrestrial locomotion of the centipede scolopendra heros. *Journal of experimental biology*, 198(5):1185–1195, 1995.
- [121] Holk Cruse. What mechanisms coordinate leg movement in walking arthropods? *Trends in neurosciences*, 13(1):15–21, 1990.
- [122] Holk Cruse, Volker Dürri, and Josef Schmitz. Insect walking is based on a decentralized architecture revealing a simple and robust controller. *Philosophical Transactions of the Royal Society of London A: Mathematical, Physical and Engineering Sciences*, 365(1850):221–250, 2007.
- [123] Guo Zhan Lum, Zhou Ye, Xiaoguang Dong, Hamid Marvi, Onder Erin, Wenqi Hu, and Metin Sitti. Shape-programmable magnetic soft matter. *Proceedings of the National Academy of Sciences*, page 201608193, 2016.
- [124] Nico P van Dijk, K Maute, M Langelaar, and F Van Keulen. Level-set methods for structural topology optimization: a review. *Structural and Multidisciplinary Optimization*, 48(3):437–472, 2013.
- [125] Ole Sigmund. Design of multiphysics actuators using topology optimization—part ii: Two-material structures. *Computer methods in applied mechanics and engineering*, 190(49):6605–6627, 2001.

- [126] Scott J Hollister. Porous scaffold design for tissue engineering. *Nature materials*, 4(7):518–524, 2005.
- [127] Gordon Wetzstein, Douglas Lanman, Matthew Hirsch, and Ramesh Raskar. Tensor displays: compressive light field synthesis using multilayer displays with directional backlighting. *ACM Transactions on Graphics (TOG)*, 31(4):80, 2012.
- [128] Wai-Man Pang, Yingge Qu, Tien-Tsin Wong, Daniel Cohen-Or, and Pheng-Ann Heng. Structure-aware halftoning. *ACM Transactions on Graphics (TOG)*, 27(3):89:1–89:8, 2008.
- [129] Amit Bermano, Ilya Baran, Marc Alexa, and Wojciech Matusik. SHADOWPIX: Multiple Images from Self Shadowing. *Computer Graphics Forum*, 2012.
- [130] S. Kirkpatrick, C. D. Gelatt, and M. P. Vecchi. Optimization by simulated annealing. *Science*, 220(4598):671–680, 1983.
- [131] Jorge Nocedal and Stephen J. Wright. *Numerical Optimization*. Springer, 2000.
- [132] Martin Philip Bendsøe and Ole Sigmund. *Topology Optimization: Theory, Methods and Applications*. Springer-Verlag Berlin Heidelberg, 2003.
- [133] Alex Chortos, Jia Liu, and Zhenan Bao. Pursuing prosthetic electronic skin. *Nature materials*, 15(9):937, 2016.
- [134] Roland S Johansson and J Randall Flanagan. Coding and use of tactile signals from the fingertips in object manipulation tasks. *Nature Reviews Neuroscience*, 10(5):345, 2009.
- [135] Brygida Dzidek, Sérena Bochereau, Simon A Johnson, Vincent Hayward, and Michael J Adams. Why pens have rubbery grips. *Proceedings of the National Academy of Sciences*, 114(41):10864–10869, 2017.
- [136] Kuniharu Takei, Toshitake Takahashi, Johnny C Ho, Hyunhyub Ko, Andrew G Gillies, Paul W Leu, Ronald S Fearing, and Ali Javey. Nanowire active-matrix

- circuitry for low-voltage macroscale artificial skin. *Nature materials*, 9(10):821, 2010.
- [137] Changhyun Pang, Gil-Yong Lee, Tae-il Kim, Sang Moon Kim, Hong Nam Kim, Sung-Hoon Ahn, and Kahp-Yang Suh. A flexible and highly sensitive strain-gauge sensor using reversible interlocking of nanofibres. *Nature materials*, 11(9):795, 2012.
- [138] Chuan Wang, David Hwang, Zhibin Yu, Kuniharu Takei, Junwoo Park, Teresa Chen, Biwu Ma, and Ali Javey. User-interactive electronic skin for instantaneous pressure visualization. *Nature materials*, 12(10):899, 2013.
- [139] Gregor Schwartz, Benjamin C-K Tee, Jianguo Mei, Anthony L Appleton, Do Hwan Kim, Huiliang Wang, and Zhenan Bao. Flexible polymer transistors with high pressure sensitivity for application in electronic skin and health monitoring. *Nature communications*, 4:1859, 2013.
- [140] Sungwon Lee, Amir Reuveny, Jonathan Reeder, Sunghoon Lee, Hanbit Jin, Qihan Liu, Tomoyuki Yokota, Tsuyoshi Sekitani, Takashi Isoyama, Yusuke Abe, et al. A transparent bending-insensitive pressure sensor. *Nature nanotechnology*, 11(5):472, 2016.
- [141] Jonghwa Park, Marie Kim, Youngoh Lee, Heon Sang Lee, and Hyunhyub Ko. Fingertip skin-inspired microstructured ferroelectric skins discriminate static/dynamic pressure and temperature stimuli. *Science advances*, 1(9):e1500661, 2015.
- [142] Gereon H Büscher, Risto Kõiva, Carsten Schürmann, Robert Haschke, and Helge J Ritter. Flexible and stretchable fabric-based tactile sensor. *Robotics and Autonomous Systems*, 63:244–252, 2015.
- [143] Asli Atalay, Vanessa Sanchez, Ozgur Atalay, Daniel M Vogt, Florian Haufe, Robert J Wood, and Conor J Walsh. Batch fabrication of customizable silicone-

- textile composite capacitive strain sensors for human motion tracking. *Advanced Materials Technologies*, 2(9), 2017.
- [144] Tommaso D’Alessio. Measurement errors in the scanning of piezoresistive sensors arrays. *Sensors and Actuators A: Physical*, 72(1):71–76, 1999.
- [145] W Daniel Hillis. A high-resolution imaging touch sensor. *The International Journal of Robotics Research*, 1(2):33–44, 1982.
- [146] Roberto Lazzarini, R Magni, and Paolo Dario. A tactile array sensor layered in an artificial skin. In *Intelligent Robots and Systems 95. ‘Human Robot Interaction and Cooperative Robots’, Proceedings. 1995 IEEE/RSJ International Conference on*, volume 3, pages 114–119. IEEE, 1995.
- [147] Athina Papadopoulou, Jared Laucks, and Skylar Tibbits. Auxetic materials in design and architecture. *Nat. Rev. Mater*, 2:17078, 2017.
- [148] Ying Jiang, Zhiyuan Liu, Naoji Matsuhisa, Dianpeng Qi, Wan Ru Leow, Hui Yang, Jiancan Yu, Geng Chen, Yaqing Liu, Changjin Wan, et al. Auxetic mechanical metamaterials to enhance sensitivity of stretchable strain sensors. *Advanced Materials*, 30(12):1706589, 2018.
- [149] Mina Konaković, Keenan Crane, Bailin Deng, Sofien Bouaziz, Daniel Piker, and Mark Pauly. Beyond developable: computational design and fabrication with auxetic materials. *ACM Transactions on Graphics (TOG)*, 35(4):89, 2016.
- [150] Antonio Torralba, Rob Fergus, and William T Freeman. 80 million tiny images: A large data set for nonparametric object and scene recognition. *IEEE transactions on pattern analysis and machine intelligence*, 30(11):1958–1970, 2008.
- [151] Aude Oliva and Philippe G Schyns. Diagnostic colors mediate scene recognition. *Cognitive psychology*, 41(2):176–210, 2000.

- [152] Jiquan Ngiam, Aditya Khosla, Mingyu Kim, Juhan Nam, Honglak Lee, and Andrew Y Ng. Multimodal deep learning. In *Proceedings of the 28th international conference on machine learning (ICML-11)*, pages 689–696, 2011.
- [153] Yusuf Aytar, Carl Vondrick, and Antonio Torralba. Soundnet: Learning sound representations from unlabeled video. In *Advances in Neural Information Processing Systems*, pages 892–900, 2016.
- [154] Roberto Calandra, J Lin, A Owens, J Malik, D Jayaraman, Edward H Adelson, Wenzhen Yuan, and Sergey Levine. More than a feeling: Learning to grasp and regrasp using vision and touch. *Advances in Neural Information Processing Systems*, pages 1–10, 2017.
- [155] Wenzhen Yuan, Shaoxiong Wang, Siyuan Dong, and Edward Adelson. Connecting look and feel: Associating the visual and tactile properties of physical materials. In *Proceedings of the 2017 IEEE Conference on Computer Vision and Pattern Recognition (CVPR17), Honolulu, HI, USA*, pages 21–26, 2017.
- [156] Pranjul Shah, Joëlle V Fritz, Enrico Glaab, Mahesh S Desai, Kacy Greenhalgh, Audrey Frachet, Magdalena Niegowska, Matthew Estes, Christian Jäger, Carole Seguin-Devaux, et al. A microfluidics-based in vitro model of the gastrointestinal human–microbe interface. *Nature communications*, 7:11535, 2016.